

May 2016

In-Situ Synthesis of Aluminum- Titanium Diboride Metal Matrix Hybrid Nanocomposite

Afsaneh Dorri Moghdam
University of Wisconsin-Milwaukee

Follow this and additional works at: <https://dc.uwm.edu/etd>

 Part of the [Materials Science and Engineering Commons](#)

Recommended Citation

Dorri Moghdam, Afsaneh, "In-Situ Synthesis of Aluminum- Titanium Diboride Metal Matrix Hybrid Nanocomposite" (2016). *Theses and Dissertations*. 1137.
<https://dc.uwm.edu/etd/1137>

This Dissertation is brought to you for free and open access by UWM Digital Commons. It has been accepted for inclusion in Theses and Dissertations by an authorized administrator of UWM Digital Commons. For more information, please contact open-access@uwm.edu.

**IN-SITU SYNTHESIS OF ALUMINUM- TITANIUM DIBORIDE METAL MATRIX
HYBRID NANOCOMPOSITE**

by

Afsaneh Dorri Moghadam

A Dissertation Submitted in

Partial Fulfillment of the

Requirements for the degree of

Doctor of Philosophy

in Engineering

at

The University of Wisconsin-Milwaukee

May 2016

ABSTRACT

IN-SITU SYNTHESIS OF ALUMINUM- TITANIUM DIBORIDE METAL MATRIX HYBRID NANOCOMPOSITE

by

Afsaneh Dorri Moghadam

The University of Wisconsin-Milwaukee, 2016
Under the Supervision of Professor Pradeep K. Rohatgi

Metal matrix nanocomposites (MMNC's) are reported to have improved mechanical, thermal and electrical properties as compared to their respective base alloys. To date, these materials have been synthesized mainly by powder metallurgy or deformation processing. Solidification synthesis of MMNCs is a promising method, capable of economically producing large and complex shapes, however technical challenges including nanoparticle agglomeration, and poor interfacial strength have hindered the adoption of this technology. In-situ processing methods, in which the reinforcements are synthesized in liquid metals, typically via exothermic reactions offer the potential for improved dispersion and interfacial bonding between the reinforcement and the matrix, however this technique has been largely unexplored in the literature for metal matrix nanocomposites. The objectives of this research were to examine the feasibility of synthesizing nano or sub-micron size particulates in liquid aluminum using in-situ stir mixing and squeeze casting. An exothermic reaction was designed to synthesize Al_2O_3 and TiB_2 from TiO_2 particles and elemental boron in an aluminum melt. This dissertation investigates (i) the mechanism of aluminothermic and borothermic reduction of titanium oxide in the presence of molten aluminum and boron,

(ii) in situ synthesis of micron and nano sized particles via solidification processing, and (iii) the effects of processing variables on the physical, microstructural, mechanical and tribological properties of in-situ MMNCs. Microstructural examination and theoretical analysis indicates that the reaction to form TiB_2 and Al_2O_3 proceeds through several complex non-equilibrium reactions. A multi-stage reaction model is proposed to describe the process by which the TiO_2 surface is reduced to form Al_2O_3 and TiB_2 . The effects of the powder particle size on the formation of reinforcing phases and microstructural evolution have been investigated and it was found that nanosized TiO_2 powder promoted the formation of smaller size reinforcing phases. Furthermore, a solidification route has been designed to fabricate in-situ aluminum composites reinforced with submicron Al_2O_3 and TiB_2 particulates. Experimental and theoretical analysis is presented that shows that the particle size and refining power of nanoparticles is controlled by the viscosity of the melt, rather than precipitation and growth. In addition, it was found that increasing the weight percentage of nanoparticles of TiO_2 resulted in an increase in elastic modulus with good agreement to analytical models. Increasing the weight percentage of reinforcement up to 4 wt% resulted in an increase in the hardness greater than that predicted by the rule of mixtures or the Hall Petch relationship.

© Copyright by Afsaneh Dorri Moghadam, 2016
All Rights Reserved

I dedicate this research work to

EMAD

FOR HIS UNCONDITIONAL LOVE.

I LOVE YOU.

And also

To my parents, my brother, and my sister for their endless love, support, and
encouragements.

TABLE OF CONTENTS

| | |
|----------------------------------------------------------------------------------|-------------|
| TABLE OF CONTENTS ----- | vi |
| LIST OF FIGURES ----- | viii |
| LIST OF TABLES ----- | xiii |
| ACKNOWLEDGEMENTS ----- | xiv |
| CHAPTER 1. INTRODUCTION ----- | 1 |
| 1.1 Introduction to Metal Matrix Nanocomposites ----- | 1 |
| 1.2 Research Objectives----- | 6 |
| CHAPTER 2. LITERATURE REVIEW ----- | 8 |
| 2.1 Introduction ----- | 8 |
| 2.2 In-situ Al/TiB ₂ composites----- | 12 |
| 2.2.1 Mixed salt reaction or flux assisted synthesis (FAS)----- | 13 |
| 2.2.2 Liquid Mixing Synthesis ----- | 16 |
| 2.2.3 Self-propagating high temperature synthesis (SHS) ----- | 18 |
| 2.3 In-situ Al/TiB ₂ nanocomposites----- | 19 |
| 2.4 Ultrasonic Cavitation–Based Solidification Processing----- | 21 |
| 2.5 Summary and Conclusion----- | 25 |
| CHAPTER 3. REACTION MECHANISM [137] ----- | 28 |
| 3.1 Thermodynamic Considerations ----- | 28 |
| 3.2 Materials and Experimental----- | 30 |
| 3.3 Results and Discussion ----- | 33 |
| 3.4 Summary ----- | 51 |
| CHAPTER 4. PROCESSING/STRUCTURE RELATIONSHIPS ----- | 53 |
| 4.1 Introduction ----- | 53 |
| 4.2 Materials and Experimental----- | 53 |
| 4.2.1 Materials ----- | 53 |
| 4.2.2 Composite fabrication----- | 54 |
| 4.2.3 Characterization of Composites----- | 58 |
| 4.3 Results and Discussion----- | 64 |
| 4.3.1 Synthesis of composites starting with micron size TiO ₂ ----- | 64 |
| 4.3.2 Synthesis of composites starting with nano size TiO ₂ ----- | 69 |
| 4.3.3 Comparison of mechanical properties of micro and nanocomposites ----- | 76 |
| 4.3.4 Variation of mechanical properties with reinforcement content----- | 84 |
| 4.3.5 Variation of properties with processing parameters ----- | 89 |
| 4.3.6 Variation of tribological properties with processing parameters [145]----- | 99 |
| 4.3.7 Summary----- | 107 |
| CHAPTER 5. CONCLUSION ----- | 109 |

| | |
|--------------------------------------------------------------------------------------------------------------------------------|------------|
| CHAPTER 6. FUTURE WORK ----- | 114 |
| CHAPTER 7. REFERENCES ----- | 116 |
| Appendix I (Corrosion and Wetting of Al/ (TiB₂-Al₂O₃) Micro- and Nanocomposites) ----- | 124 |

LIST OF FIGURES

| | |
|--------------------------------------------------------------------------------------------------------------------------------------------------------------------------------------------------------------------------------------------------------------------------------------------------------------------------------------------------------------------------------------------------------------------------------------------------------------------------------------------------------------------------------------------------------------------------------------------------------------------------------------------------------------------|----|
| Figure 1 Optical micrographs of a dissolving TiAl_3 particle obtained through video frames during hot stage observations [119]. | 17 |
| Figure 2 Generation of an acoustic bubble. | 22 |
| Figure 3 Schematic of cavitation bubble collapse. | 23 |
| Figure 4 The cavitated bubble collapse and interparticle collisions lead to erosion, surface cleaning and wetting of the particles and particle size reduction. | 24 |
| Figure 5 A simplified model for two SiC nanoparticles in aluminum alloy melt and the forces keep these particles together. | 25 |
| Figure 6 The temperature dependence of Gibbs free energy change (ΔG_0). | 29 |
| Figure 7 comparing free energy changes by temperature of different possible compounds in Al-Ti-B system. | 30 |
| Figure 8 Schematic showing DSC/TGA chamber equipped with Controlled back filled atmosphere. | 32 |
| Figure 9 DSC trace of mixture of a) Pure aluminum b) Al-TiO ₂ -B heated in the temperature range of 200–1200°C. | 34 |
| Figure 10 X-ray diffraction patterns of the Al-B-TiO ₂ Mixture and samples after thermal processing (a) Unheated mixture (b) Heat treated at 760 °C and quenched (c) Heat treated at 760 °C followed by 30 min isothermal and quenched (d) Heat treated at 900 °C and quenched (e) Heat treated at 900 °C followed by 5 min isothermal and quenched (f) Heat treated at 900 °C followed by 10 min isothermal and quenched (g) Heat treated at 900 °C followed by 30 min isothermal and quenched (h) Heat treated at 990 °C and quenched (i) Heat treated at 990 °C followed by 30 min isothermal and quenched (j) Heat treated at 1200 °C and quenched. | 35 |
| Figure 11 The Secondary Electron Images of (a) and (b) TiO ₂ anatase particle, and (c and (d) TiO ₂ rutile particle. | 37 |
| Figure 12 TiO ₂ surface obtained from heat treatment at 900 °C with no dwell time (a) and (d) the secondary electron images and (b) aluminum elemental map (c) Oxygen elemental map. | 39 |
| Figure 13 (a) Transmission electron microscopy image and (b) Energy Dispersive spectrum of the nanowire structure on TiO ₂ surface obtained from heat treatment at 900 °C with no dwell time. | 40 |
| Figure 14 The secondary electron image obtained from the powders retrieved from 900 °C heat treatment and were lightly grounded using a mortar and pestle. | 42 |
| Figure 15 High resolution XRD spectra showing B ₂ O ₃ characteristic peaks at a) 43.12° b) 40.41° indexed with the 06-0634 JCPDS. | 43 |

| | |
|-----------------------------------------------------------------------------------------------------------------------------------------------------------------------------------------------------------------------------------------------------------------------------------------------------------------------------------------------------------------------------------------------------------------------------------------------------------------------------------------------------------------------------------------------------------------------------------------------------------------------------------------------------------------------------------------------------------------------------------------------|----|
| Figure 16 (a) Secondary electron image and (b) Backscattered electron (BSE) image of crack on $\text{Al}_2\text{O}_3/\text{Al}_3\text{Ti}$ shell obtained from the powders retrieved from 900 °C for 5 minute heat treatment..... | 45 |
| Figure 17 (a) Secondary electron image of TiB_2 overgrown nodule on TiO_2 surface (b) Backscattered electron (BSE) image obtained from the powders retrieved from 900 °C after 5 minute heat treatment..... | 45 |
| Figure 18 (a) and (b) The secondary electron image (c) and (d) Bright Field Transmission electron microscopy image of particles obtained from the powders retrieved from 900 °C for 10 minute heat treatment. | 46 |
| Figure 19 (a) Secondary electron image and (a) Backscattered electron (BSE) image of different phases obtained from the powders retrieved from 1200 °C heat treatment. | 48 |
| Figure 20 Secondary electron image and the elemental map (Oxygen, Boron, and Titanium) of the mixture of micron size TiO_2 , aluminum, and boron heated up to 1200 °C..... | 49 |
| Figure 21 Schematic representation of the proposed five stage model conversion of TiO_2 to TiB_2 and Al_2O_3 in liquid aluminum; Stage I- Melting of Al, dissolution of B, and Phase change of TiO_2 from Anatase to Rutile, Stage II- Attack of Al and B on TiO_2 and formation of Al_2O_3 shell on TiO_2 surface, Stage III, Creation of TiB_2 by attack of B on TiBO_3 and Ti_2O_3 Stage IV- Aluminothermic reduction of remaining TiO_2 and formation of titanium suboxides, and stage V- Complete exhaustion of intermediates, dissolution of Al_3Ti , and precipitation of TiB_2 | 50 |
| Figure 22 (a) Bright Field (b) Dark Field Transmission electron microscopy image of the particles obtained from the heat treatment of the mixture of nano size TiO_2 , aluminum, and boron heated up to 1200 °C. | 50 |
| Figure 23 (a) Bright Field Transmission electron microscopy image and (b) and (c) HRTEM images the particles obtained from the heat treatment of the mixture of nano size TiO_2 -Al-B heated up to 1200 °C indexed by Al_2O_3 75-1862 JCPDS card | 51 |
| Figure 24 (a) Bright Field Transmission electron microscopy image and (b) and (c) HRTEM images the particles obtained from the heat treatment of the mixture of nano size TiO_2 -Al-B heated up to 1200 °C indexed by TiB_2 35-741JCPDS card | 51 |
| Figure 25 Line scan X-Ray spectroscopy of the Al/ Al_2O_3 - TiB_2 composite casted in the uncoated clay crucible | 54 |
| Figure 26 The mixed powders pressed into pellets using formed cylindrical pellets | 55 |
| Figure 27 The experimental set up for a) in-situ reactive stir mixing process b) Ultrasonic assisted in-situ reactive stir mixing process c) Squeeze Casting | 56 |
| Figure 28 drawing of specimens which have been cut and mounted for microstructural analysis | 59 |
| Figure 29 The tensile test specimens and its drawing | 61 |
| Figure 30 Schematic illustration of reaction products formed on particle/ liquid interface | 64 |

| | |
|-----------------------------------------------------------------------------------------------------------------------------------------------------------------------------------------------------------------------------------------------------------------------------------------------------------------------------------------------------------------------------------------------------------------|----|
| Figure 31 a) Optical microstructure of Aluminum/ (TiB ₂ -Al ₂ O ₃) microcomposite starting with 25 μm TiO ₂ precursor b) grey threshold in (a), c) phases volume percentage d)particle size distribution | 65 |
| Figure 32 TEM image of Aluminum/(TiB ₂ -Al ₂ O ₃ composite prepared starting with 25 μm TiO ₂ precursor with Al ₂ O ₃ and TiB ₂ particles, labeled respectively | 66 |
| Figure 33 XRD pattern of the powders skimmed from the surface of the melt before pouring | 67 |
| Figure 34 XRD pattern of the residual powders remained in the crucible after melt pouring | 67 |
| Figure 35 XRD pattern of the Al- (TiB ₂ / Al ₂ O ₃) hybrid composite synthesized using stir casting..... | 70 |
| Figure 36 Particle size distribution of nanoparticles using DLS method..... | 71 |
| Figure 37 Bimodal particle size distribution of nanoparticles using DLS method | 72 |
| Figure 38 Partcile- Eddie streamline interaction | 74 |
| Figure 39 TEM of aluminum/ (TiB ₂ -Al ₂ O ₃) nanocomposites produced by liquid stir casting a) In-situ stir mixing b) In-situ stir/ultrasonic mixing..... | 76 |
| Figure 40 The cross polarized optical macrograph of (a) the unreinforced aluminum, (b) the microcomposite, and (c) The nanocomposite processed at similar conditions containing 4 weight percent reinforcement | 78 |
| Figure 41 The engineering stress-strain curves of (a) microcomposites reinforced with 4wt% hybrid particles at 700°C, (b) microcomposites reinforced with 4wt% hybrid particles at 1000°C, (c) nanocomposites reinforced with 4wt% hybrid particles at 700 °C, (d) nanocomposites reinforced with 4wt% hybrid particles at 850 °C, and (e) nanocomposites reinforced with 4wt% hybrid particles at 1000 °C..... | 79 |
| Figure 42 Macro fractographs of unreinforced, micron, and nano particle reinforced composite tensile specimens..... | 80 |
| Figure 43 micro fractographs of unreinforced and nano particle reinforced composite tensile specimens | 80 |
| Figure 44 Tensile specimen fracture surface of the microcomposites reinforced with hybrid particles..... | 82 |
| Figure 45 Tensile specimen fracture surface of the nanocomposites reinforced with hybrid particles..... | 82 |
| Figure 46 (a) The cross polarized optical micrograph, and (b,c) the SEM fracture surface micrograph of Al/ (TiB ₂ - Al ₂ O ₃) hybrid nanocomposites | 84 |
| Figure 47 Typical curve of load versus penetration depth in an indentation test. | 85 |
| Figure 48 The force displacement diagram of Nano indentation test. | 86 |
| Figure 49 Average Elastic Modulus values for aluminum and its nanocomposites as a function of particle loading..... | 88 |

| | |
|------------------------------------------------------------------------------------------------------------------------------------------------------------------------------------------------------------------------------------|-----|
| Figure 50 Comparison between theoretical prediction and experimental data using the Hashin- Shtrikman analytical model..... | 89 |
| Figure 51 The grain size variation by pouring temperature of aluminum melt | 90 |
| Figure 52 The grain size variation by mixing temperature for unreinforced and particle reinforced composites | 91 |
| Figure 53 Schematic representation of the boundary layer on TiO ₂ particles during stir mixing and turbulent flow effect on the detachment of TiB ₂ nanoparticles during mixing..... | 93 |
| Figure 54 The variation of experimental data obtained for the aluminum melt viscosity with temperature [144]..... | 94 |
| Figure 55 The experimental data collected for the variation in refinement ratio with pouring temperature at various mixing times for the nanocomposite reinforced with 4wt% hybrid particles | 95 |
| Figure 56 Variation in refinement ratio by temperature for the nanocomposites reinforced with 4wt% hybrid particles; the fitted curves of the experimental data is in accordance with the viscosity control prediction model | 95 |
| Figure 57 The experimental data collected for the variation in refinement ratio by mixing times at various temperatures for the nanocomposites reinforced with 4wt% hybrid particles..... | 96 |
| Figure 58 The 3D plot of variation in grain ratio by temperature and time for the nanocomposites reinforced with 4wt% hybrid particles. | 96 |
| Figure 59 Variation in a) Hardness and, b) Yield Stress of the nanocomposites by processing temperature for 4wt% particle loading | 97 |
| Figure 60 TEM image of dislocations around particles | 98 |
| Figure 61 Variation of coefficient of friction of pure aluminum and nanocomposites reinforced with 4wt% hybrid particles synthesized at various processing conditions..... | 101 |
| Figure 62 Lubricant tribofilm formation on worn surface of composites [146]..... | 101 |
| Figure 63 Variation of wear rate and hardness with reaction temperature for a) Unreinforced aluminum, b) nanocomposites reinforced with 4wt% hybrid particle | 102 |
| Figure 64 SEM micrographs of the worn surfaces at various processing times and temperatures | 105 |
| Figure 65 Topography image of worn surface for 850 °C reaction temperature for a) pure aluminum, b) 5 min, c) 10 min and d) 15 min reaction time and e) linear profile of worn surfaces..... | 106 |
| Figure 66 Energy dispersive spectrum (EDS) of the worn surface..... | 107 |
| Figure 67 Rame Hart Model 500 Goniometer (Measures Contact Angle of Water in Air & Oil in Water)..... | 126 |
| Figure 68 Schematic of water/air contact angle measurement. | 126 |

| | |
|-----------------------------------------------------------------------------------------------------------------------------------------------------------------|-----|
| Figure 69 Comparison of contact angles between aluminum and its composites at different pouring temperature | 127 |
| Figure 70 Variation in contact angle by the matrix grain size | 128 |
| Figure 71 Potentiodynamic polarization plot of unreinforced pure aluminum and Aluminum/ (TiB ₂ -Al ₂ O ₃) nanocomposite | 129 |

LIST OF TABLES

| | |
|----------------------------------------------------------------------------------------------------------------------------------------------------------------------|-----|
| Table 1 List of products formed through heating and isothermal reactions in Al-TiO ₂ -B system..... | 33 |
| Table 2 Coded levels of liquid mixing independent processing variables..... | 57 |
| Table 3 Experiment Design- Liquid Mixing | 58 |
| Table 4 Density, molar weight, and molar volume of different compounds present in the Al-B-TiO ₂ system | 66 |
| Table 5 Stir mixing experimental parameters | 74 |
| Table 6 Summary of average properties of the micro and nanocomposites reinforced with 4wt% hybrid particles at various processing condition. | 77 |
| Table 7 Estimated reinforcement loading in the composites..... | 85 |
| Table 8 Measured values for elastic modulus and hardness of particle reinforced aluminum nanocomposites | 87 |
| Table 9 Corrosion current and corrosion potential of unreinforced pure aluminum and Aluminum/ (TiB ₂ -Al ₂ O ₃) nanocomposite..... | 129 |

ACKNOWLEDGEMENTS

I would like to thank my advisor Distinguished Professor Pardeep K. Rohatgi for the invaluable chance to pursue research under him. All guidance, motivation, advice and patience from him have been channeled properly.

I would also like to thank Dr. Ben Schultz and Dr. JB Ferguson for their precious time spent on very constructive discussions. Valuable help from Dr. Hardcastle and Dr. Hugo Lopez for advanced analysis and characterization is greatly appreciated.

I also have to thank the members of my PhD committee, Professors Hugo Lopez, Dr. Amano, Dr. Changsoo Kim, and Dr. Sobolev for their helpful career advice and suggestions in general.

Special thanks to Dr. Sohn and Le Zhou at University of Florida, as well as to Donald Robertson and Heather Owen at UW-Milwaukee for help in SEM and TEM work. Thanks to Rahim Reshadi for providing structural lab facilities and support.

Thank you Michael Biening, Farhad Balali, Jared Gross, and the students of the Center for Composite Materials who have helped considerably over the past years.

Financial support in the form of a research scholarship from the Foundry Education Foundation and University of Wisconsin- Milwaukee is firmly acknowledged.

The authors would like gratefully acknowledge the support of the NSF I/UCRC by partly funding this research under grant NSF- MIL107834.

Words cannot express how grateful I am to my family who support in all side of life.

Last but certainly not least, I would like to thank my colleague and my husband Emad Omrani who helped me in all of the stages of the work.

CHAPTER 1. INTRODUCTION

1.1 Introduction to Metal Matrix Nanocomposites

A composite material is the product of combining two or more dissimilar materials of separate phases to form another material having superior properties that are different from either parent materials. In automotive, aerospace and sports industries, the requirement for high performance materials to meet challenging demands keeps increasing. Because of their limited properties, it is more difficult for conventional materials, metals and alloys to keep up with such demands, which are often difficult to be engineered and designed [1-3].

Based on reinforcing metals with suitable reinforcement, metal matrix composites (MMCs) provide alternative material with enhanced properties to satisfy the challenging demands. Composite materials can be more easily tailored to have specific properties such as being lightweight [4, 5], having high specific strengths and stiffnesses [6], high wear resistance and low coefficient of friction [7], high hardness [8], high thermal conductivity [9], low coefficient of thermal expansion [10], high energy absorption [11], and a damping capacity [12] than conventional materials. Based on the processing techniques that have developed, metal matrix composites can be divided into three categories: particle reinforced MMCs, short fiber reinforced MMCs and continuous fiber reinforced MMCs. Continuous fiber MMCs can be more difficult and expensive to fabricate, unlike particle reinforced MMCs. Furthermore, composites containing aligned reinforcement will cause pronounced anisotropic properties in the reinforcement direction for the primary mechanical properties, such as strength and stiffness [13]. The MMCs containing non-aligned reinforcement may be used in applications where near-isotropic properties would be preferred. Particulate reinforced metal matrix composites are also attractive because they are easier and cheaper to

process using standard metallurgical processing techniques like casting, extrusion and rolling [14, 15]. The constitution of matrix as well as size [16], volume fraction [17] and morphology of reinforcement, as well as processing method [18] used determine the end properties of the MMC fabricated. In obtaining optimal properties in a MMC, stiffer and stronger reinforcements compatible with the metallic matrix should be used, distribution of reinforcement should be near uniform and most importantly, good matrix-reinforcement interfacial integrity should be achieved [19, 20].

Aluminum, which has been widely studied since the 1920s, is the most popular matrix for metal matrix composites. In the 1980s, transportation industries started to develop reinforced aluminum matrix composites. Aluminum and its alloys are quite attractive due to their low density, their capability to be strengthened by precipitation, their good corrosion resistance, their high thermal and electrical conductivity, and their high damping capacity. Aluminum-based metal matrix composites have attracted considerable attention as structural materials in the aerospace, automotive, and transportation industries because of their high specific modulus and strength, and superior fatigue and creep resistances [1].

Since MMC's have been investigated by many researchers, improved properties are found when the size of the reinforcement is decreased [21]. It is expected that by scaling down the particle size in metal matrix composites to nanoparticles, some of the shortcomings of MMCs such as poor ductility, poor machinability and reduced fracture toughness may be overcome [22-26]. With recent advances in producing particles below 100 nm, it is expected that significant improvements can result from the incorporation of nanoparticles (NPs) in metals. A nano composite is a combination of two phases, at least one of which is in the order of nano size (less than 100 nm) in

at least one dimension. Accordingly, a metal matrix composite reinforced with nano sized ceramics can be termed as an MMNC's, a metal matrix nano composite. Theoretically, if a homogenous distribution of nano-reinforcements is present within the matrix grains, significantly improved mechanical properties could result due to a combination of Orowan strengthening and grain refining [27-32].

Although large amounts of work has been undertaken in the past decade to develop polymer matrix nanocomposites which many of such materials are already used in various applications, metallic composites containing nanoparticles can potentially offer many benefits over polymeric composites. The metallic matrix has inherent high temperature stability, high strength, high modulus, wear resistance and thermal and electrical conductivity. Aluminum nanocomposites have special weight reduction potentials which can be beneficial in the automotive and aerospace industries [33-35], primarily because these metal matrices have high strength and stiffness. They also have good thermal stability. However, a limited number of research has been reported to incorporate NPs homogenously in a metallic matrix. There can be many factors that lead to the undesirable non-uniform distributions of nanoparticles in a metal matrix, such as agglomeration, pushing of nanoparticles by growing dendrites, poor bonding between particles and matrix, and their accumulation in the grain boundaries. These challenges in synthesis and processing need to be overcome to achieve the desired benefits of reinforcement with nanosize particles [1, 2, 36-40].

For producing MMC's, there are two categories of production techniques: in-situ and ex-situ methods [15]. Ex-situ composites can be prepared simply by incorporating ceramic nanoparticles into alloys of aluminum via either powder metallurgy (PM) or liquid metallurgy. During recent decades, the ex-situ techniques, in which ceramic particles are added to molten metal and mixed prior to solidification, have been studied

extensively [17, 41-43]. However, due to many shortcomings including reaching a highly dispersed and non-agglomerated particles in matrix, none of these techniques satisfied the desired high yield strength which has been theoretically predicted.

In the in-situ method, the ceramic particles are introduced to the molten matrix via an exothermic reaction between the constituent elements of composites [41, 44-56]. Numerous work has been reported on the formation of in-situ ceramic particles of micron sizes in Al-based composites via reactive hot pressing, combustion synthesis, direct metal oxidation, etc. Aluminum has a high reduction potential and will reduce many oxides such as TiO_2 , ZrO_2 , CuO , ZnO , etc. Thus, the in-situ formation of particles inside aluminum matrix is expected to be a promising approach to fabricate MMCs and it has received much attention [44, 46, 49, 51, 57]. By the in-situ formation of MMCs a more homogenous and dispersed microstructure might be able to be achieved. Because in-situ reactions result in both a clean interface of reinforcement and small particle sizes, it might be possible to attain better mechanical properties by this method.

Conventional ceramic materials that are used to reinforce aluminum alloys include carbides, borides, nitrides, and oxides. Among these reinforcing particulates, titanium diboride (TiB_2) has been an attractive candidate since it exhibits high melting point (2900°C), high modulus (565 GPa), high hardness (2500 HV), and good thermal stability [58-61]. Furthermore, TiB_2 not only can form via an in-situ process, but it is also thermodynamically stable in liquid aluminum after formation. In addition, TiB_2 has been predicted to have a good potential to be incorporated effectively [62, 63] as a nanosize reinforcement in aluminum matrix due to its low interfacial energy [64, 65] and high probability of being captured by metal front during solidification [66].

Synthetically added TiB_2 particles (through ex-situ synthesis) tend to settle in liquid aluminum due to agglomeration when the particles are not wetted by the liquid metal due to the surface contamination inherent to the particles synthesis process [67, 68]. Elimination of contamination from the particles surface results in low contact angles which leads to an appropriate spreading condition [66, 69, 70].

In in-situ processing routes, the interface between matrix and reinforcement produced are relatively stable and impurity-free. In addition, the particles will be protected by the melt environment from oxidation. A strong bond between in-situ particles and the metal matrix is necessary to achieve an effective load transfer mechanism in the nanocomposites [6, 50]. Moreover, the in-situ formed reinforcing particles are finer in size and their distribution in the matrix is more uniform resulting in better mechanical properties than traditionally processed ex-situ composites.

In-situ syntheses of TiB_2 particles in a metallic matrix using an exothermic reaction by various techniques such as mixed salt reaction [71], mechanical alloying [72], liquid mixing [73], and self-propagating high temperature technique [74, 75] have been studied for decades. In most cases, processing of aluminum/ TiB_2 composites involved a two-step process where elemental titanium and boron first reacts with aluminum to form Al_3Ti and AlB_2 intermetallic. Subsequent reactions will lead to dissolution of these metastable intermetallics and the formation of Al_2O_3 and TiB_2 , which are thermodynamically most stable products in these systems. These procedures, however, led to mixtures of TiB_2 and some residual metastable byproducts. Al_3Ti has a tetragonal platelet structure having sharp edges that can be deleterious to mechanical properties especially elongation to failure of the final composite if this metastable phase is present in the final microstructure [52, 76, 77]. Therefore, it is

important to find a pathway to avoid the harmful influences of Al_3Ti formation on strength and ductility of the composite. Complete transformation to TiB_2 is more favorable where the final thermodynamically stable products are not forming as a result of intermediate dissolution.

Synthesizing surface clean nanoparticles using in-situ techniques will need to be accomplished using less expensive solidification routes which enable fabrication of large and complex components. By exploring a lower cost and more adaptable methods to manufacture metal matrix nanocomposites with improved ductility, such materials are expected to come into commercial use for a wide variety of applications, particularly where weight savings is essential. Understanding the mechanism of formation of in-situ ceramic particles inside liquid aluminum is crucial to designing system variables to achieve surface-clean nanoparticle reinforced composites. Acquiring the knowledge needed to achieve these goals is the primary motivation of this dissertation.

1.2 Research Objectives

The objectives for this work are to explore and evaluate the feasibility of fabricating aluminum based nano-composites using in-situ processing and assess the microstructural and mechanical properties of the synthesized composites.

This work is carried out in 3 phases:

- i. In phase I, the mechanism of reaction between molten aluminum, TiO_2 , and elemental boron will be investigated. Microstructural and analytical investigations will be used to describe the competing mechanisms of aluminothermic and borothermic reduction of titanium oxide in the presence of molten aluminum and boron through complex non-

equilibrium reactions. To investigate the reaction model, the effects of powder particle size on formation of reinforcing phases and microstructural evolution will be investigated.

- ii. In the second phase, a solidification processing pathway to synthesize bulk aluminum matrix nanocomposites containing sub-micron particles will be explored. Samples with selected temperature, time, and mixing techniques, designed on the basis of theoretical and experimental findings, will be synthesized to study the effect of compositional and processing parameters on the in-situ formation of nanoparticles. Selected microstructural and mechanical properties will be characterized to establish the process- properties relationship based on the measurements.

CHAPTER 2. LITERATURE REVIEW

2.1 Introduction

It is generally accepted that a reduction in the particle size aluminum of the reinforcements, as well as a strong mechanical at the interface without the presence of a chemical reaction product, would lead to an improvement in strength, ductility, machinability and fracture toughness [6, 37, 76, 78-81].

In order to attain complete understanding of properties of MMNC's, it is necessary to develop a relationship to predict mechanical properties of bulk composite as a function of its constituents and processing conditions. In recent years some modeling works has been done in this regard. In many cases, quantum mechanics models have been developed to predict properties. However, the effect of the particles on the on the micromechanics of deformation and strengthening mechanisms should be included to have better understanding.

Hall and Petch investigated the deformation and ageing of mild steel, They proposed a model to predict the yield stress as a function of grain size. It has been demonstrated that one of the most dominant mechanisms in determining mechanical properties of various crystalline metals is grain refinement. The empirical relation which is used to describe the effect of grain size on yield strength is expressed by:

$$\sigma_y = \sigma_0 + \frac{K_{H-P}}{\sqrt{D}}$$

Addition of nanoparticles to a metallic matrix, results in a reduction in grain size of the MMNC compared to unreinforced matrix. This improvement due to addition of nanoparticles and the consequent grain refining is considered as grain refinement strengthening mechanism in MMNC's.

When there is hard unsharable particles in the way of a dislocation movement route, the two segments of the dislocation line at either end of the precipitate attracts and a loop will form around the particle, which is the so-called Orowan strengthening. This constriction leads to the increase in dislocation density which eventually leads to high work hardening rate. It is well reported that contribution of Orowan mechanism in mechanical strength of MMC's is negligible since reinforcements are coarse and interparticle spacing is large. But, theoretically in MMNC's, where highly dispersed reinforcements with particle size less than 100 nm are incorporated, Orowan strengthening becomes important

In most of the models developed mainly these three major mechanisms of strengthening of MMNC's are proposed [39]. Individual mechanisms can contribute to the final yield strength either by arithmetic summation method, quadratic summation, or compound methods. Ferguson et al. proposed a model for dispersion strengthened alloys and MMNC's with consideration to stress and energy. They identified different parameters which influence the grain size dependent behavior such as volume fraction, and particle size [82]. Kim et al [30] reviewed different models in predicting strengthening of nanoparticles in magnesium alloys and reported that all these models have either over estimation or under estimation errors. Additionally, in most of models proposed to date the effect of work-hardening from post processing is also ignored. It has been shown that the most dominant mechanism works in MMNC's in most of synthesized nano composites is mainly governed by grain refinement.

Formation of a fine equiaxed microstructure rather than a coarse dendritic structure in aluminum casting has several benefits. Grain refinement includes the controlling of nucleation and growth of the solid. It promotes the formation of a fine, equiaxed grain

structure and improves not only the quality of the cast part but also the efficiency of the casting process.

Two methods are normally used to achieve a grain-refined microstructure: inoculation and dynamic nucleation. Dynamic nucleation is achieved by application of localized forced convection with rapid cooling[83]. It has been proposed that the convection causes dendrite arms to melt off from the mother dendrites, producing stable solid particles. These solid particles then act as secondary nuclei in the melt. The high density of these secondary nuclei results in a uniform and grain-refined microstructure. Several techniques to induce forced convection have been applied successfully using this grain refinement approach, including mechanical stirring, electromagnetic stirring, low-temperature casting, ultrasonic vibrations and gas bubbling.

An alternative way is by inoculation, a specific control of nucleation such by addition of grain refiner to the melt. It is the most widely used method to promote the formation of a fine, uniform, equiaxed grain structure. For inoculation, refinement of microstructure is achieved by addition of appropriate inoculants. The addition of titanium in various forms into aluminum alloys has been found to have a strong effect in nucleating the primary aluminum phase. The most widely used inoculants are those based on Al-Ti-B alloys, commonly Al-3 wt.% Ti-1 wt.% B, and Al-5 wt.% Ti-1 wt.% B which are added to molten aluminum at a typical level of 1-10 parts per thousand by weight. Experimental studies show that minor addition of Ti results in significant grain refinement by particles of Al_3Ti . Adding Ti and B simultaneously, the grain refining is improved [84]. The mechanism of operation of these refiners had been extensively studied, yet the exact mechanism of grain refinement is not fully understood [85-87].

To understand the development of the nucleation process it should be mentioned that there are two streams thoughts. These are the nucleant-particle theories and the phase-diagram theories. The two strands of theories are related to the two types of particles present in the Al-Ti-B master alloys; aluminides and borides. The particle theories, or boride theory, suggest that nucleation occurs on the borides in the master alloy (TiB_2 , AlB_2 , and $(\text{Ti,Al})\text{B}_2$), while the phase diagram theories explain grain refinement by nucleation on Al_3Ti , the peritectic phase.

Addition of heterogeneous nuclei for achieving grain refinement was first proposed by Cibula in 1949. In this grain refinement approach, numerous potent heterogeneous nuclei are dispersed in the melt, and a fraction of them become active nucleation sites during solidification and nucleate solid particles. In such a case, solid can form on a particle (by heterogeneous nucleation or by adsorption or wetting) at an undercooling smaller than that required for the onset of free growth, which constitutes the effective nucleation of a grain on the particle [88].

Mohanty et al. [86] attempted to evaluate the grain refinement potential of TiB_2 by adding synthetic TiB_2 crystals into a pure aluminum matrix. They have shown that borides are pushed to the grain boundaries and that no grain refinement is observed when there is no solute titanium present, which suggests that the lattice disintegrity between aluminum and the borides is large, indicating that borides are a poor nucleant. Although it was a successful method, there are still several drawbacks. Firstly, the synthetic TiB_2 added to the melt is not comparable with the ones formed in the melt by addition of master alloys due to their large crystallite surface area which easily can absorb oxygen and nitrogen. Oxidizing and nitriding at high temperatures changes their surface properties. Secondly, the size of synthetic TiB_2 crystals used in

their experiment is so large (5–10 μm). In general the average size of the TiB_2 particles in Al–Ti–B master alloy is about 0.5 μm which is much smaller than that of the synthetic TiB_2 crystal. Any change in the surface properties and morphologies of TiB_2 may affect its nucleation behavior.

The phase diagram theory suggests that grain refinement is caused by the peritectic reaction on the primary particles, Al_3Ti . Sigworth and Kuhn's [89] work shows that the prior existence of TiAl_3 nuclei is the fundamental reason for the nucleation of grains because TiAl_3 is found at the centers of aluminum grains, and there is a well-established orientation relationship between the lattices of the two phases. Although all experimental evidence is in line with expectations from the Al-Ti phase diagram, but does not explain refinement. However, this theory can be rejected by the fact that how addition of boron can enhance of for grain refinement.

Accordingly, neither the nucleant-particle theories nor the phase diagram theories are able to adequately explain why addition of boron to the Al-Ti system significantly improves grain refinement. Therefore, a combination of these theories or including other factors can explain the mechanism more easily [90].

2.2 In-situ Al/ TiB_2 composites

Aluminum and its alloys have been chosen as the matrix materials. predominantly because of low melting point, low density, reasonably high thermal conductivity, heat treatment capability, processing flexibility and their low cost.

As for the reinforcement, especially in recent years, TiB_2 reinforced aluminum MMCs have been extensively investigated. TiB_2 is chosen since it is particularly suitable as reinforcement for Al-based reactive sintered composites due to its high exothermic formation and thermodynamic stability in aluminum. The addition of TiB_2

to an aluminum matrix can greatly improve stiffness, hardness, and wear resistance without apparent loss of thermal expansion coefficient and electrical and thermal conductivities and high damping capacity compared to other ceramic reinforcements. The in-situ TiB₂ particulate reinforced aluminum composite can be obtained either by hot pressing and reaction sintering of powders (example is SHS¹ or XD™ process²) [44, 91] [92] [44, 93] or by in melt processing[45, 94-101].

In early 90s, Kuruvilla proposed using the XD process to form submicron TiB₂ particles in the aluminum matrix. In this process, Ti, and B are elementally blended with Al and the resultant blend is compacted and heated to about 800°C. In the presence of liquid phase, the Ti and B reacts exothermically to produce submicron size TiB₂ dispersoids, in the form of hexagonal and block-like crystals [91]. However, coarse Al₃Ti was also precipitated.

The melt processing approaches are also considered as either liquid-solid reaction (formation of TiB₂ particles in an aluminum matrix by addition of elemental powders or alloys of Al-Ti and Al-B and then heat them up to provide molten aluminum in which Ti and B diffuse and precipitate out TiB₂) or mixed salt reaction (mix salts of Ti and B are reacted in molten aluminum to form TiB₂ particles). In the following sections these types of Al/TiB₂ synthesis routes will be discussed in details.

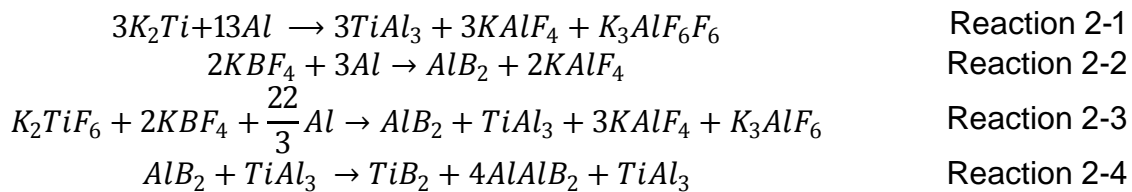
2.2.1 Mixed salt reaction or flux assisted synthesis (FAS)

Aluminum TiB₂ composite is fabricated by many researchers using mixed salts of potassium hexafluorotitanate (K₂TiF₆) and potassium tetrafluororate (KBF₄) in stirred aluminum melt [76, 102-106]. Donaldson et al. [107] examined the reaction between

¹ Self-propagating high temperature synthesis

² The XD process (patented by Martin Marietta) is an in-situ process which uses an exothermic reaction between two components to produce a third component.

salts and aluminum by XRD analysis of the slag, as well as the transfer efficiency of Ti and B from salt to aluminum by chemical analysis of the alloy. The formation sequence of TiB₂ from the reaction with K₂TiF₆ and KBF₄ is discussed in the view of the formation of a salt/metal emulsion and agglomeration by Fjellstedt [97]. The highly exothermic reaction with K₂TiF₆ will aid the formation of an emulsion, and Al₃Ti form that in a subsequent step transforms into TiB₂. It will also support high element transfer efficiency. The reaction with KBF₄ causes less heat to produce and the tendency towards formation of an emulsion and thus lower transfer efficiency resulting in a sluggish formation of AlB₂. Simultaneous additions of K₂TiF₆ and KBF₄ increase the transfer efficiency but will cause the formation of stringer defects in a layered structure. The following reaction sequences are suggested:



In salt mix process, salt plays two roles; 1- acting as activator, decreasing activation energy and accelerating the reaction 2-reacting with Al₂O₃ to form dross. However, due to different chemical reaction involved, many unfavorable by-products are also obtained in all reported composites. In addition, Al₃Ti is also unavoidable product of these mixtures. In the report released by Lakshmi[103], in which the effect of processing parameters on the size and wt% of TiB₂ has been studied, it has been shown that TiB₂ particles were formed after 10 min of reaction at 800 °C. Reaction between K₂TiF₆ and aluminum occurred at a higher rate than between KBF₄ and Al. Thus at the early stage of reaction, TiB₂ formation is less complete and intermediate TiAl₃ forms. Excess TiAl₃ nucleates as a thin layer on the surface of TiB₂ particles. Alternatively Al₃Ti may also nucleate as individual particles. Wang et al [108] studied

the process parameter in the same flux assisted system and reported that although TiB_2 is the more thermodynamically stable phase compared with Al_3Ti , it requires a longer time to produce this phase. In the presence of excess boron, in the form of AlB_{12} , Al_3Ti will decompose fast by reacting with AlB_{12} to form TiB_2 .

The mechanism which was proposed for the salt mix reaction technique is described below.

Initially, TiB_2 forms at the interface between aluminum and the flux. The formation and dispersion of this kind of boride particle is strongly influenced by the alloy elements that modify the Al/TiB_2 interfacial energy.

Ti and B disperse into the aluminum melt when K_2TiF_6 and KBF_4 are reduced by aluminum and subsequently react to form TiB_2 particles. The titanium and boron which exists in the aluminum melt are either in the form of alloying elements or as compounds such as Al_3Ti and AlB_{12} . At higher temperatures and longer holding times, AlB_{12} and Al_3Ti will decompose to form AlB_2 and TiB_2 . The particle size and morphology are largely affected by processing condition, such as temperature, holding time and flux composition.

The growth behavior changes in the presence of surface-active elements such as Mg, Li, and B which lower interfacial energy [109]. Alloying elements can also affect the stability of the precipitated phases during the fabrication of in-situ reinforced Al/TiB_2 composites [47]. The results show that the addition of alloying elements, such as Mg, Cu, Zr, Ni, Fe, V, and La promotes the formation of Al_3Ti and TiB_2 phases. Particularly, Zr has the most pronounced effect among these alloying elements. In addition, alloying elements can hinder the formation of AlB_2 to a small extent. The calculations also show that it is easier for magnesium to react with the salts to

form TiB_2 than aluminum during the fabrication of in-situ reinforced Al/ TiB_2 using the flux-assisted synthesis (FAS) technology. Magnesium, at high concentration, in Al-Ti-B-Mg system, can decrease the excess free energy of TiB_2 , thus promoting TiB_2 phase formation. The same role can be attributed to other solutes as V and Zr [110].

The mechanical properties of the microcomposites using salt mix technique have been reported by many researchers [18, 76, 111-116]. Comparison between unreinforced and micron particle reinforced composites show that yield strength and tensile strength increase about 40-60% while there 20-30% increase in modulus. However, there is a significant reduction in ductility as a result of increase in TiB_2 particle content [117].

2.2.2 Liquid Mixing Synthesis

TiB_2 particles form in the aluminum melt by addition of elemental powders or alloys of Al-Ti and Al-B. So far, there is a limited amount of reports on synthesis of TiB_2 particulates prepared by in-situ reaction in molten aluminum. Wang et al. studied the possibility of formation of TiB_2 particulates in molten aluminum by preparing a cylindrical pressed preform of elemental powders of Al, Ti, and B follow by molten aluminum infiltration. The molten aluminum flows and spreads over the surface of titanium powders. The reaction temperature, in this case, is lower than the melting point of titanium (1953 K). As soon as the molten aluminum spreads over the surface of titanium powders Al_3Ti first forms [118].

Other researchers added elemental powders at the stoichiometric ratio to the molten aluminum, it has been shown that that Al, TiB_2 , and Al_3Ti forms as the final products. Al_3Ti has sharp edges which can deteriorate mechanical properties of the final composite in large extent [113].

Tee et al. showed that addition of copper into an aluminum matrix as an alloying element enhanced TiB_2 nucleation. However, it also increase Al_3Ti content which eventually caused 68% loss in ductility. They also experimentally verified that when the holding time is too short, TiB_2 forms is low content and when the holding time exceed an optimum , Al_3Ti flakes are coarsened [117].

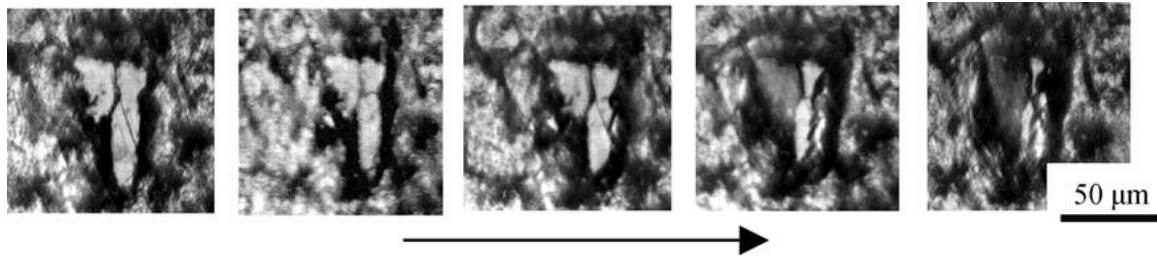


Figure 1 Optical micrographs of a dissolving $TiAl_3$ particle obtained through video frames during hot stage observations [119].

Other stream of experiments in liquid mixing synthesis is the use of Al-Ti and Al-B master alloys [77, 90]. Emamy et al. [119] investigated the progress of in-situ formation of TiB_2 by mixing molten master alloys of Al-Ti and Al-B using hot stage microscope (Figure 1). The formation of TiB_2 particles occurred via diffusion of boron atoms through $TiAl_3$ particles interface, thereby reacting to form fine TiB_2 particles. The sequence of TiB_2 formation can be written in the following steps; 1- The initial Al-Ti master alloy already has Al_3Ti , therefore, boron atoms move toward $TiAl_3$ particles in a gap at the $TiAl_3$ surface. 2- Boron atoms diffuse through TiB_2 particles since it has very small atomic size and continues to grow. 3- Natural cracks on $TiAl_3$, particles, which results in further fragmentation of $TiAl_3$ helps further dissolution of $TiAl_3$ particles, increasing the rate of TiB_2 and finally ring like TiB_2 forms. In all up to date literature survey, the size of TiB_2 forms is a factor of Al_3Ti size which is not easy to be controlled. Another problem with current technology is the residual Al_3Ti , which drops the final properties of the composites particularly ductility.

2.2.3 Self-propagating high temperature synthesis (SHS)

In 1994 [120], SHS followed by high pressure consolidation, was performed to synthesis Al/ TiB₂ and Al/ TiC composites. Al (44 μm), Ti (44 μm), B (1-5 μm) powders were mixed, ball milled, and then ignited by passing through electric current. Ma et al was the first group reported incorporating B and B₂O₃ into the Al- TiO₂ systems to synthesize in-situ aluminum based composites by a reactive sintering process termed XD™ technique [44, 93, 121]. The interface obtained between TiB₂ particles and aluminum matrix was clean and no consistent crystallographic orientation relationship was found. The composite also exhibit excellent elevated temperature strength up to 300 °C [121]. In this process it was found that Ti displaced from the reaction between TiO₂ and Al reacts with B to form TiB₂ instead of aluminum forming Al₃Ti. The size of in-situ formed Al₂O₃ and TiB₂ is less than 2 μm; the Al₃Ti block-like compound with the size of about 20 μm was also observed. When the amount of B/TiO₂ reaches a 2/1 ratio (stoichiometry ratio of B/Ti in TiB₂), the Al₃Ti in the composite can be completely eliminated. Their EDS analyses revealed that the white blocks observed in the microstructure are Al₃Ti, while the black particulates are Al₂O₃. The TEM examinations also verified that the in-situ Al₂O₃ and TiB₂ particulates had an equiaxed shape. It was reported that in liquid sintering process the formation of in-situ TiB₂ is mainly controlled by the diffusion of Ti. Ma reported coarse Ti and B powders would reduce the amount of nucleated TiB₂, increase the diffusion path of Ti and slow the diffusion of Ti in molten aluminum. Furthermore, the formation of a certain amount of Al₃Ti cannot be avoided in coarse Ti-B powder system.

The size and shape of the in-situ formed TiB₂ particulates is mainly controlled by the diffusion of Ti atoms and therefore, the growth of the TiB₂, whereas the formation or elimination of Al₃Ti is determined by both the nucleation of TiB₂ and the diffusion of

Ti atoms. When fine TiO_2 powder is employed, fine and equiaxed TiB_2 particulates are formed in-situ due to a short diffusion distance and rapid diffusion rate of Ti. However, in systems like $\text{TiO}_2\text{-Al-B}_2\text{O}_3$, where both rates of B reduction and its dispersion into molten aluminum are relatively slow there is a little amount of the nucleation of the TiB_2 in the system and also the formation of the Al_3Ti cannot be avoided [93]. Hence, in order to promote the formation of fine TiB_2 particulates and the elimination of brittle Al_3Ti , it is necessary to increase the nucleation rate of TiB_2 and the diffusion rate of Ti atoms. However, the diffusion of Ti atoms may not be the main controlling step in the TiB_2 formation. A rapid growth of TiB_2 occurs immediately after the nucleation of such particulates. Therefore, the formation rate of the in-situ TiB_2 particulate is controlled by both nucleation and growth of TiB_2 .

2.3 In-situ Al/ TiB_2 nanocomposites

In spite of the fact that there is an abundance of literature on the in-situ synthesis of TiB_2 particles in various metal matrices, but there are only few studies which synthesized nano TiB_2 particles. Most of conventional ceramic reinforcements have poor wetting with molten aluminum. In case of TiB_2 , the commercially available nanosized TiB_2 particles are either expensive or not scalable or they have a surface carbon-coating inherent to the arc-plasma synthetic process, which promotes the oxidation reactions and hinders NP incorporation into the metal melt. These shortcomings make them not useful for reinforcing material in solidification processing of MMNCs by ex-situ techniques. However, during in-situ processing particles will be protected by melt environment from oxidation and a clean and impurity-free surface particles. TiB_2 can be considered as an excellent candidate as reinforcement in aluminum matrix nanocomposites since it has a low interfacial energy and good wettability with aluminum. Additionally, it has a high hamakar constant compared to

other types of reinforcements [122-124] which enhance particle distribution after solidification within grains.

In-situ copper matrix composite with 3.5 wt.% TiB was prepared by reactions of B_2O_3 , carbon and titanium in copper–titanium melt by rapid solidification. Other groups claimed formation of nano TiB_2 particles in the copper matrix using synthetic method combining preliminary mechanical treatment of initial powder mixtures in high-energy ball milling, self-propagating exothermic reaction and subsequent mechanical treatment of the product [125]. The in-situ formed TiB_2 particles with a size of about 50 nm exhibited a homogenous dispersion in the copper matrix when prepared through stir mixing followed by rapid solidifying. The mixture of B_2O_3 and carbon powder (as a reductive agent) at temperatures between 1400 and 1500 °C was introduced into the melts of Cu–Ti alloy by argon carrier gas while it was agitated by the propeller. TiB_2 was formed by the carbothermic reduction of B_2O_3 in the melt. The in-situ reaction was carried out for an appropriate length of time to ensure the complete conversion of titanium in the melt to TiB_2 and the elimination of the CO_2 [126]. Though in this paper the formation of nanoparticles has been only reported, the mechanism of nano particle formation has not been investigated.

Guo [127] used another technique to incorporate nanoparticles in the copper matrix combining in-situ reaction with rapid solidification. The bulk TiB_2 copper composites prepared by an in-situ reaction equipment for double-beam melts. The basic idea in this study was to combine in-situ reaction with rapid solidification techniques at the same time to prepare nano TiB_2 particles dispersion strengthened copper alloy. The average size of nano TiB_2 particles distributed in copper matrix synthesized in

optimized condition is about 20 nm. However, one of the main shortcomings of the current technique is that the equipment used cannot be easily scaled up into industry.

An Al₂O₃- TiB₂ ceramic matrix nanocomposite with a mean crystallite size of 35–40 nm was synthesized by the high energy ball milling at some optimum milling time on Al, B₂O₃ and TiO₂ powders [128-131]. It is also reported the titanium diboride were synthesized after ball-milling for 10 to 15 hours and the reaction was found to be completed during the milling process. The powder obtained had a particle size of about 50 nm after 100 hours milling and seemed to be relatively mono disperse [132].

Lee et al reported a three step process [71] in which TiB₂ nanoparticles separately formed and washed in acid by in-situ reaction between salts with a high intensity ultrasonic field that restricts the particle growth and resulted in small TiB₂ particles. Pellets of Al- TiB₂ master nanocomposite (50 wt % in TiB₂) was fabricated and used to prepare the final nanocomposite with desired composition. Scaling up of the proposed three-step process is expensive and not scalable.

2.4 Ultrasonic Cavitation–Based Solidification Processing

It is extremely difficult to disperse nano particles uniformly in liquid metals because of their poor wettability in metal matrix and their large surface-to volume ratio, which easily induces agglomeration and clustering [133].

Formation of small liquid-free zones or vapor cavities and bubbles in a liquid which is the result of forces acting upon the liquid is called cavitation. Cavitation usually happens when a liquid is exposed to rapid changes of pressure that cause the formation of cavities where the pressure is relatively low. When subjected to higher pressure, the voids implode and can generate an intense shockwave.

ACOUSTIC CAVITATION

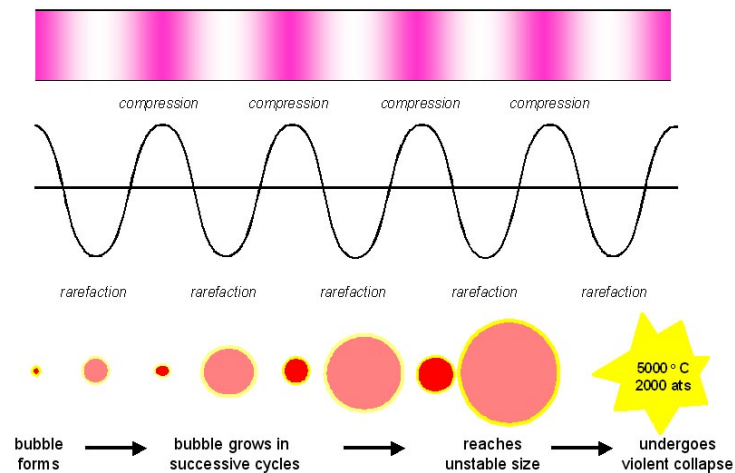


Figure 2 Generation of an acoustic bubble

Power ultrasound improves chemical and physical changes in a liquid through the generation and following destruction of cavitation bubbles. Like any sound wave ultrasound is propagated via a series of compression and rarefaction waves induced in the molecules of the medium through which it passes. At adequately high power the rarefaction cycle may exceed the attractive forces of the molecules of the liquid and cavitation bubbles will form. Such bubbles grow by a process known as rectified diffusion. During its expansion phase, a small amount of vapor from the medium enters the bubble and is not fully ejected during compression. The bubbles grow over a period of a few cycles to an equilibrium size for the particular frequency applied and when they collapse in subsequent compression cycles, it generates the energy for chemical and mechanical effects. Figure 2 and Figure 3 schematically illustrates the generation of an acoustic bubble and its collapse.

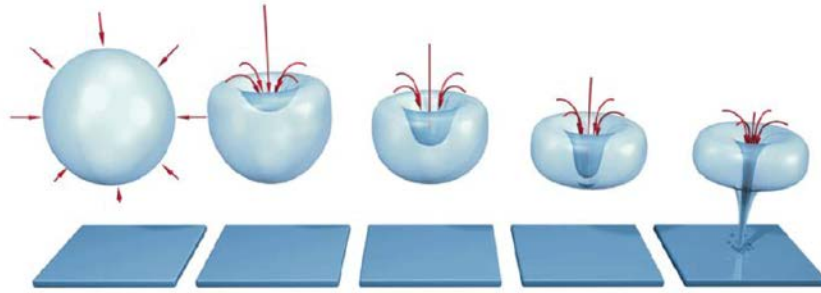


Figure 3 Schematic of cavitation bubble collapse

Cavitation bubble collapse is a remarkable phenomenon induced throughout the liquid by the power of sound. In aqueous systems at an ultrasonic frequency of 20kHz each cavitation bubble collapse acts as a localised hotspot generating temperatures of about 4,000 K and pressures in excess of 1000 atmospheres. During the rarefaction phase, the surface of the cavities expands to many times that of stable bubbles, and the pressure inside the cavities decrease to almost zero. During the compression phase, cavities collapse, and suddenly the pressure goes up. Acoustic cavitation can produce dramatic effects on powders suspended in a liquid (Figure 4). Surface imperfections or trapped gas can act as the nuclei for cavitation bubble formation on the surface of a particle and subsequent surface collapse can then lead to shock waves which break the particle apart. Cavitation bubble collapse in the liquid phase near to a particle can force it into rapid motion. Under these circumstances the general dispersive effect is accompanied by interparticle collisions which can lead to erosion, surface cleaning and wetting of the particles and particle size reduction (Figure 4)

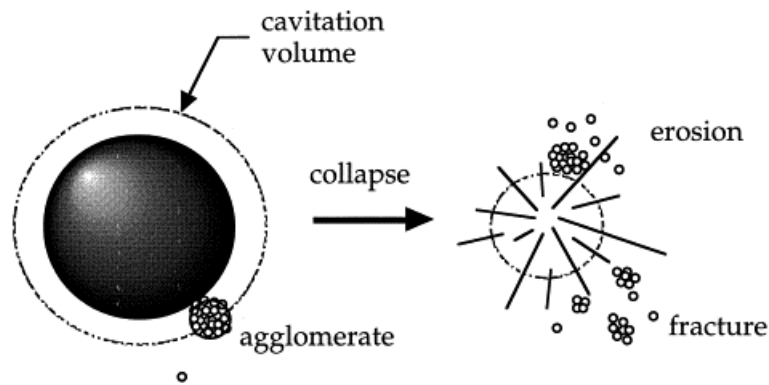


Figure 4 The cavitated bubble collapse and interparticle collisions lead to erosion, surface cleaning and wetting of the particles and particle size reduction

The research of ultrasonic vibration for metallurgical applications can be dated back to 1878 which are used to refine microstructures, reduce segregation, and improve secondary phase formation and distribution [134]. Ultrasonic waves can be used for degassing to lessen the porosity in solidified metal. Mechanisms for grain refinement under ultrasonic vibrations have been proposed. They are related to large instantaneous pressure and temperature fluctuations in the melt. These pressure and temperature fluctuations are likely to induce heterogeneous nucleation in the melt. They are also likely to promote dendrite fragmentation by enhancing solute diffusion through acoustic streaming [135].

To explain the action of ultrasonic in liquid metal and how cavitation plays a key role in dispersion of nanoparticles a simplified model was proposed by Li et al. [136]. Figure 5 shows two nanoparticles captured inside melt and two forces- intrinsic van der Waals force and capillary force applied by the melt surface tension- hold two nanoparticles together in the melt. The magnitude of these forces is a function of the particle mean distance. In this model, maximum amount pressure required to separate the two nanoparticles are estimated by adding the maximum of each of these two forces. On the other hand, in order to compare the pressure generated by ultrasonic cavitation with the required minimum pressure for the nanoparticle (In their model, they

particularly studied the SiC nanoparticles with a radius of 30 nm in aluminum alloy A365), a simple model involving a single cavitation bubble in the aluminum melt was studied. The calculated value of the cavitation pressure can reach up to 6,000atms, which is significantly higher than the required minimum bubble pressure (650 atms) to separate the two SiC nanoparticles with a diameter of 30nm. Therefore, it is theoretically understood and experimentally validated that ultrasonic cavitation could result in the dispersion of nanoparticles.

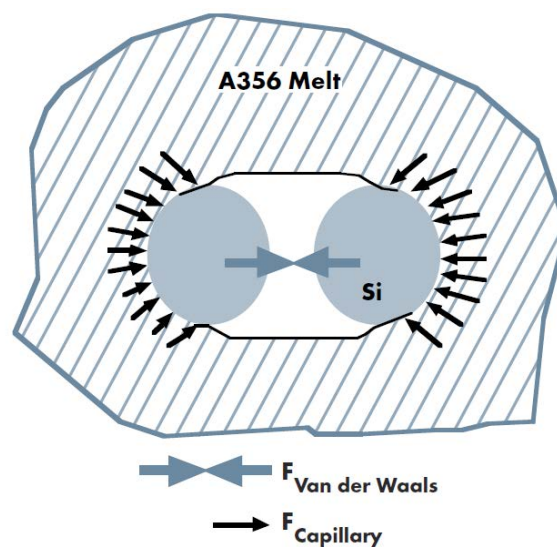


Figure 5 A simplified model for two SiC nanoparticles in aluminum alloy melt and the forces keep these particles together

2.5 Summary and Conclusion

Metal-matrix nanocomposites and the potential use of aluminum matrix particulate reinforced composites were reviewed. A brief introduction of different strengthening mechanisms in particulate reinforced matrix was discussed. Among them, it has been shown that Hall-Petch strengthening and Orowan strengthening can give outstanding enhancement to metal matrix nanocomposites.

Solidification processing techniques to synthesize metal matrix composites were reviewed, In particular, the ex-situ and the in-situ metal matrix composite production

techniques were discussed. Although most of the work done on solidification processing of composites is using ex-situ route, this approach appears to have many shortcomings and difficulties due to the impurities such as oxides, carbides, and nitrides which exist on particles' surface at elevated temperature as well as issues in dispersing particles uniformly in the matrix. These concerns are highlighted when the particle size is scaled down to nano size. High amount of surface area available in nano particles, increase the tendency to any oxidation reaction as well as more possibility of agglomeration. However, it is then theoretically shown that ultrasonic mixing can potentially help the deagglomeration of particles and enhance precipitation and nucleation of second phase in the molten metal.

Although in-situ fabrication of ceramic reinforcements in a metal matrix have been studied extensively, a limited number of MMNCs have been synthesized using in-situ processing. Particles synthesized by in-situ processing usually have a clean and contamination free surface which is attributed to the fact that particles will be protected by melt environment from oxidation. Among many in-situ synthesized particles, titanium diboride has high stiffness and hardness (only less than diamond, BN and B₄C) and has high mechanical strength 750 MPa. Additionally, in contrast to most ceramics, it is electrically and thermally conductive. TiB₂ is a thermodynamically stable compound which has strong interfacial bonding and good wettability with aluminum which helps a more uniform distribution in the matrix. In addition, having high hardness, low density, high melting temperature, and high corrosion resistance makes aluminum containing TiB₂ particles a potential candidate for high strength engineering composite.

Al/TiB₂ Composites prepared by adding synthetic TiB₂ crystals into pure aluminum matrix have not shown outstanding properties, while the intrinsic problems of ex-situ techniques as well as poor surface properties of particles due to oxidation and nitration lead to a disintegrate between particles and matrix. Secondly, the size of synthetic TiB₂ crystals is generally large (5–10 μm).

The most versatile and inexpensive solidification processing techniques for synthesis of Al/ TiB₂ composites studied is mixed salt reaction processing. This approach results in large micron size and many unfavorable by-products which may limit their application. Yet, only a limited number of TiB₂ reinforced nano or sub-micron composites have been synthesized to date. Additionally, there is limited number of available literature which studied the mechanism of the formation of boride particles in the melt. More knowledge on the reaction mechanism as well as identifying the parameters which control particle size and distribution, and eventually mechanical properties, is needed.

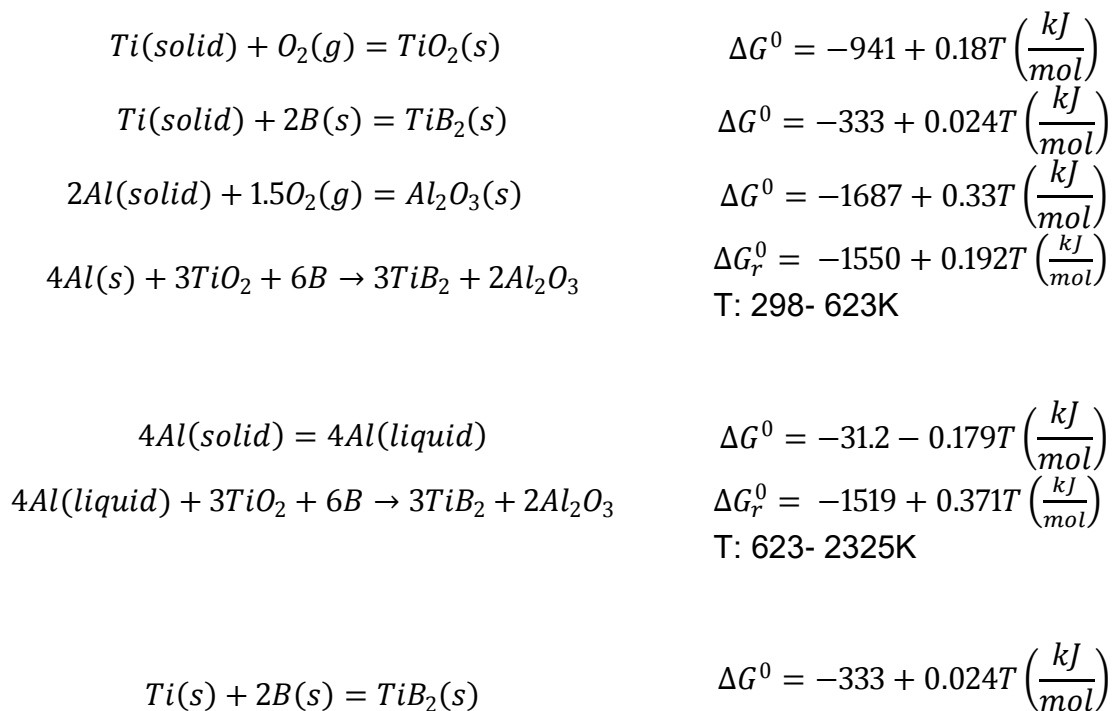
CHAPTER 3. REACTION MECHANISM [137]

The purpose of this chapter is to study the reaction path in the Al- TiO₂-B system during the transformation of titanium oxide into titanium diboride and alumina. Structural and compositional changes were examined to verify to investigate the reaction model in the system. Reaction products of the reduction are examined by interrupting the reaction at different reaction times of isothermal treatments. The reaction mechanisms involved in the transformation processes of the parent phases will be discussed.

3.1 Thermodynamic Considerations

In order to evaluate the feasibility of formation of TiB₂ by in-situ reaction in Al-TiO₂-B system, the temperature (T) dependence of Gibbs free energy change (ΔG_0) of possible reactions is discussed.

The following set of reactions have been used to estimate the Gibbs free energy of formation of TiB₂ [138]:



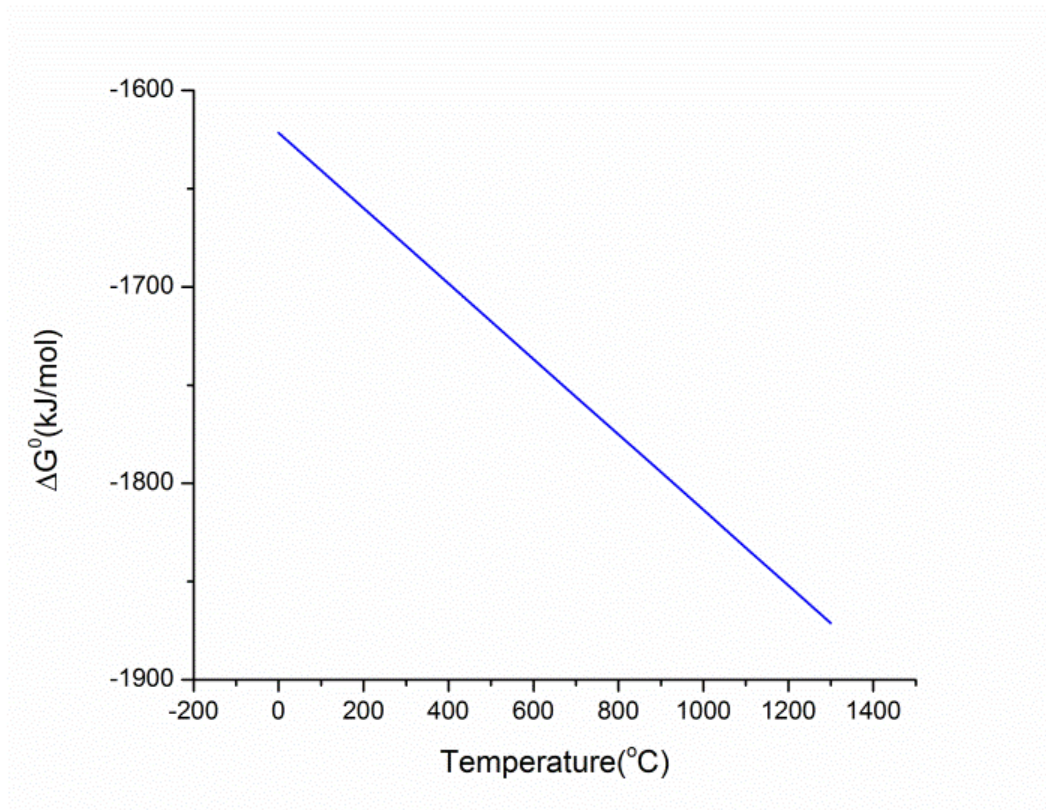
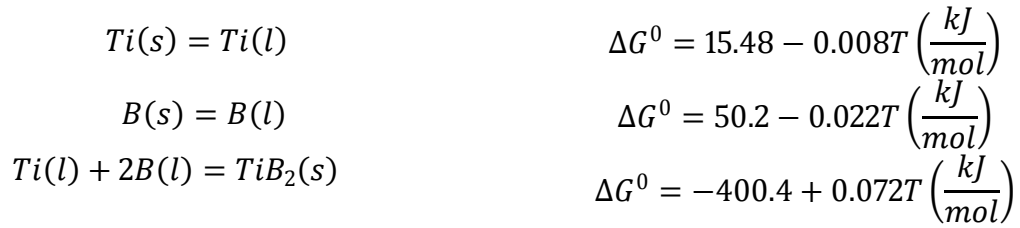


Figure 6 The temperature dependence of Gibbs free energy change (ΔG_0)

Figure 6 shows the temperature dependence of Gibbs free energy change of TiB_2 . It can be clearly seen, the formation of TiB_2 has a negative free energy, and therefore, the reaction is highly exothermic, which indicates that the reaction is possible since there is a large driving force.

The formation of other phases in the Al-TiO₂-B system, such as TiB, Al₃Ti and AlB₂, are also possible. The formation of these phases can be evaluated by comparison of Gibbs free energy of the formation of the following reactions (Figure 7).



This plot clearly shows that the ΔG of formation of TiB_2 is much more negative than those for other reactions in the temperature range between 200- 1400 °C. Therefore, if the boron content in the system is enough, TiB_2 phase will more likely form, rather than to Al_3Ti and AlB_2 phases.

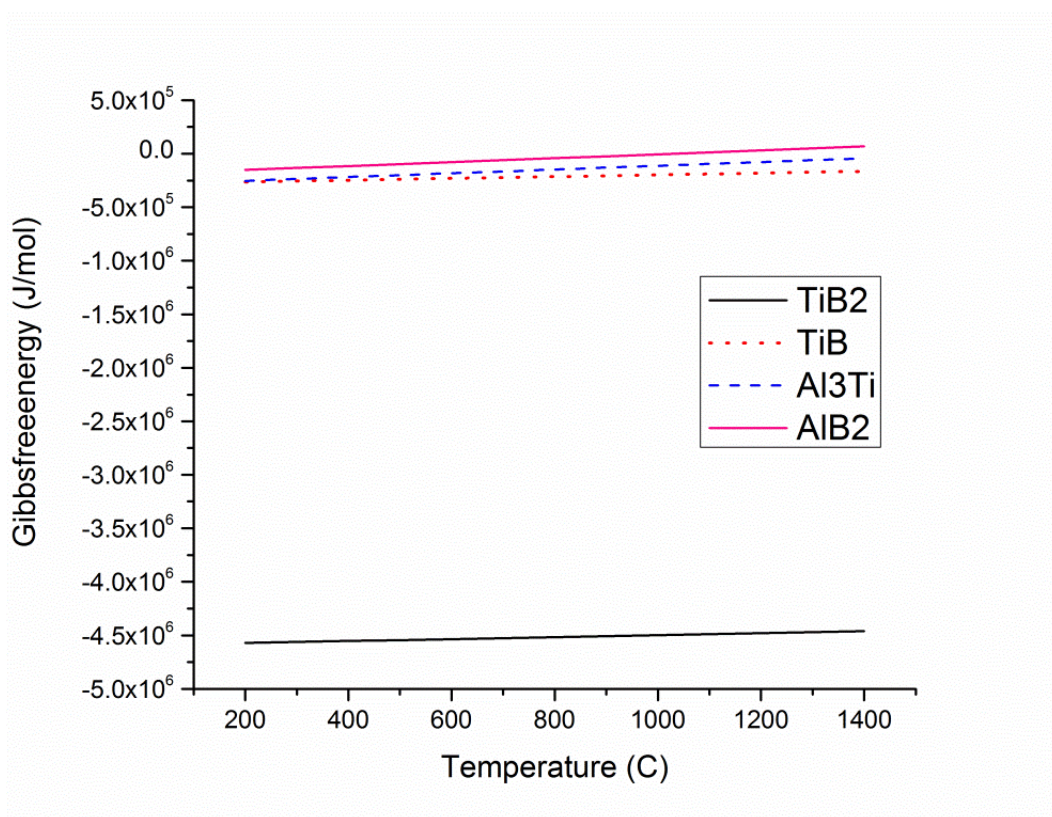
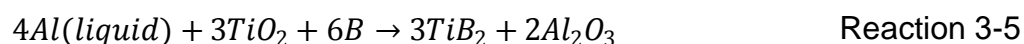


Figure 7 comparing free energy changes by temperature of different possible compounds in Al-Ti-B system

3.2 Materials and Experimental

Acros Organics™ Titanium(IV), 98+% Anatase powders with an particle diameter of >44 μm, Sigma- Aldrich Titanium(IV) oxide, anatase nanopowders with particle diameter <25 nm, boron powder, 94-96% amorphous, with an average particle diameter of <5 micron, and aluminum 99% powder with an particle diameter of >74μm,

were weighed according to the stoichiometry of reactants to form anticipated products based on Reaction 3-5, with 50% excess aluminum and then mixed through extensive acoustic mixing using a Resodyn-LabRAM Mixer to ensure homogeneity.



To investigate the reaction path, the powder mixtures were heated at 10 °C/min to 760 °C, 900 °C, 990 °C and 1200 °C and held isothermally for selected periods of time followed by rapid cooling as indicated in Table 1 using a DSC/TGA (TA Instrument Q600) with a TA data acquisition interface. About 20 mg of powder mixture of reactants were placed in an alumina sample crucible. Alumina powder was used as the reference standard. An argon atmosphere was created by stopping the air backfilling using hose in water technique which is shown schematically in Figure 8. Before each run, the system was flushed with argon to ensure a pure argon atmosphere in the chamber. In addition to isothermal heat treatments, parallel runs in the temperature range 25–1200 °C were performed. DSC traces were repeated to ensure reproducibility. DSC temperature calibrations were made using aluminum and silver (in argon) standards heated at 20 °C/min.

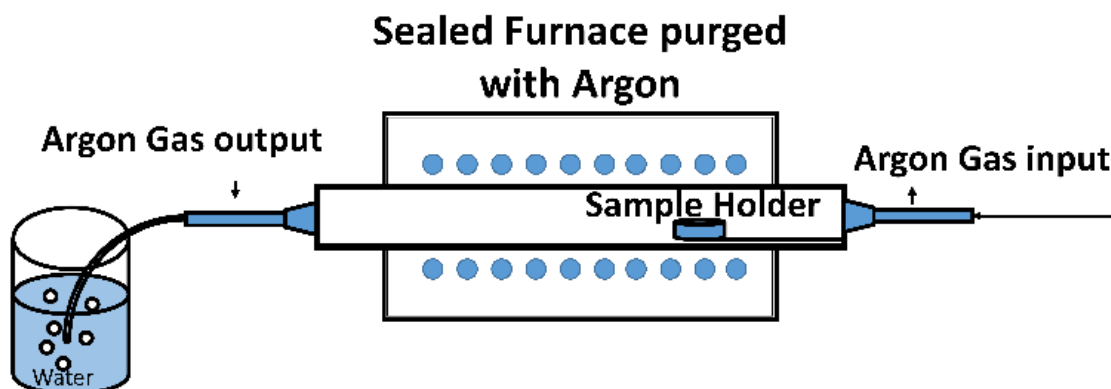


Figure 8 Schematic showing DSC/TGA chamber equipped with Controlled back filled atmosphere.

The samples retrieved from the DSC were examined by X-ray diffraction (XRD) using a Scingtag XDS 2000 diffractometer, with a step size of 2 degrees/min in 20-70 degree range, Scanning and Transmission Electron Microscopy, Energy Dispersive Spectroscopy for phase identification, microstructure observation, and qualitative elemental analysis, respectively.

SEM was carried out using a Hitachi S-4800 Ultra High Resolution Cold Cathode Field Emission Scanning Electron Microscope (FE-SEM) at 10 kV. Elemental analysis of the retrieved powders was performed using Hitachi S-4800 FE-SEM equipped with a Bruker Quantax EDS system. The thin window silicon drift detector (SDD) allows the detection of elements boron and higher. Transmission electron microscopy (TEM) was carried out using a Hitachi H-9000NAR with attached Noran Energy Dispersive Spectrometer and a Gatan multi scan CCD camera controlled by an Emispec Vision 2 data acquisition system. Powder samples were analyzed by TEM by first ultrasonically dispersing the nanoparticles in alcohol followed by depositing a drop of the dispersion onto a porous carbon film on 300 mesh copper grids using an eyedropper and subsequently allowing the alcohol to evaporate in air.

3.3 Results and Discussion

The DSC traces of pure aluminum powder and the Al- TiO₂-B powder mixture are shown superimposed on each other in Figure 9. An endothermic peak is observed in both specimens at 676 °C corresponding to the melting of the 99% pure aluminum. When the Al- TiO₂-B mixture is heated to a higher temperature (>760 °C), the aluminum completely melts and becomes a stable molten system, and then at 759 °C an endothermic valley followed by an exothermic peak which onsets at 940 °C are observed. The exothermic peak may be attributed to a temperature range in which some exothermic reactions might simultaneously take place. However, it is not possible to separate the contribution of reactions forming the broad exothermic peak.

Table 1 List of products formed through heating and isothermal reactions in Al-TiO₂-B system

| | Stage I | | Stage II | Stage III | Stage VI | Stage V | | | | | |
|-----------------------|----------------------|----------------------|----------------------------------------------------------------------|----------------------------------------------------------------------|----------------------------------------------------------------------|-------------------------------------|--------------------------------|--------------------------------|--------------------------------|--------------------------------|------|
| Temp. (°C) | 760 | | 900 | | | | | | | 990 | 1200 |
| Time (min) | 0 | 30 | 0 | 5 | 10 | 30 | 0 | 30 | 0 | | |
| XRD Identified phases | Al | Al | Al | Al | Al | Al | Al | Al | Al | Al | |
| | TiO ₂ (A) | TiO ₂ (R) | TiO ₂ (R) | TiO ₂ (R) | TiO ₂ (R) | TiO ₂ (R) | Al ₂ O ₃ | Al ₂ O ₃ | Al ₂ O ₃ | Al ₂ O ₃ | |
| | | | Al ₂ O ₃ | Al ₂ O ₃ | Al ₂ O ₃ | Al ₂ O ₃ (↑↑) | TiB ₂ | TiB ₂ | TiB ₂ | TiB ₂ | |
| | | | TiBO ₃ | TiBO ₃ | TiBO ₃ | TiBO ₃ | Al ₃ Ti | Al ₃ Ti | Al ₃ Ti | Al ₃ Ti | |
| | | | (Ti _{0.99} ,Al _{0.1}) ₂ O ₃ | (Ti _{0.99} ,Al _{0.1}) ₂ O ₃ | (Ti _{0.99} ,Al _{0.1}) ₂ O ₃ | Ti ₄ O ₇ | Ti ₄ O ₇ | Ti ₄ O ₇ | Ti ₄ O ₇ | Ti ₄ O ₇ | |
| | | | | | | Ti ₃ O ₅ | Ti ₃ O ₅ | Ti ₃ O ₅ | Ti ₃ O ₅ | Ti ₃ O ₅ | |
| | | | | | | Ti ₂ O ₃ | Ti ₂ O ₃ | Ti ₂ O ₃ | Ti ₂ O ₃ | Ti ₂ O ₃ | |
| | | | Al ₃ Ti | Al ₃ Ti | Al ₃ Ti | Al ₃ Ti | | | | | |
| | | | | TiB ₂ | TiB ₂ (↑↑) | TiB ₂ (↑↑) | | | | | |
| | | | | B ₂ O ₃ | B ₂ O ₃ | B ₂ O ₃ | | | | | |

* Boron is present although it was not detected by XRD
 ↑↑ indicates significant increase in quantity

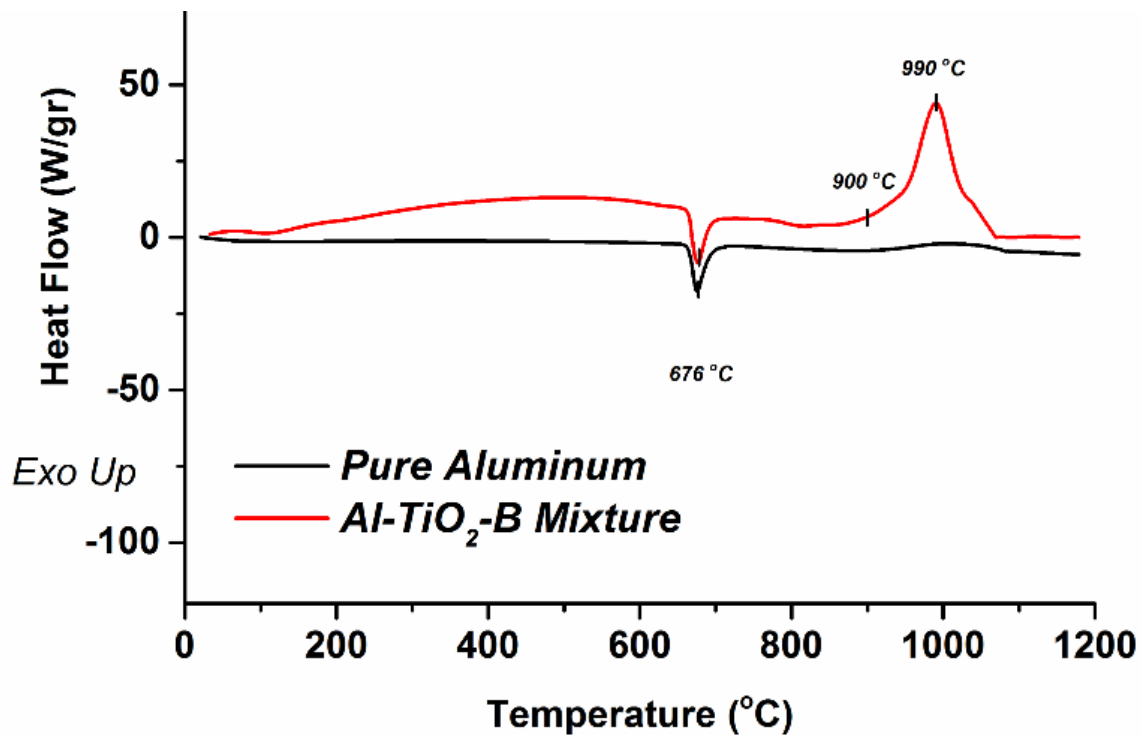


Figure 9 DSC trace of mixture of a) Pure aluminum b) Al-TiO₂-B heated in the temperature range of 200–1200°C.

To further examine this reaction, isothermal heat treatments were conducted at 760, 900, 990 and 1200 °C as described in Table 1 and the obtained products were analyzed by XRD, SEM, and TEM. The X-ray diffraction patterns and the list of products formed after thermal processing are shown in Figure 10 and Table 1, respectively. Prior to heating, only the diffraction peaks of TiO₂ and aluminum exist. Boron was not detected by XRD; however, this product is interpreted to be present in an amorphous form. XRD results suggest that the reduction of TiO₂ by boron and aluminum is more complicated than depicted by Reaction 3-5 which only shows the formation of the thermodynamically stable reinforcing phases.

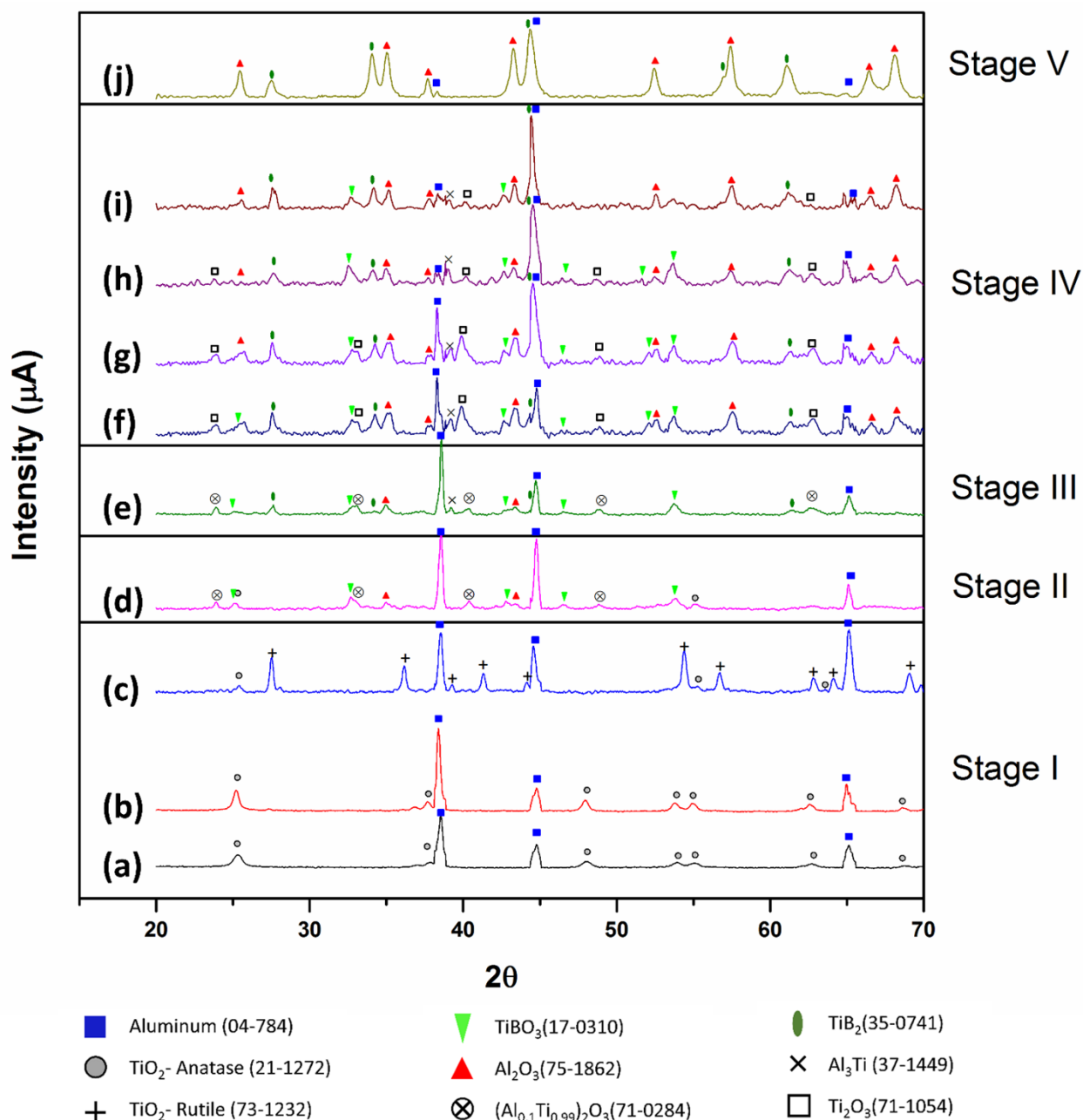


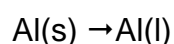
Figure 10 X-ray diffraction patterns of the Al-B-TiO₂ Mixture and samples after thermal processing (a) Unheated mixture (b) Heat treated at 760 °C and quenched (c) Heat treated at 760 °C followed by 30 min isothermal and quenched (d) Heat treated at 900 °C and quenched (e) Heat treated at 900 °C followed by 5 min isothermal and quenched (f) Heat treated at 900 °C followed by 10 min isothermal and quenched (g) Heat treated at 900 °C followed by 30 min isothermal and quenched (h) Heat treated at 990 °C and quenched (i) Heat treated at 990 °C followed by 30 min isothermal and quenched (j) Heat treated at 1200 °C and quenched.

The X-ray diffraction patterns obtained on products heat treated below the exothermic peak observed in the initial scan suggests that no significant reaction between Al, B, and TiO₂ have occurred (Stage I in Figure 10). As the temperature increases, the aluminum melts and dissolves the boron, there are various reactions between the liquid metal and the oxide that contribute to the formation of intermediate products such as Al₃Ti, Al₂O₃, and TiBO₃, and titanium sub oxides as listed in Table 1 and observed in Figure 10. As the temperature increases and the reactions proceed, intermediate phases disappear and TiB₂ and Al₂O₃ are the ultimate products.

The reduction of titanium dioxide to titanium diboride in molten aluminum in the presence of boron may be described by a number of well-defined reaction steps as proposed below:

Stage I: Melting of Al, dissolution of B, and Phase change of TiO₂ from Anatase to Rutile

Figure 10a and Figure 10b represent the X-ray diffraction spectrum of the unheated mixture and the mixture heated to 760 °C. No significant compositional changes are observed. The DSC curve of the mixture also shows that up to 760 °C no irreversible transition occurred and it can be concluded that the endothermic peak is only caused by the heat absorption due to aluminum melting (Reaction 3-6) and no other reaction is taking place at this range.



Reaction 3-6

The X-ray diffraction pattern obtained from the samples held isothermally for longer periods of time at 760 °C (Figure 10c) show that the anatase TiO₂ used to prepare the

mixtures begins to transform to rutile- TiO_2 as described by reaction (3); however, some anatase remains in the specimen even after a 30 minute hold time.

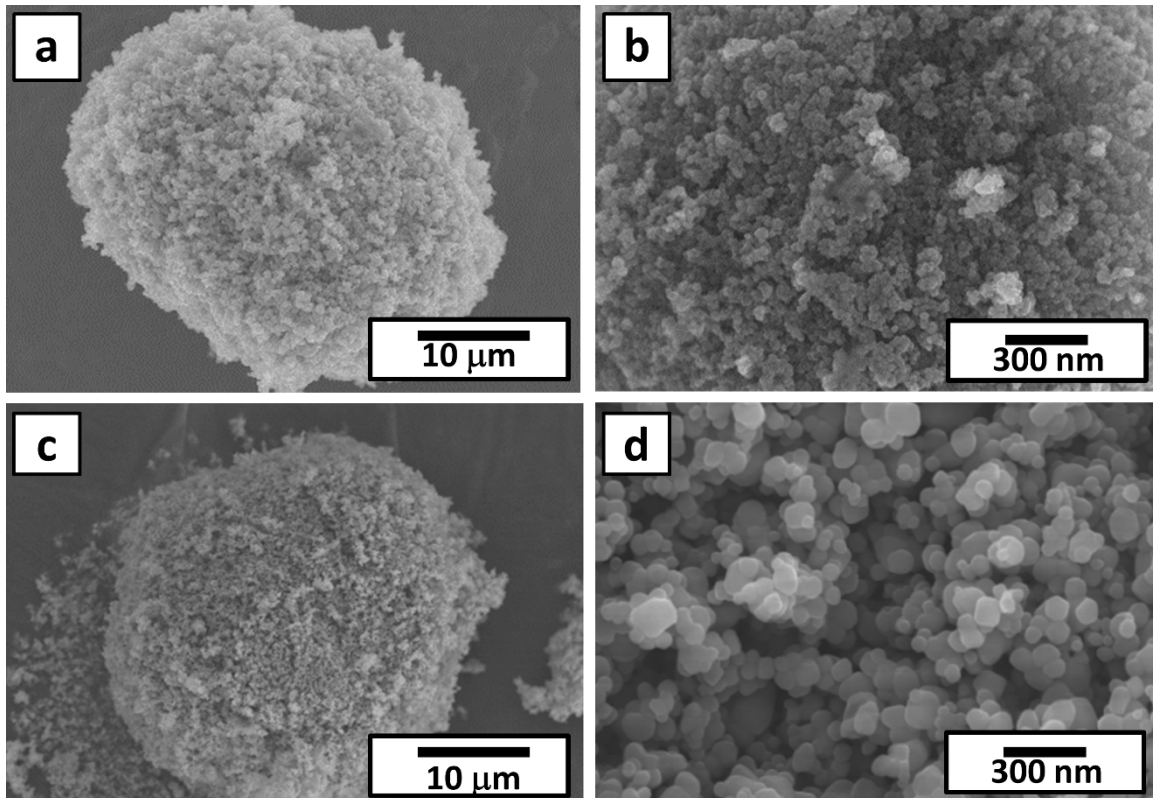
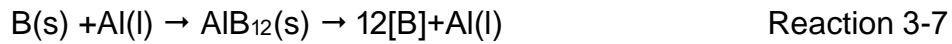


Figure 11 The Secondary Electron Images of (a) and (b) TiO_2 anatase particle, and (c and (d) TiO_2 rutile particle.

The Anatase–rutile phase transition is expected to occur within the temperature range of 400 – 1200 °C [139]. Figure 11 shows the TiO_2 rutile surface morphology of micron size powders. The Rutile surface is highly hierarchical with clusters of fine nano-sized crystals which are aggregated in a spheroidal morphology and have a smooth surface texture. In the presence of liquid aluminum, the boron powder is expected to dissolve forming an Al- B solution. However, It has been reported that boron powders initially combine directly with liquid aluminum to form AlB_{12} and then AlB_{12} decompose to produce active [B] according to Reaction 3-7. While this

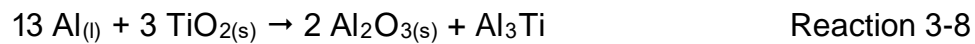
intermediate reaction was not directly observed in this study, it has been observed experimentally by others [39] [48].



Stage II: Attack of Al and B on TiO₂

At 900 °C (Figure 10d), intermediate phases including TiBO₃, Ti₂O₃, and minor quantities of Al₂O₃, and Al₃Ti have begun to appear.

The presence of minor amounts of Al₂O₃ and Al₃Ti in the heat treated mixture suggests partial occurrence of Reaction 3-8.



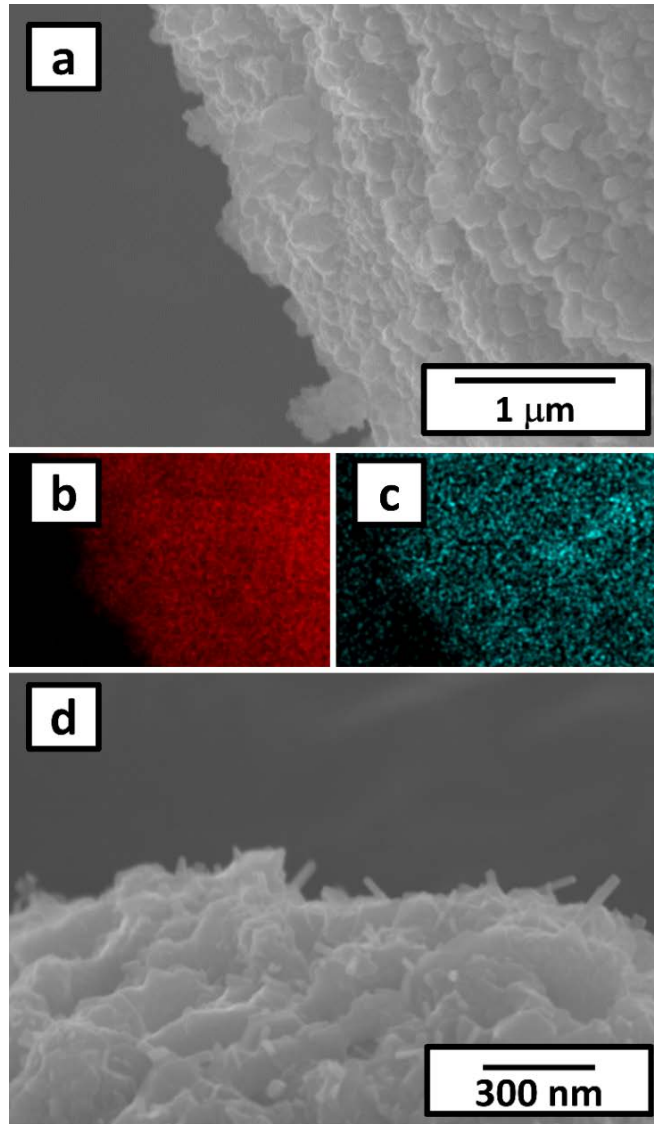


Figure 12 TiO₂ surface obtained from heat treatment at 900 °C with no dwell time (a) and (d) the secondary electron images and (b) aluminum elemental map (c) Oxygen elemental map.

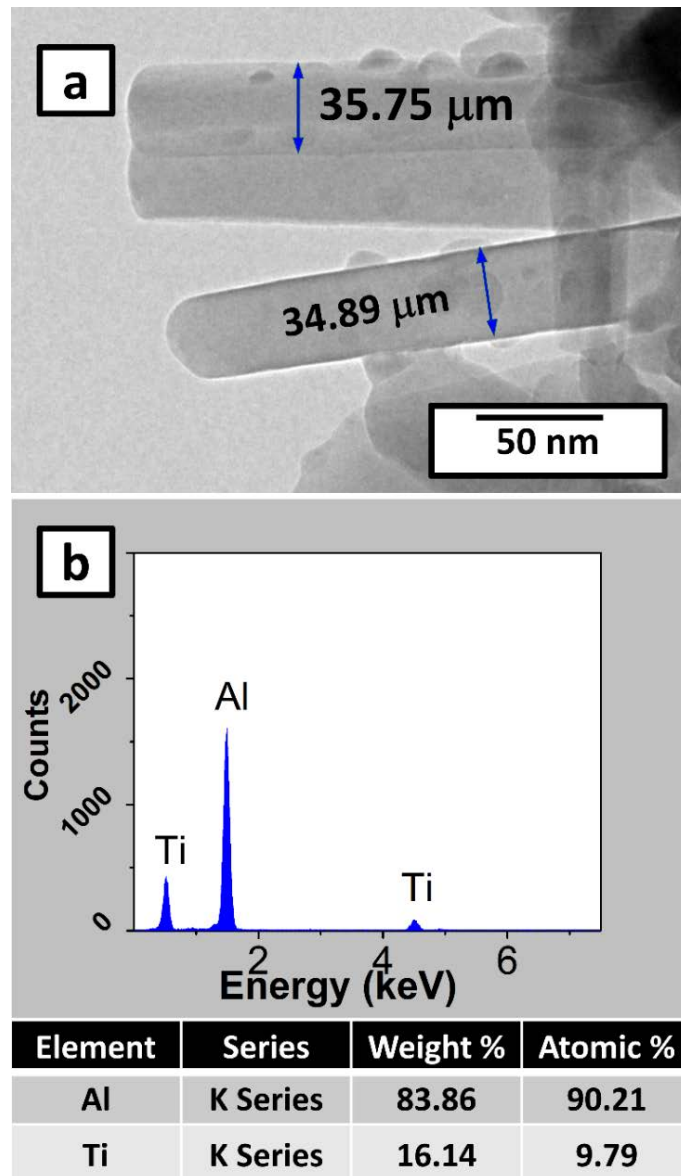


Figure 13 (a) Transmission electron microscopy image and (b) Energy Dispersive spectrum of the nanowire structure on TiO_2 surface obtained from heat treatment at $900\text{ }^\circ\text{C}$ with no dwell time.

Al_2O_3 is the most stable product in the Al- TiO_2 -B system both thermodynamically (free energy consideration) and kinetically (Higher activity of Al compared to B in Al-B-Ti liquid system). Therefore, initially it is expected that the TiO_2 surface is attacked by aluminum to form Al_2O_3 and Al_3Ti through a displacement reaction. The rough TiO_2 rutile surface (Figure 11) consists of a number of grains that result in a very high surface area that results in fast reaction kinetics. SEM and TEM observations and elemental analysis confirm the formation of a shell on TiO_2 particles at this stage (Figure 12 and

Figure 13). Surface features (Figure 12d) show coexistence of a spheroidal and rod-like structure of several tens of nanometers. Energy dispersive analysis (Figure 13b) shows that the rod-like phase corresponds to Al_3Ti and the nodular phase corresponds to the Al_2O_3 phase. During formation of this hybrid structure on the TiO_2 surface, initially, TiO_2 reacts with Al to form Al_2O_3 , rejecting Ti into the surrounding liquid. As a result, the region between the newly formed Alumina nodules becomes highly enriched with [Ti]. Because of the high Ti concentration in the local liquid that surrounds the alumina nodules, the concentration of Ti reaches the point where it can react with aluminum to form Al_3Ti . Thus the Al_3Ti phase nucleates on the surface of the TiO_2 particles in regions not covered by the Al_2O_3 nodules.

Once the Al_2O_3 layer that forms is continuous, it prevents the liquid aluminum from coming into contact with the TiO_2 underneath. However B, which diffuses interstitially, can react with the TiO_2 underneath the Al_2O_3 shell since B diffusivity is higher in Al_2O_3 than diffusivity of aluminum in Al_2O_3 . The borothermic reduction reaction therefore proceeds in an intermediate layer between TiO_2 and Al_2O_3 through solid diffusion. In borothermic reduction of TiO_2 , it is expected that initially boron reduces the TiO_2 to titanium borate (TiBO_3) and then excess boron will reduce TiBO_3 to TiB_2 [34]. The presence of TiBO_3 , the predominant titanium boron phase at this temperature, clearly indicates that the initial step of borothermic reduction has started on the TiO_2 surface. TiO_2 reacts with B to form TiBO_3 and Ti_2O_3 as intermediates through a partial reduction according to Reaction 3-9.



However, the XRD peak position at 48.77° corresponds to $(\text{Ti}_{0.99}\text{Al}_{0.01})_2\text{O}_3$ phase.

The slightly shifted 2θ position of Ti_2O_3 characteristic peaks, indicates the progressive

substitution of Ti by Al. This implies that Ti_2O_3 which forms at this stage is simultaneously attacked by the aluminum diffusing into the solid shell.

This assumption is confirmed by SEM observations carried out on samples obtained on the powders which were lightly ground using a mortar and pestle. These various layers discussed so far are apparent in Figure 14 in the SEM micrograph in which the TiO_2 core, the borothermic reduction products and the Al_2O_3 / Al_3Ti shell can be observed.

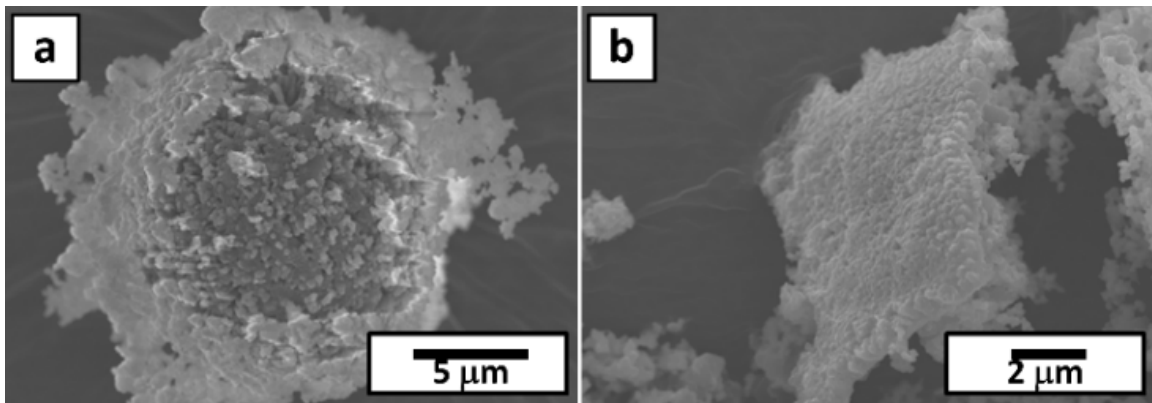
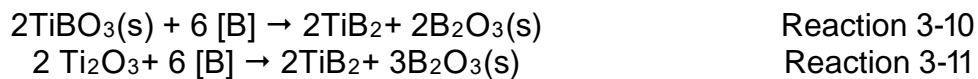


Figure 14 The secondary electron image obtained from the powders retrieved from 900 °C heat treatment and were lightly grounded using a mortar and pestle.

Stage III: Creation of TiB_2 and B_2O_3 by attack of B on $TiBO_3$ and Ti_2O_3

Figure 10(e), X-ray diffraction pattern of the mixture isothermally treated for 5 minutes at 900 °C, suggests that the borothermic reduction proceeds and the two phases formed by reaction (6) ($TiBO_3$ and Ti_2O_3) are reacting with boron to form TiB_2 and B_2O_3 (Reaction 3-10 and Reaction 3-11).



This suggests that the third stage of the phase evolution is governed by a progressive borothermal reduction of TiO_2 and $TiBO_3$ in the presence of residual

boron. Detection of B_2O_3 is complicated using both by XRD and EDS in this system. The low atomic number of B_2O_3 relative to other species leads to a low or no signal in EDS. The major diffraction peaks of the B_2O_3 phase which is near 32° , 40° , and 43° 2θ position are very close to the major peaks of other species, thereby making detection difficult. However, Figure 15, which is an enlargement of a high resolution X-ray diffraction spectra of selected ranges, shows the characteristic peaks of B_2O_3 in more detail.

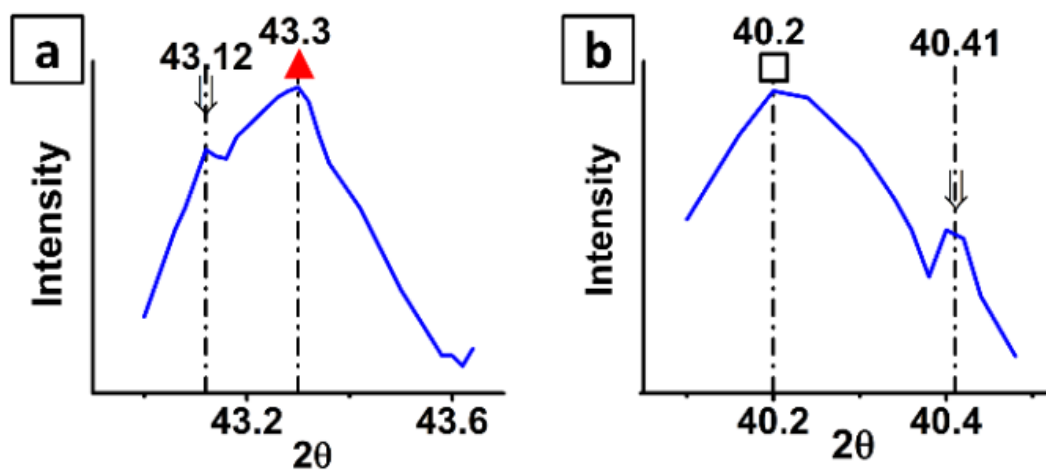
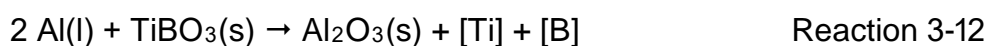


Figure 15 High resolution XRD spectra showing B_2O_3 characteristic peaks at a) 43.12° b) 40.41° indexed with the 06-0634 JCPDS.

In the present system there are two possible routes toward the consumption of $TiBO_3$. $TiBO_3$ can be attacked both by boron or aluminum. The Gibbs free energy data of $TiBO_3$ appears to be unknown and so no accurate quantitative thermodynamic predictions can be made. However, based on our XRD results, Al_2O_3 and Al_3Ti content does not show a significant change compared to stage II while $TiBO_3$ and Ti_2O_3 is decreasing to a considerable extent. This appears to rule out the potential reduction of $TiBO_3$ by aluminum through Reaction 3-12.



Although partial reduction of TiO_2 by aluminum was started at Stage II, the XRD analysis shows that the formation of the TiB_2 is associated with a decrease in the intensity of the main TiBO_3 and Ti_2O_3 peaks but little change to the Al_2O_3 and Al_3Ti peaks. This means that further aluminothermic reduction was not extensive at this stage. As stated previously, this can be attributed to the difference in diffusion rate of [B] and [Al] in the thin Al_2O_3 solid shell which formed on TiO_2 surface. Longer reaction times show increased production of TiB_2 through reactions (7) and (8), which also result in large volume changes. Initially, when the thin shell of Al_2O_3 forms on the surface of TiO_2 particles (At 900C- 0 Min), the 58% change in volume due to reaction 3 can be compensated by its free surface movement into the molten metal. When boron diffuses into the Al_2O_3 shell, various reactions will take place. Initially formation of TiBO_3 and Ti_2O_3 cause a 56% volume change. However, further borothermic reduction of TiO_2 causes a 156% change. While this can occur by an internal reaction underneath the Al_2O_3 / Al_3Ti shell, the large difference in densities between reactants and products makes it likely that cracking will occur in the shell, thereby allowing direct contact between the melt and TiO_2 which will act to increase the reaction rate. This causes the onset of Stage IV in which molten aluminum directly reacts with TiO_2 to form Al_2O_3 .

Figure 16 shows the backscattered and secondary electron image of the cracked surface of the film encapsulated the TiO_2 particles. The inner surface exposed due to fracture of the shell, which seems darker in backscattered image, is TiO_2 , which is also confirmed by X-ray analysis. The lighter features are likely to be TiBO_3 and Al_2O_3 . Al_3Ti nano rods sitting on a shell of alumina spheroidal features are also detectable in this image. Figure 17a shows the overgrown feather-like product of the borothermic

reduction. In Figure 17b which shows the PDBSE image of the surface, the low mass phase, here TiB_2 , can be observed.

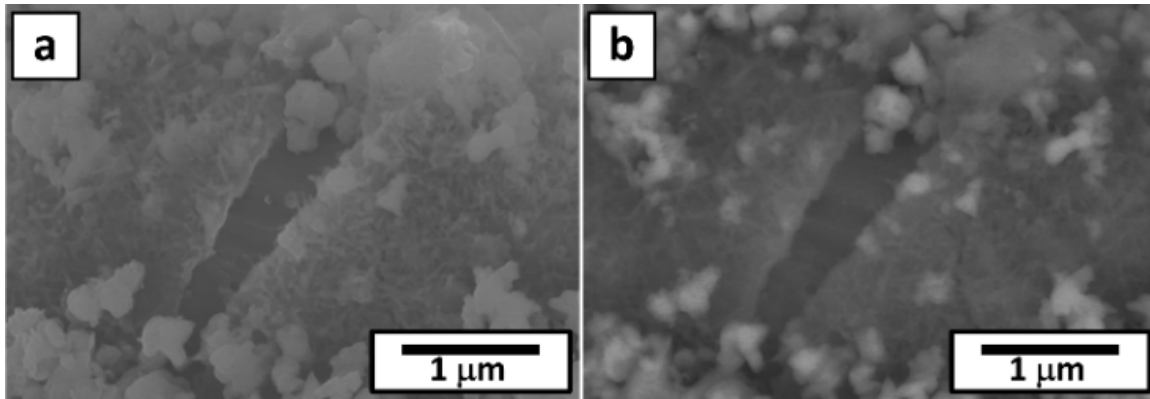


Figure 16 (a) Secondary electron image and (b) Backscattered electron (BSE) image of crack on Al_2O_3/Al_3Ti shell obtained from the powders retrieved from $900\text{ }^\circ C$ for 5 minute heat treatment

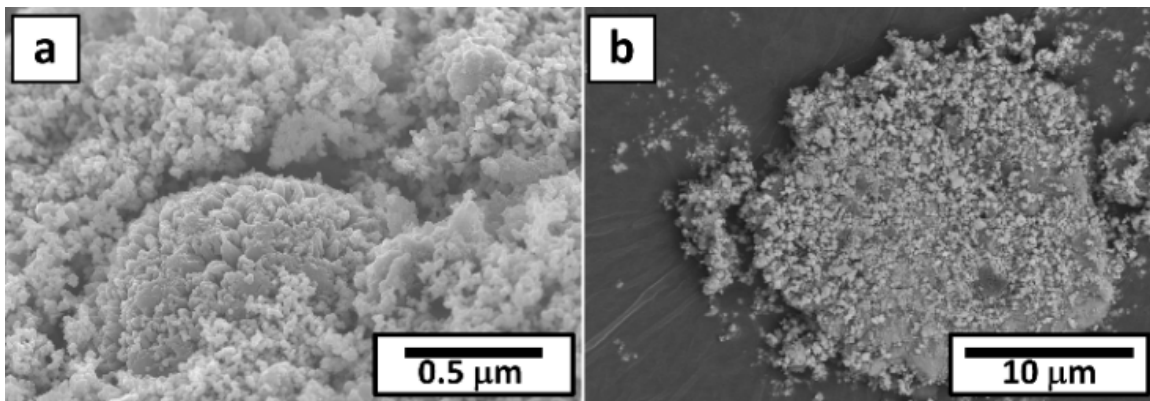


Figure 17 (a) Secondary electron image of TiB_2 overgrown nodule on TiO_2 surface (b) Backscattered electron (BSE) image obtained from the powders retrieved from $900\text{ }^\circ C$ after 5 minute heat treatment.

Stage IV: Attack of remaining TiO_2 and B_2O_3 by aluminum - formation of titanium suboxides

When [B] is depleted in the melt, aluminothermic reduction of the remaining TiO_2 proceeds by formation of Magne´li phases. This stage of the reduction of titanium dioxide is characterized by the formation of a mixture that mainly consists of the various types of titanium suboxides, Ti_nO_{2n-1} (Ti_3O_5 , Ti_2O_3 , and Ti_4O_7). In the last

stages of conversion from TiO_2 to Al_2O_3 , Ti oxides must increase in Ti:O ratio due to reduction by aluminum (Reaction 3-13 to Reaction 3-15).

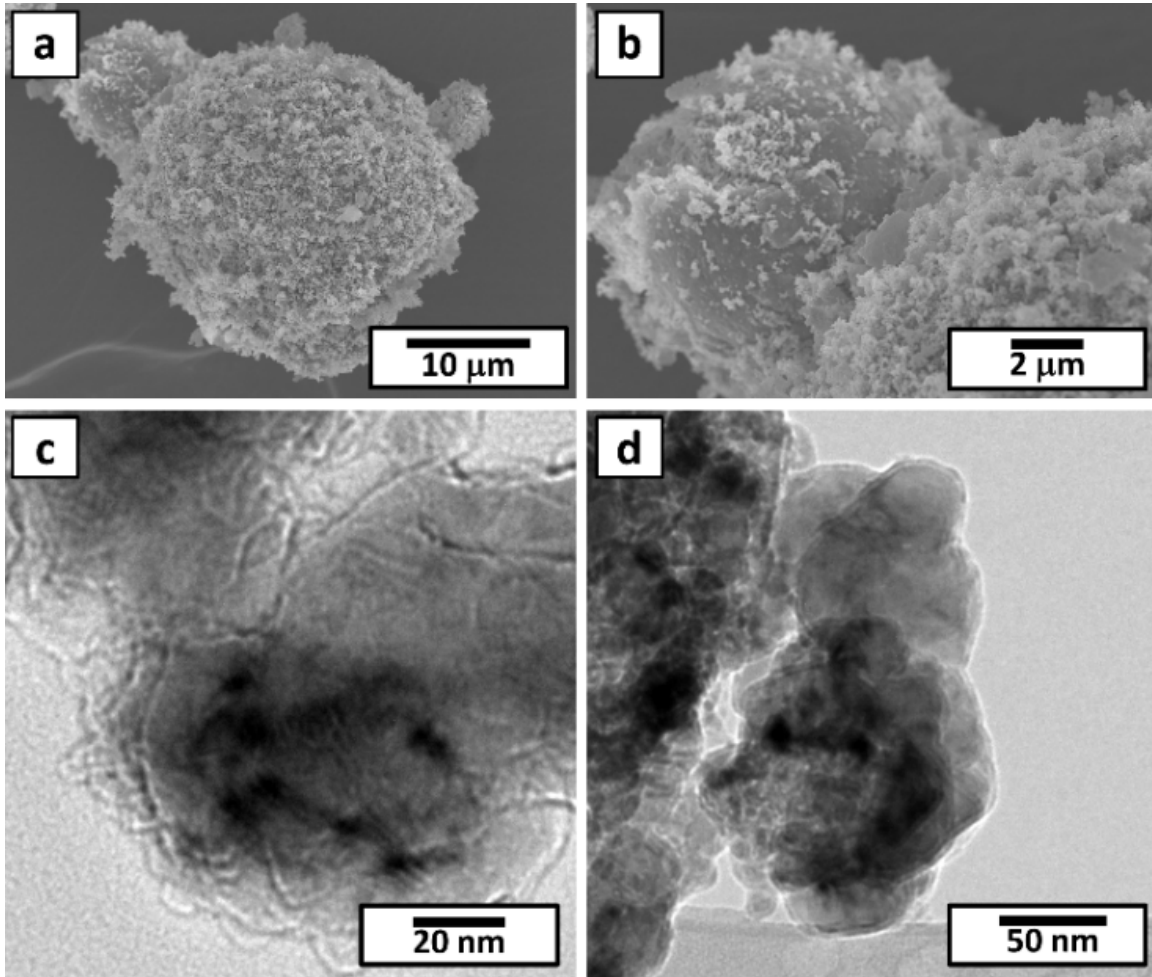
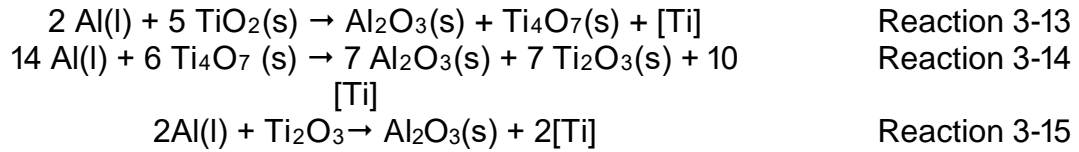


Figure 18 (a) and (b) The secondary electron image (c) and (d) Bright Field Transmission electron microscopy image of particles obtained from the powders retrieved from 900 °C after 10 minute heat treatment.

Cracks and voids initiated from the external surface of the Al_2O_3 and TiBO_3 layers and propagated through the shell, facilitate the aluminothermic conversion of TiO_2 to Al_2O_3 by increasing the number of sites for reaction. In Ti-O system, Ti_2O_3 is the most stable product of the TiO_2 reduction. However, the reduction of TiO_2 by aluminum during this stage proceeds through the formation of intermediate compounds. Several

intermediate suboxides are formed including Ti_4O_7 , Ti_3O_5 before finally forming Ti_2O_3 . The peak positions for these phases are at 40.22° and 48.77° shifts to 40.19° and 48.70° , respectively. This shows that the mixed aluminum titanium oxide which had been formed at Stage II is no longer stable and Ti_2O_3 is the stable phase of this stage. These reactions continue until all of the remaining TiO_2 is consumed. The stability of Ti_2O_3 can be explained by its corundum structure. Therefore, Reaction 3-15 will not proceed to completion and some equilibrium Ti_2O_3 may remain in the system. Reduction to TiO was not observed, an effect which can be explained by the relatively low thermodynamic stability of this phase. The sudden increase of Al_2O_3 can be explained by Reaction 3-13 to Reaction 3-16 at this stage.

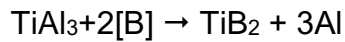


Gradual decrease in the $TiBO_3 / TiB_2$ XRD intensity ratio also suggests that borate and oxide continues to react with boron through reactions 8 and 9 and forming more TiB_2 . Figure 18 shows a secondary electron image showing how these overgrown nodules of TiB_2 continue to grow. It can be expected that when these nodules grow and reach a certain size, they break off of the surface. Figure 18 shows a TEM image of these nodules at this stage. The B_2O_3 phase is also reduced by liquid aluminum, leading to the rejection of active [B] into the melt.

Stage V: Complete exhaustion of intermediates, dissolution of Al_3Ti , and precipitation of TiB_2

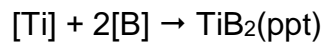
The X-ray diffractogram of the reaction products heat treated at $1200^\circ C$ indicates that TiB_2 and Al_2O_3 are the major phases remaining. In presence of excess boron, as

a result of Reaction 3-17, remaining Al_3Ti transforms to TiB_2 , which is a more thermodynamically stable intermetallic.



Reaction 3-17

The active B diffused to the surfaces of remaining Al_3Ti and reacted with Al_3Ti to form TiB_2 starting at stage II, reduce all the Al_3Ti at this stage. Therefore, Reaction 3-17 goes to completion and the Al_3Ti rods are reduced entirely. Any remaining [Ti] and [B] dissolved in aluminum will also precipitate to form TiB_2 by Reaction 3-18.



Reaction 3-18

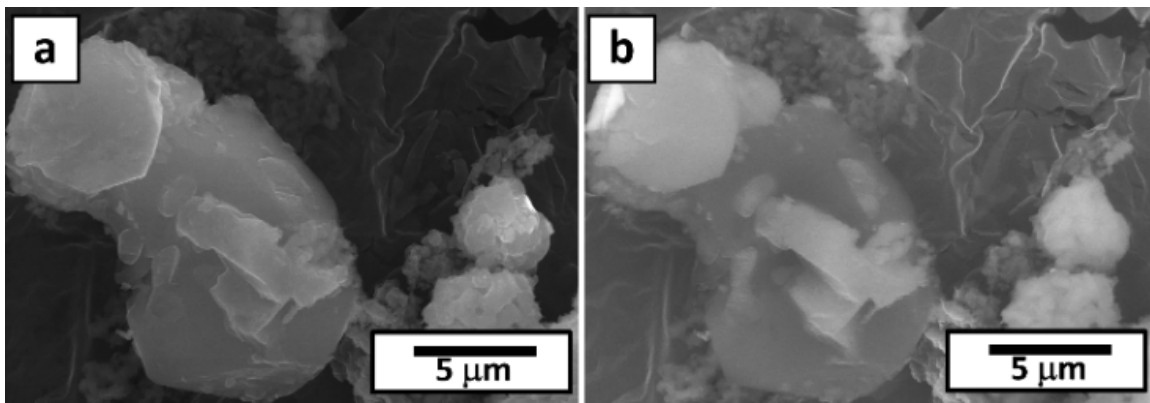


Figure 19 (a) Secondary electron image and (a) Backscattered electron (BSE) image of different phases obtained from the powders retrieved from 1200 °C heat treatment.

No Al_3Ti is observed in the final products. The complete reduction of TiO_2 and dissolution of Al_3Ti allows only Al_2O_3 and TiB_2 to exist as final reaction products. Figure 19 shows the secondary and BSE image and Figure 20 shows the elemental map of the mixture of micron size TiO_2 , aluminum, and boron heated to 1200 °C until reaction complete. The X-ray maps show that the resultant particulates mainly contained Al and O or Ti and B suggesting Al_2O_3 and TiB_2 .

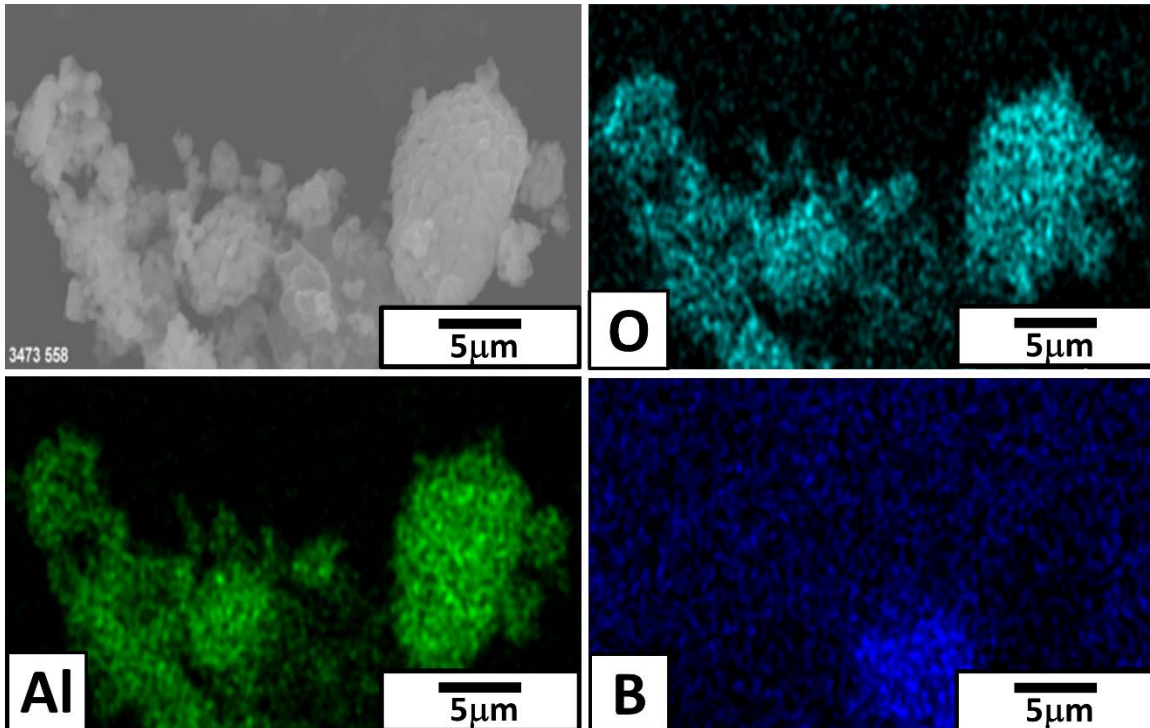


Figure 20 Secondary electron image and the elemental map (Oxygen, Boron, and Titanium) of the mixture of micron size TiO_2 , aluminum, and boron heated up to 1200 °C

The reactions thought to be involved in creating this conversion are shown schematically in Figure 21. Based on this five stage reaction model it is possible to speculate on how to decrease the size of particles that form. The proposed reaction model suggests that the size of particles ultimately formed by the reduction process is likely related to the reaction sites on the TiO_2 surface. These observations suggest that using nanosized TiO_2 powder as precursor is a viable process capable of resulting in the synthesis of nano Al_2O_3 and TiB_2 as reinforcement particles inside an aluminum matrix.

To confirm the above hypothesis, the same mixture using a nano size TiO_2 precursor was studied. Figure 22 shows the TEM image of the particles obtained where nano-sized TiO_2 powder was used. The Al_2O_3 and TiB_2 particles obtained here are greatly reduced in size in comparison to Figure 20 where TiO_2 particles were in range of 10-50 microns.

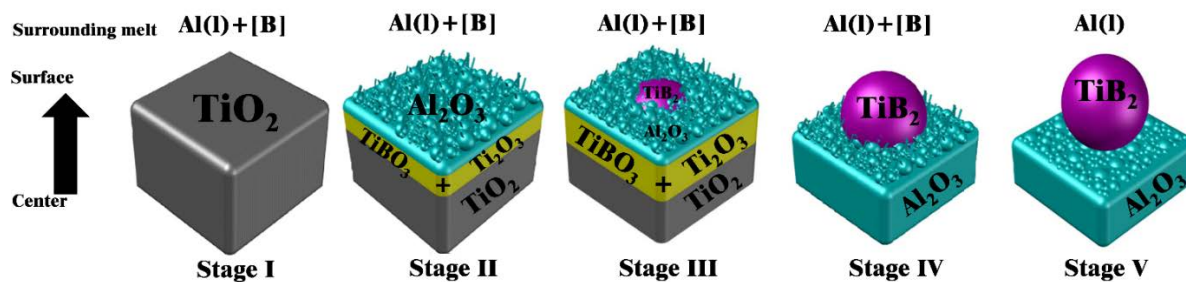


Figure 21 Schematic representation of the proposed five stage model conversion of TiO_2 to TiB_2 and Al_2O_3 in liquid aluminum; Stage I- Melting of Al, dissolution of B, and Phase change of TiO_2 from Anatase to Rutile, Stage II- Attack of Al and B on TiO_2 and formation of Al_2O_3 shell on TiO_2 surface, Stage III, Creation of TiB_2 by attack of B on TiBO_3 and Ti_2O_3 Stage IV- Aluminothermic reduction of remaining TiO_2 and formation of titanium suboxides, and stage V- Complete exhaustion of intermediates, dissolution of Al_3Ti , and precipitation of TiB_2

The X-ray diffraction analysis of products formed using fine TiO_2 revealed the same main phases of the coarse products— Al_2O_3 and TiB_2 . However, it was observed that, when finer TiO_2 was used as starting material, the complete conversion takes place at lower temperatures. This may be attributed to the fact that smaller particles of TiO_2 powder promotes the reactions between Al and TiO_2 by increasing reaction sites.

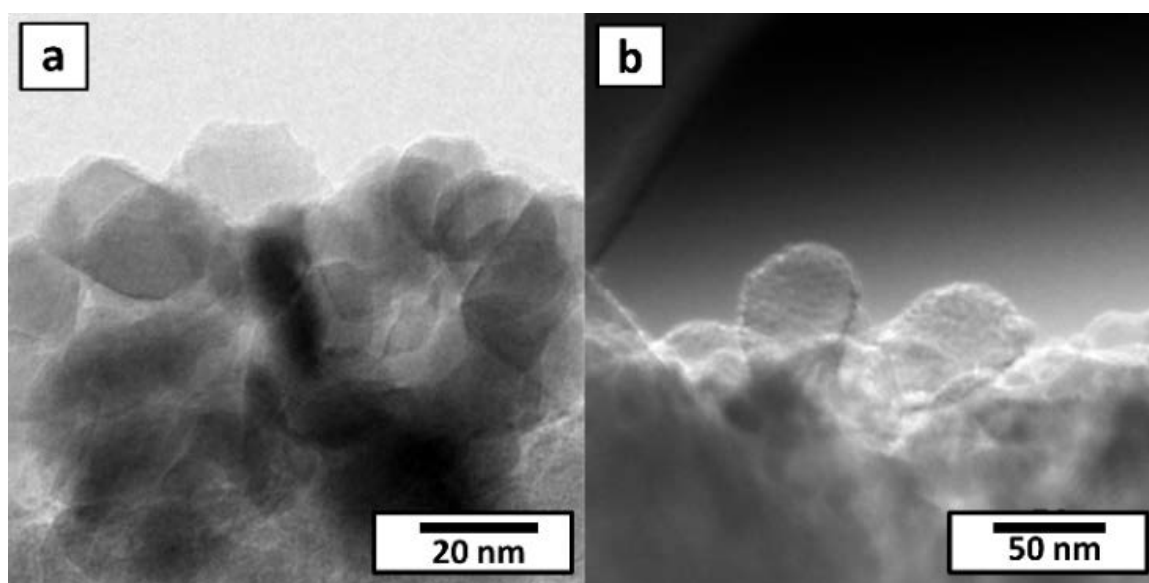


Figure 22 (a) Bright Field (b) Dark Field Transmission electron microscopy image of the particles obtained from the heat treatment of the mixture of nano size TiO_2 , aluminum, and boron heated up to $1200\text{ }^\circ\text{C}$.

Figure 23 and Figure 24 show the HRTEM images of the product of the mixture of nano sized TiO_2 , aluminum, and boron mixture after heated up to $1200\text{ }^\circ\text{C}$. The lattice fringes are clearly observed in the HRTEM image, which can be matched with Alumina

and TiB₂ particles. The particle size varies in two ranges, 5-25 nm and 40-55 nm, which after matching with lattice parameters, belong to Al₂O₃ and TiB₂, respectively. The d-spacing of 0.174 nm (Figure 23) corresponds to the lattice fringe of {024} of Alumina. The d-spacing of 0.262 illustrated in Figure 24, corresponds to the {100} and {003} fringe of TiB₂. These results are in good agreement with the proposed reaction model which correlate the reaction site size to the final reinforcing intermetallics.

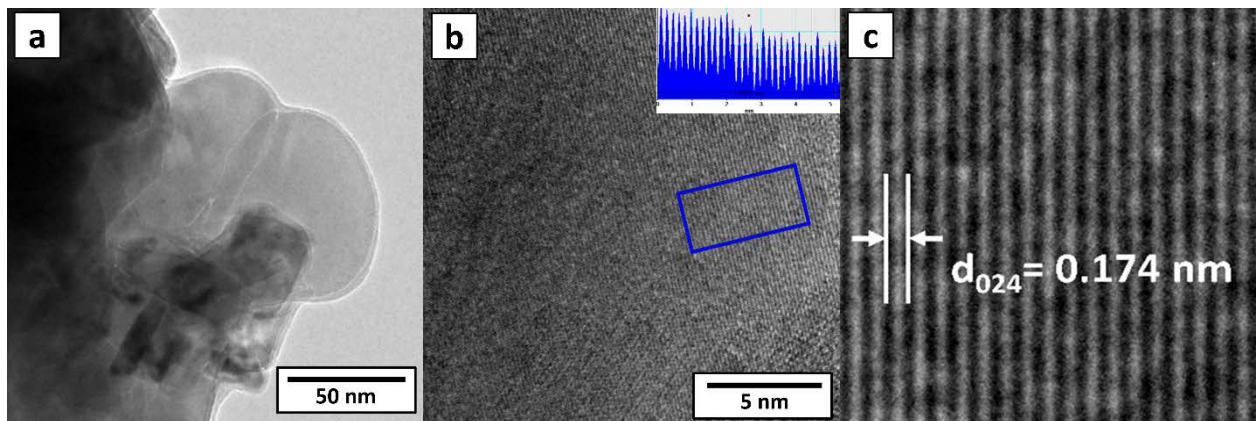


Figure 23 (a) Bright Field Transmission electron microscopy image and (b) and (c) HRTEM images the particles obtained from the heat treatment of the mixture of nano size TiO₂-Al-B heated up to 1200 °C indexed by Al₂O₃ 75-1862 JCPDS card .

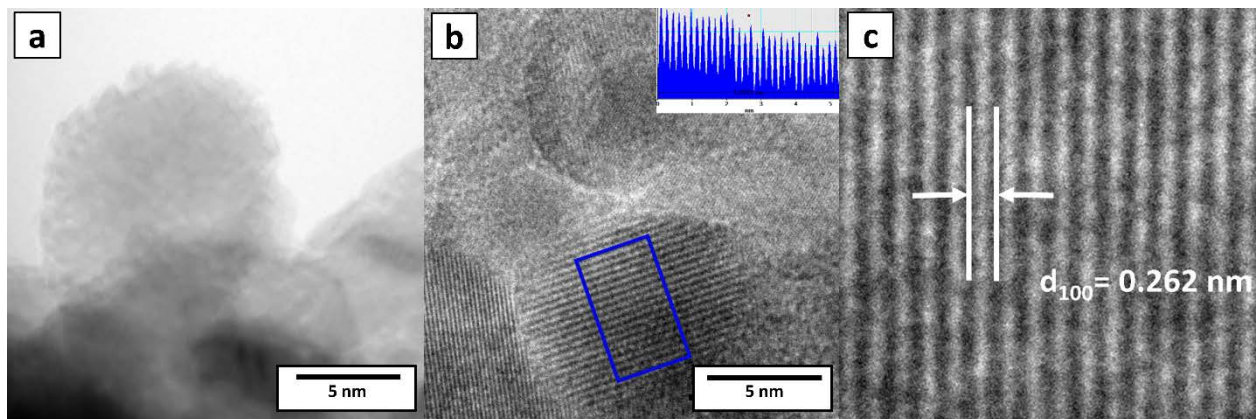


Figure 24 (a) Bright Field Transmission electron microscopy image and (b) and (c) HRTEM images the particles obtained from the heat treatment of the mixture of nano size TiO₂-Al-B heated up to 1200 °C indexed by TiB₂ 35-741JCPDS card .

3.4 Summary

The reduction of TiO₂ by molten aluminum in the presence of amorphous boron has been investigated and shown to be a multi-stage process. Initially a solid shell of Al₂O₃ / Al₃Ti forms on the surface of the TiO₂ particles. This is followed by borothermic

reduction of the TiO_2 by the diffusion of elemental B through the $\text{Al}_2\text{O}_3 / \text{Al}_3\text{Ti}$ shell, thus forming TiBO_3 and Ti_2O_3 at the shell/ TiO_2 interface. Further borothermic reduction leads to a significant volume change that eventually causes the Al_2O_3 shell to crack, allowing aluminum to make contact with the intermediate layers and fresh unreacted TiO_2 . When the melt is depleted of boron, the aluminum starts to reduce the remaining TiO_2 to form Al_2O_3 . The cracks in the outside shell facilitate aluminothermic reduction of the TiO_2 core. Finally, TiB_2 and Al_2O_3 particles form as a result of gradual TiO_2 exhaustion. According to the reaction sequence discussed and observed microstructural outcomes, TiB_2 and Al_2O_3 reinforcement particles may be formed in Al-B melts through the reaction of TiO_2 particles, where the size of the in-situ formed particles may be controlled by the size of the TiO_2 particles. In view of the findings it was theoretically predicted and experimentally demonstrated that TiB_2 and Al_2O_3 particles with sizes ranging from 5-55 nm can be formed in-situ from nanosized TiO_2 (<25 nm) precursors, while TiB_2 and Al_2O_3 particles with sizes ranging from 20-45 μm can be formed in-situ from microsized TiO_2 particles (>44 μm) .

CHAPTER 4. PROCESSING/STRUCTURE RELATIONSHIPS

4.1 Introduction

Researchers have explored in-situ reinforcement fabrication methods using various techniques such as mixed salt reaction, liquid mixing and XD technique, but little results have been published on in-situ fabrication of nanocomposites in aluminum based alloys using casting, which is the most cost effective and scalable manufacturing technique in fabricating metal matrix composites.

It has been discussed in chapter 3 that the interaction between TiO_2 and boron or aluminum is governed by surface reaction. Therefore, to control the size of in-situ formed intermetallics, the reaction site can be considered as a controlling parameter. Additionally, it is theoretically proven that ultrasonic based mixing helps deagglomeration of small particles and enhance precipitation and nucleation of second phase in the molten metal. Combined with the in-situ processing, it can be considered an approach to synthesize nanoparticles dispersed in the matrix.

The objective of the following chapter is to examine the microstructure and mechanical properties of composites synthesized by a combination of ultrasonic processing with aluminoborothermic reduction of titanium oxide in presence of boron in molten aluminum. After the addition of the powder mixture to the molten metal by mechanical stirring combined with ultrasonic cavitation, the aluminum and boron reacts with the TiO_2 through Reaction 3-5.

4.2 Materials and Experimental

4.2.1 Materials

Acros Organics™ Titanium(IV), 98+% anatase powders with an average particle diameter of 25 μm (>44 μm) and Sigma- Aldrich Titanium(IV) oxide, anatase

nanopowders with particle diameter <25 nm, boron powder, 94-96% amorphous, with an average particle diameter of <5 micron, and Aluminium,99%,powder, 200 mesh, were used in the preparation of precursors of various samples. Commercially pure aluminum was used in ingot form.

4.2.2 Composite fabrication

In this work, conventional stir mixing and ultrasonic assisted reactive stir mixing is used to synthesize Al/ (Al₂O₃ - TiB₂) hybrid composites. Aluminum ingot were placed in a coated graphite crucible (ID 89 mm, Depth 127 mm) and heated using an electrical furnace and held at various temperatures (700, 850, and 1000 °C). A Zircwash coating was applied inside the crucible to avoid contamination. Since the melt is so reactive with silicon present in the clay graphite crucible, it is necessary to make sure that enough Zr coating covers both the impeller and the crucible. In the initial trials, the SEM and EDS image shows the presence of considerable amount of Si in the composite. The EDS / Line scan of the casted composite in the clay crucible without enough coating is shown in Figure 25.

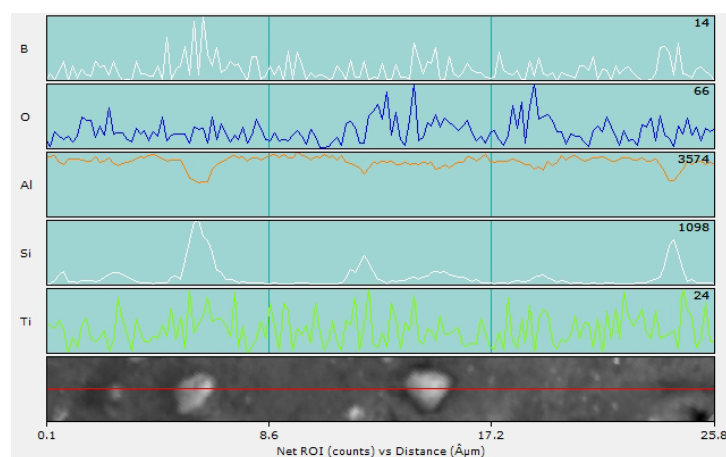


Figure 25 Line scan X-Ray spectroscopy of the Al/ Al₂O₃-TiB₂ composite casted in the uncoated clay crucible

Once the melt reached the desired constant temperature, the measured quantities of TiO₂ nanoparticles and boron were mixed using a Resodyne acoustic mixer set to 70% power for 7 minutes.

Since using TiO₂ and boron in powder form to synthesis TiB₂ by in melt reaction has not been done in previous literature, in order to identify the proper technique to add the mix to the melt, several trial and error experiments were performed. Different ways of addition of powders to molten aluminum were tried, and parameters which influence the reaction were identified. Both use of powders or loose packets of powders were not satisfactory in the synthesis process and mostly the powders sink or float to the surface and bottom of the crucible during addition and mixing of powders.

As an alternative way, the mixed powders were mixed with pure aluminum powder in 42:58 ratio and pressed into pellets using a 25 mm ID trapezoidal split sleeve pressing die set at a pressure of 2000 psi to form cylindrical pellets (Figure 26). The Al/ (Al₂O₃ -TiB₂) hybrid composite containing the TiB₂ and Al₂O₃ was synthesized by adjusting the compositional ratio of TiO₂, B, and Al. The pellets containing reactant particles mixture were preheated in a resistance furnace at 200 °C for 60 minutes. These pellets were used to introduce the reactants to the melt.



Figure 26 The mixed powders pressed into pellets using formed cylindrical pellets

The melt was stirred for various lengths of time (5, 10, and 15 minutes) using a boron nitride coated steel MixedFLOW Impeller (45° pitched blade, Fawcett Co.) rotating at a

speed of approximately 500 rpm, while the pellets of reactants and wetting agent were dipped into the melt at a rate of 2 g/min. The impeller was placed dynamically in the center of the melt and its position was changed manually to push the pellets inside the melt. For a series of samples, a high-energy ultrasonic horn with a diameter of 20 mm and a frequency of 20 kHz was simultaneously placed just above the composite slurry to avoid melt temperature drop. Then, the surface oxides were skimmed thoroughly prior to pouring the molten composite into the mold, and the composite was squeeze cast into a mold. An electric resistance furnace was used to preheat the rectangular squeeze casting mold to approximately 330 °C. Once the mold reached the preheat temperature it was removed from the furnace and placed in a hydraulic press. After the melt is poured into the mold cavity, the punch is dropped into the cavity and a pressure of approximately 5000 psi is applied to the punch to squeeze cast the composite ingot. The experimental set up is shown in Figure 27.

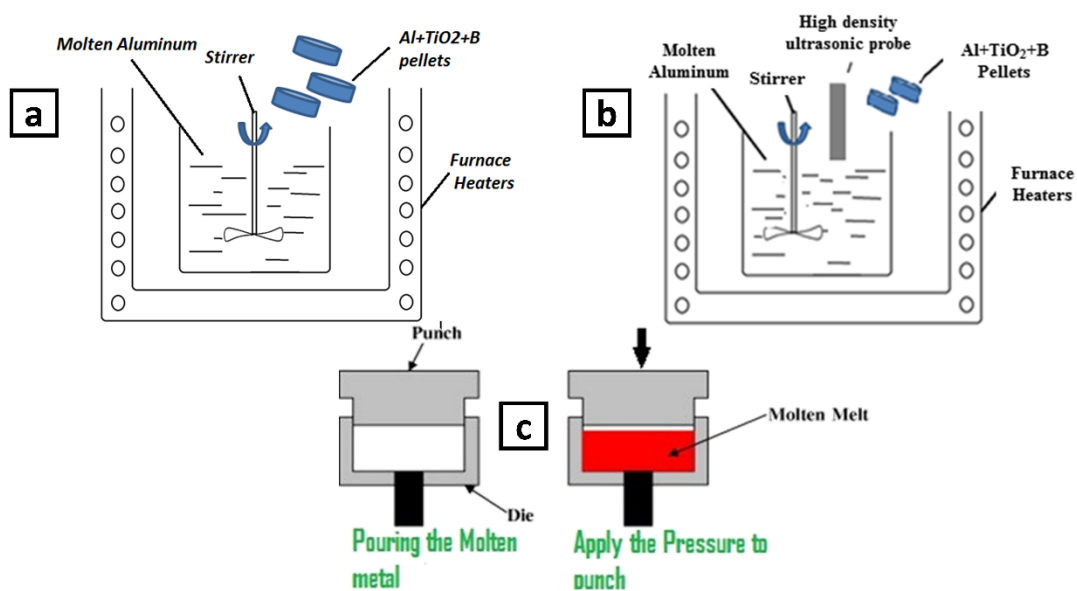


Figure 27 The experimental set up for a) in-situ reactive stir mixing process b) Ultrasonic assisted in-situ reactive stir mixing process c) Squeeze Casting

Several factors can influence the final properties during in-situ processing of Al/(Al₂O₃-TiB₂) composites include particle loading, melt temperature, mixing time, and mixing technique. Any change in these parameters can results is change in particle size and distribution, α - aluminum grain size, final mechanical properties including tensile, and wear properties. In this study, selected number of processing factors were designated to evaluate the optimal processing conditions for Al/(Al₂O₃-TiB₂) reinforced composites.

To study the effect of processing variables, a coded level were allocated to the numeric factors for liquid mixing route as shown in Table 2. Four parameters were selected while three of them (P1-3) were studied in interaction mode and the mixing technique were studied independently. The experiments designed to study various parameters is listed in Table 3. In total 20 specimen will be obtained through castings. The range each independent factor selected is based upon findings in preliminary results which has been discussed in chapter 3. To study the effect of particle content, another set of samples as shown in Table 2 was prepared. Five level of loading has been studied (0, 0.1, 2, 4, 8 wt.%).

Table 2 Coded levels of liquid mixing independent processing variables

| Code | Parameter Name | 1 | 2 | 3 | 4 | 5 |
|--------------|--------------------------------------|------------|----------|----------|----------|----------|
| P1 | TiO ₂ size | 40 μ m | 25 nm | - | - | - |
| P2 | Reaction temperature ($^{\circ}$ C) | 700 | 850 | 1000 | - | - |
| P3 | Mixing time (min) | 5 | 10 | 15 | - | - |
| P-in1 | Mixing Technique | ST* | ST/US** | - | - | - |
| P-in2 | NPs loading (wt.%) | 0 | 0.1 | 2 | 4 | 8 |

Table 3 Experiment Design- Liquid Mixing

| RUN# | TiO ₂ Size | Reaction temperature | Mixing time | Mixing | NPs Loading |
|------|-----------------------|----------------------|-------------|--------|-------------|
| 1 | - | 1 | - | 2 | 1 |
| 2 | - | 2 | - | 2 | 1 |
| 3 | - | 3 | - | 2 | 1 |
| 4 | 1 | 1 | 1 | 2 | 4 |
| 5 | 1 | 1 | 3 | 2 | 4 |
| 6 | 1 | 3 | 1 | 2 | 4 |
| 7 | 1 | 3 | 3 | 2 | 4 |
| 8 | 2 | 1 | 1 | 2 | 4 |
| 9 | 2 | 1 | 2 | 2 | 4 |
| 10 | 2 | 1 | 3 | 2 | 4 |
| 11 | 2 | 2 | 1 | 2 | 4 |
| 12 | 2 | 2 | 2 | 2 | 4 |
| 13 | 2 | 2 | 3 | 2 | 4 |
| 14 | 2 | 3 | 1 | 2 | 4 |
| 15 | 2 | 3 | 2 | 2 | 4 |
| 16 | 2 | 3 | 3 | 2 | 4 |
| 17 | 2 | 2 | 2 | 1 | 4 |
| 18 | 2 | 2 | 2 | 2 | 2 |
| 19 | 2 | 2 | 2 | 2 | 3 |
| 20 | 2 | 2 | 2 | 2 | 5 |

4.2.3 Characterization of Composites

Specimens were prepared from the castings to study microstructure and mechanical properties. Specimens for microstructural studies and analytical evaluations were cut from the castings as shown in Figure 28 using a low-speed diamond saw.

The specimens were polished using standard metallographic technique. Specimens were hot mounted (about 150 °C) using a mounting press in a non-conductive phenolic resin. Mounted specimens were ground with rotating discs of abrasive paper (silicon carbide paper). The grinding procedure involves several stages, using a finer paper (higher number) each time. Each grinding stage removes the scratches from the

previous coarser paper. This can be easily achieved by orienting the specimen perpendicular to the previous scratches. Between each grade, the specimen was washed thoroughly with soapy water to prevent contamination from coarser grit present on the specimen surface. The sand papers used for grinding samples were 180, 240, 320, 400, 600, 800, and 1200 grit size. Polishing discs were used to achieve final polished surface finish prior to etching. Soft cloth impregnated with 1 and 0.5 μm abrasive colloidal silicon carbide particles were used in this study to produce a smooth surface.

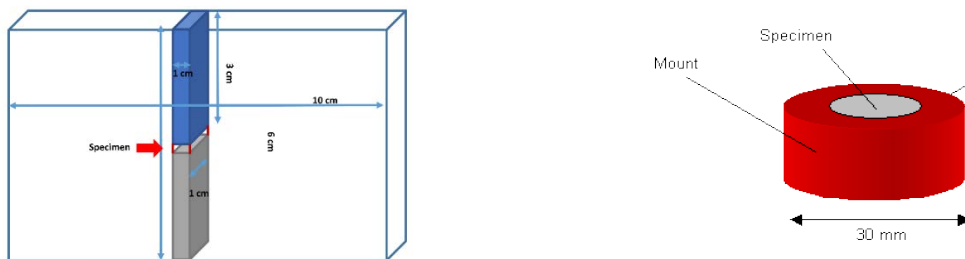


Figure 28 drawing of specimens which have been cut and mounted for microstructural analysis

The specimens were etched using electro etching in a HBF_4 solution (1.8 wt % in H_2O at a constant potential of 22 V for 50 s) to reveal the microstructure of the metal through selective chemical attack. The rate of etching is affected by crystallographic orientation, so contrast is formed between grains, for example in pure metals. The reagent will also preferentially etch high energy sites such as grain boundaries. This results in a surface relief that enables different crystal orientations, grain boundaries, phases and precipitates to be easily distinguished. Samples were finally cleaned in an ultrasonic bath.

Grain size and microstructure were photographed using a polarized light micrographs of optical microscope using a Zeiss Axio Scope. Representative

micrographs of the composites were obtained by a Nikon Eclipse TS100 Optical Microscope coupled with Clemex™ digital acquisition and image analysis system.

HRSEM was carried out on both etched and fracture surface of specimens using a Hitachi S-4800 Ultra High Resolution Cold Cathode Field Emission Scanning Electron Microscope (FE-SEM) at 10 kV. Elemental analysis was performed using Hitachi S-4800 FE-SEM equipped with a Bruker Quantax EDS system. The thin window silicon drift detector (SDD) allows the detection of elements boron and higher.

A FEI™ TEM200 Focused Ion Beam (FIB) with Gallium ion source was employed to obtain TEM thin foils. TEM was done by a Phillips CM-200 operating at 200 kV. Three different areas of the samples were used to calculate the number density of the precipitates in unit volume. STEM characterization was carried out using a FEI/Tecnai™ F30 300 kV TEM equipped with a Fischione™ high angle annular dark field (HAADF) detector and an X-ray Energy Dispersive Spectroscopy (XEDS) detector.

For structural analysis, specimens were examined by X-ray diffraction (XRD) using a Scingtag XDS 2000 diffractometer, with a step size of 2 degrees/min in 20-70 degree range.

The Dynamic light scattering (DLS) method was used to identify sizes and distribution of nanopowders in aqueous suspensions. A suspension of nanoparticles in distilled water were prepared by addition of 5 mM sodium citrate stabilizer using an ultrasonic bath (power 240 W). The sizes of the particles in aqueous suspensions were measured by dynamic light scattering (DLS) on a Brookhaven ZetaPlus PLUS/PALS analyzer (90 plus/BI-MAS). All measurements were for suspensions carried out under isothermal conditions at ambient temperature.

The microhardness was measured using a microhardness tester at 100 g load applied for 15 s. For each sample, average of five reading was reported. Tensile tests of the specimens with and without particles were carried out at ambient temperature by an Instron electronic tensile machine at the strain rate of 10^{-5} mm s⁻¹ according to ASTM E8 using a sub size specimen. Figure 29 shows the tensile test specimens and its drawing. Tensile tests were performed 3 times for each sample and average of three reading was reported. The ultimate tensile strength (UTS) was estimated using a computerized universal testing machine. The fracture surfaces of the failed tensile specimens were observed using SEM.

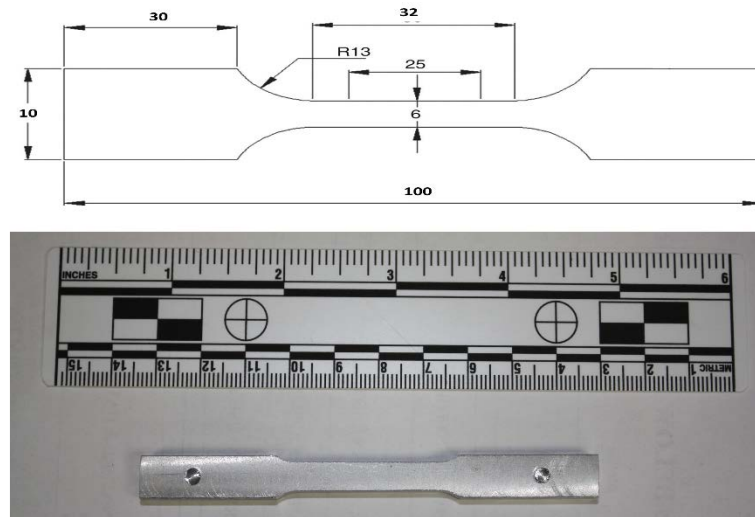


Figure 29 The tensile test specimens and its drawing

Nanoindentation was carried out using CSM NHTX S/N: 55-0019 nanohardness tester with a triangular pyramidal diamond indenter (Berkovich, B-I 93, tip radius=20 μ m) under a constant load of 10 mN. All the measurements and the load and displacement resolutions of the instrument were 1 μ N and 0.03 nm respectively. The Berkovich indenter was molded as a conical indenter with a half-cone angle of 70.3° based on the relation between the cross sectional area and depth. Nanoindentation was conducted at ambient temperature. In all indentation experiments conducted in

this work, the measured indenter tip drift rate was within ± 0.02 nm/s. The nanoindentation tester was calibrated by using glass and fused silica samples for a range of operating conditions. The H_{IT} and instrumented elastic modulus (E_{IT}) were estimated from the initial gradient of the unloading curves using the Oliver and Pharr model. Five measurements were carried out at each load on the samples.

Composites with cylindrical sliders (6 mm in diameter with a hemispherical tip) as pins and 440 stainless steel flat counterface (55 mm in diameter and 10 mm in thickness) as disk have been prepared to investigate the friction and wear properties under dry sliding condition. The disk was polished and the initial average surface roughness parameter (S_a) of disk was 1.14 ± 0.04 microns. The wear damage on rubbing surfaces was monitored with an optical profilometer and an optical microscope. The wear tests were performed in 700 MPa contact pressure, 25 mm/s of sliding speed and 1500 m of sliding distance.

The COF (coefficient of friction) values reported in this study are the average friction value obtained during each test. In addition, the linear wear-loss was acquired through a linear variable differential transducer (LVDT) with an encoder, which recorded the vertical displacement of the pin. After the tests, the worn surfaces were analyzed using SEM. The linear wear loss of each pin was converted into a volumetric wear loss using Eq. (1) derived from the geometry of a spherical cap.

$$V = \frac{\pi h^2}{3}(3r - h) \quad \text{Equation 4-1}$$

In Equation 4-1, h is the linear displacement (mm) in the vertical (longitudinal) axis for the pin, r is the pin radius (mm), which is assumed to be constant throughout the test, and V is the volumetric wear loss (mm^3). For a given testing condition, at least

three repetitive tests were performed and results of the average of the three tests are reported. A LEXT OLS4100 3-D Laser Confocal Microscopy is used for 2-D and 3-D imaging and dimensional measurements with a surface feature observation resolution of 20 nm.

4.3 Results and Discussion

4.3.1 Synthesis of composites starting with micron size TiO_2

According to the microstructure studied and reaction sequence discussed earlier, TiB_2 and Al_2O_3 reinforcement particles formed in Al-B melts (through the reaction of TiO_2 particles); where the size of the in-situ formed particles were controlled by the size of the TiO_2 particles (illustrated in Figure 30). When using stir reactive casting, micron sized TiO_2 was used in order to fabricate reinforcement in the matrix. It is experimentally demonstrated that TiB_2 and Al_2O_3 particles, with sizes ranging from 5-55 μm , were formed in-situ from micronized TiO_2 particles ($>44 \mu\text{m}$; with 25 μm average particle size) as shown in Figure 31. Few particles that have a size less than 100 nm have been observed. TiB_2 is a block-like particulate which has straight sides (Figure 32) while Al_2O_3 was an approximately spherical particulate. The interface between in-situ formed particulates and the aluminum matrix was clean and impurity-free.

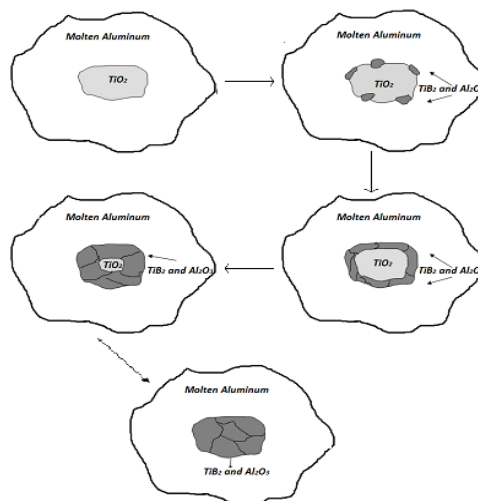


Figure 30 Schematic illustration of reaction products formed on particle/ liquid interface

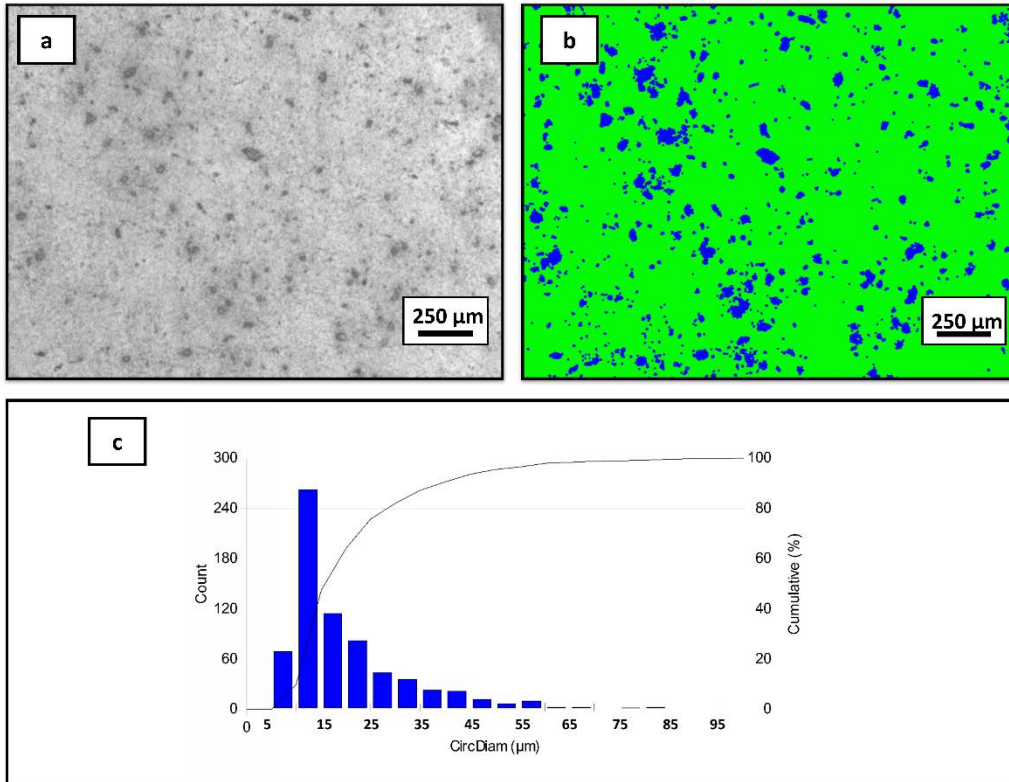


Figure 31 a) Optical microstructure of Aluminum/ ($TiB_2-Al_2O_3$) microcomposite starting with 25 μm TiO_2 precursor b) grey threshold in (a), c) phases volume percentage d)particle size distribution

One of the main drawbacks of using such large particles as a precursor was observed during stir casting. Even after an extended time of stirring, some powders would float to the surface or sink to the bottom of melt. Table 4 compares the density of the oxides and by-products which formed in the Al-TiO₂-B system. Unreacted TiO₂ identified in the powders were removed from the melt surface.

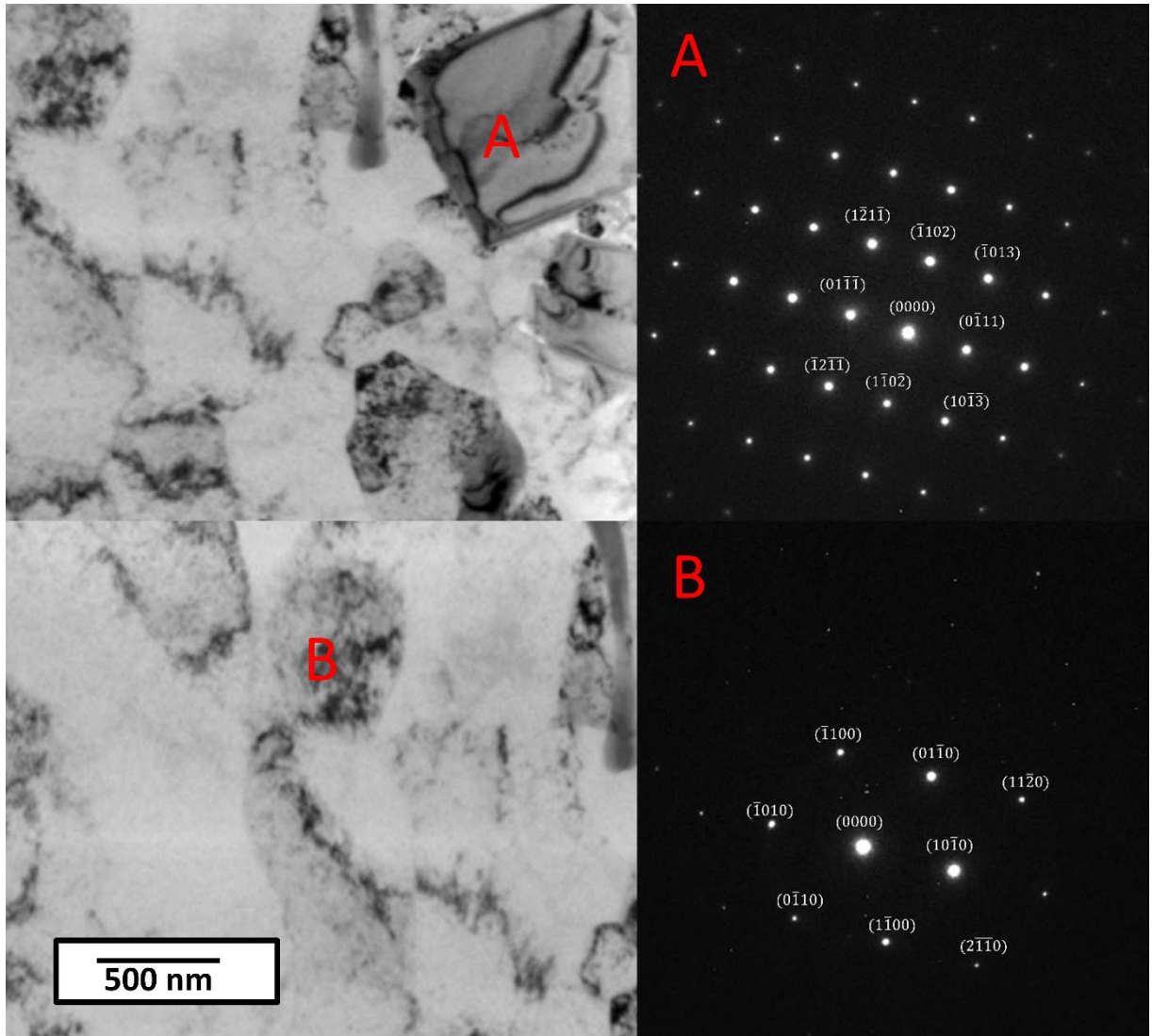


Figure 32 TEM image of Aluminum/(TiB₂-Al₂O₃ composite prepared starting with 25 μm TiO₂ precursor with Al₂O₃ and TiB₂ particles, labeled respectively

Table 4 Density, molar weight, and molar volume of different compounds present in the Al-B-TiO₂ system

| | Density (g/cm ³) | Molar weight (gr/mole) | Molar Volume (cm ³ /mole) |
|--------------------------------|------------------------------|------------------------|--------------------------------------|
| Aluminum | 2.70 | 27.00 | 10.00 |
| TiO ₂ | 4.23 | 80.00 | 18.91 |
| Al ₂ O ₃ | 3.95 | 102.00 | 25.82 |
| Al ₃ Ti | 3.4 | 128.00 | 37.88 |
| TiBO ₃ | 3.78 | 106.7 | 28.22 |
| Ti ₂ O ₃ | 4.49 | 143.73 | 32.01 |
| TiB ₂ | 4.52 | 69.5 | 15.37 |
| B ₂ O ₃ | 2.46 | 69.6 | 28.29 |

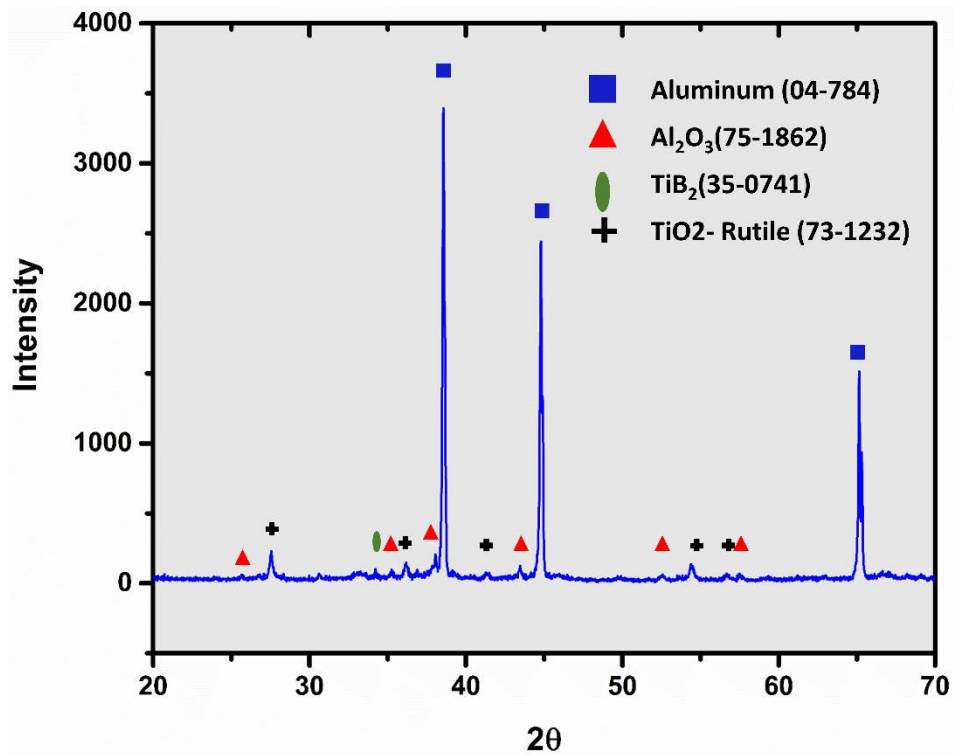


Figure 33 XRD pattern of the powders skimmed from the surface of the melt before pouring

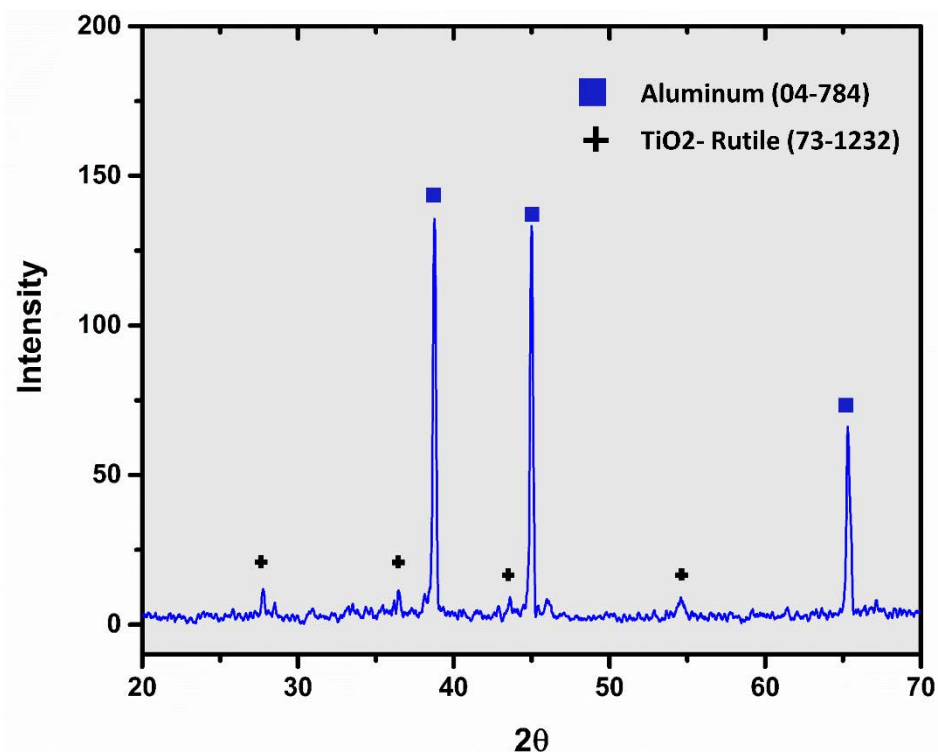


Figure 34 XRD pattern of the residual powders remained in the crucible after melt pouring

The XRD graphs in Figure 33 and Figure 34 shows the chemical composition of the powders removed from the bottom and the top of the melt before pouring. However, when the same experiment performed using nano size TiO_2 , the reaction occurred and TiB_2 formed in the matrix and a very negligible amount of powders floated or sank.

According to Stoke's law, a balanced expression for the drag force, F_k , acting on a single spherical particle moving, and a floating force, F_f , can be written. The floating velocity of a single spherical particle, V_0 , can be obtained as a function of diameter of the particle (d), the density difference of particle and liquid ($\rho_l - \rho_p$), and the viscosity of the liquid (μ):

$$V_0 = \frac{d^2(\rho_l - \rho_p)g}{18\mu} \quad \text{Equation 4-2}$$

According to Equation 4-2 the floating and sinking velocity is proportional to the square of particle diameter. Larger particles have higher tendency to float or sink. Moreover, the reaction of TiO_2 with other reactants have proven to be surface-controlled. Consequently, It means that the reaction occurs on the surface of the TiO_2 particles and, since they float or sink to the bottom of the crucible in case where the particle sizes are large, they do not have enough time to react, and the reaction does not go into the completion before floating or sinking. Secondly, smaller TiO_2 particles (25 nm compared to 44 μm) have a higher surface area available for reaction (Equation 4-3).

$$\frac{\text{Total surface available in nm particles } (A_n)}{\text{Total surface available in } \mu\text{m particles } (A_m)} = \frac{n_n \times 4\pi r_n^2}{n_m \times 4\pi r_m^2} = \frac{n_n}{n_m} \times \left(\frac{r_n}{r_m}\right)^2 \quad \text{Equation 4-3}$$

Where n_n is the number of nano-size particles with the radius of r_n and n_m is the number of micron-size particles with the radius of r_m .

For a constant volume fraction:

$$n_n \times \frac{4}{3} \pi r_n^3 = n_m \times \frac{4}{3} \pi r_m^3 \rightarrow \frac{n_n}{n_m} = \left(\frac{r_m}{r_n}\right)^3$$

Relating these two expressions together,

$$\frac{A_n}{A_m} = \frac{r_m}{r_n} \cong 2 * 10^3$$

Based on the results of these two expressions, it is shown that the available surface area for the reaction to occur is three times in magnitude higher in nano-sized particles compared to micron sized ones. In this study, since the reaction is surface controlled, the reduction rate can be increased greatly by exposing more reaction sites by introducing nano size particles in the melt. Therefore, that can be considered as one of the main reasons of proposing nano size TiO₂ particles as a precursor. In addition, the rate of settling of nanosize particles in the melt is also much lower than micronized particles, leaving more sites for reaction to occur.

4.3.2 Synthesis of composites starting with nano size TiO₂

Figure 35 shows the XRD pattern of aluminum/ (Al₂O₃-TiB₂) hybrid composite using nano-sized TiO₂ in aluminum melt as the starting precursor. The phases identified indicates the presence of TiB₂ as well as Al₂O₃. However, since the weight percent of reinforcing particles compared to the matrix is very low, detection of other compounds other than aluminum is complicated by using XRD. The high peak intensity of aluminum relative to other species leads to a very low signal in XRD at high magnification.

XRD graphs suggests that chemical reactions between aluminum, TiO_2 , and Boron have taken place completely. The theoretical fraction of the Al_2O_3 and TiB_2 reinforcement is 1.95 and 2 wt. %, respectively.

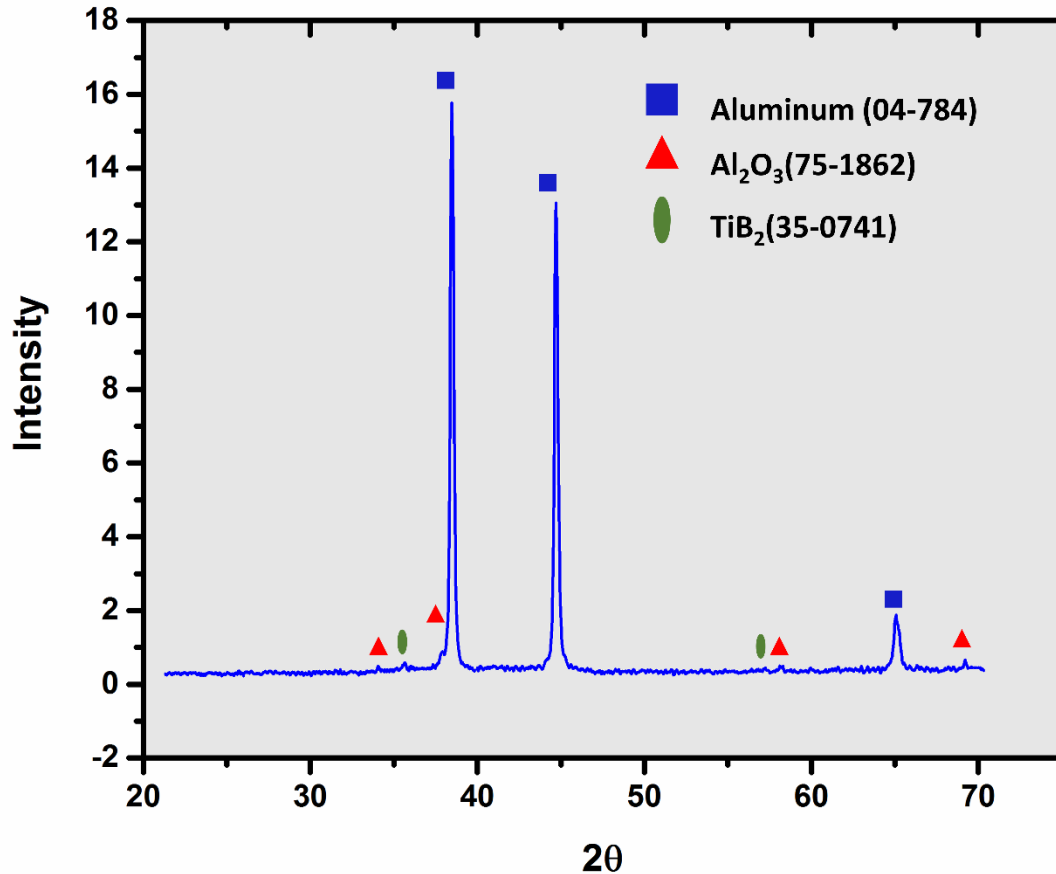


Figure 35 XRD pattern of the Al- ($\text{TiB}_2/\text{Al}_2\text{O}_3$) hybrid composite synthesized using stir casting

In this research, nanoparticles were extracted from the as cast hybrid composite samples for the further investigations. By an extraction experiment, the size distributions of particles can be analyzed as well. A small ingot was cut from the sample, and the surface of which was cleaned by sand paper. Then, the small ingot was dissolved in a 15 vol. % aqueous HCl solution in a beaker at room temperature. After dissolution, the HCl solution was decanted. The particles were then washed with water several times until the supernatant displayed neutral pH. These particles were

finally washed with ethanol, and then dried. Dynamic light scattering (DLS) was conducted to study the size distribution of particles which were carefully dispersed in the matrix presumably alumina and TiB_2 nanopowders. An aqueous suspension of nanoparticles, stabilized by sodium citrate solution at a 5 mM concentration prepared by ultrasound treatment of suspensions. Bimodal particle distributions which is determined by intensity of scattering in aqueous suspensions for the investigated nano powders are shown in Figure 36 and Figure 37. It was the same type and was characterized by the presence of two size fractions. Particle size distributions in these suspensions obtained by TEM and DLS are the same within experimental error.

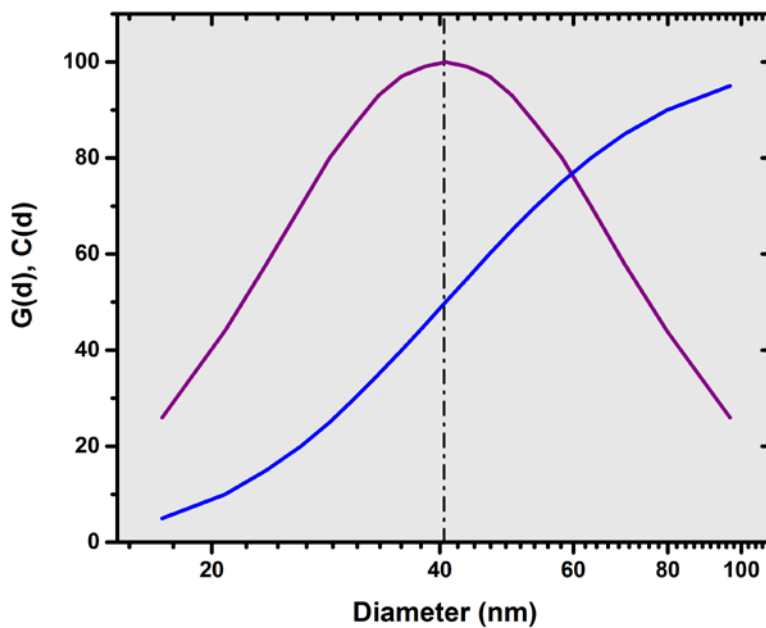


Figure 36 Particle size distribution of nanoparticles using DLS method

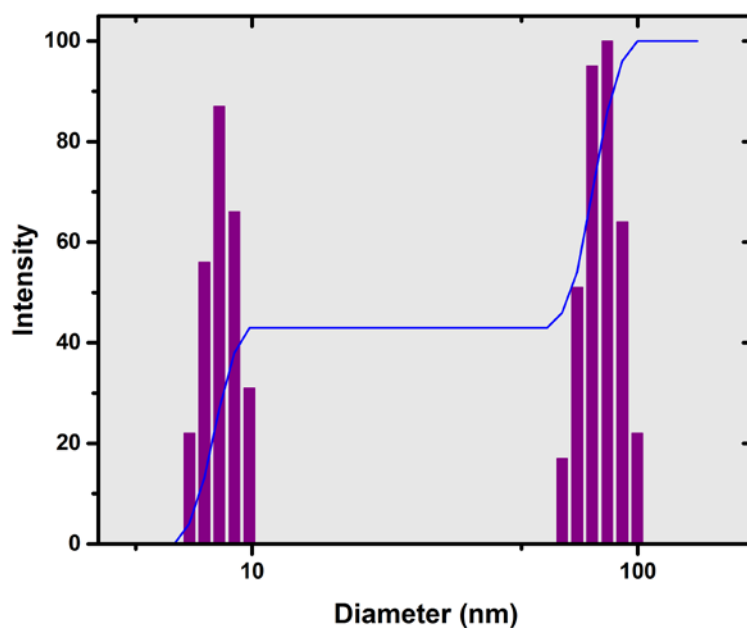


Figure 37 Bimodal particle size distribution of nanoparticles using DLS method

Dispersing nanoparticles uniformly in liquid metals is extremely difficult because of their poor wettability in a metal matrix and their large surface-to volume ratio, which easily induces agglomeration and clustering. In order to study the effect of mixing techniques involve in adding particulate reinforcements into a molten metal and dispersing them mechanically throughout the molten matrix metal, two mixing methods, stir mixing and ultrasonic mixing, have been investigated. In the first scenario an impeller is used to stir a melt that contains reactants, creating a vortex in the melt that is effective in dispersing the particles and insuring that the particles are wet by the melt. Figure 39a shows the nanocomposite prepared by in-situ mixing using reactive stir mixing. In the figure, it is shown that the particles are more aggregated and restricted to grain boundary regions.

During mechanical mixing, the interactions between particle clusters and eddies in turbulent flow have the potential to cause mechanical dispersion of nanoparticles. The

intensity of shear associated with these interactions is dependent on the relative sizes of the eddies and particle aggregates. If the particles are smaller relative to the eddies, they tend to be captured or entrained in the eddies as shown in Figure 38. As fluid motion within the eddies is laminar, there is little relative motion of the particles. On average, therefore, if the particle clusters are smaller than the eddies, the shear effects of eddy-cluster interactions are minimal. Within eddies, there is little mixing because of the rotating flow occurring in streamlines. A much higher shear stresses results when several eddies with opposing rotation interact with the particle clusters simultaneously. It has been found experimentally that detrimental effects start to occur when the Kolmogorov scale for eddy size, λ , drops below $2/3 \sim 1/2$ of the diameter of the clusters. Excessive agitation leads to formation of eddies with size small enough and of sufficient energy to cause damage to the clusters. Calculations shows that for a system having the values listed in Table 5, the Kolmogorov scale for eddy size drops is in the range of 10 μm .

Fluid mass in the impeller zone, p_m , is roughly equal to ρD_i^3 where ρ is aluminum melt density and D_i is impeller diameter (Equation 4-4). Therefore, the stirrer power P is equal to:

$$P_m = p / \rho D_i^3 = 0.264 \text{ W} / 2700 \text{ Kg/m}^3 \times (36 \times 10^{-3})^3 \text{ m}^3 = 2.09 \text{ m}^2 \text{ S}^{-3} \quad \text{Equation 4-4}$$

The Kolmogorov length scale of mixing, λ , can be calculated using Equation 4-5 where dynamic viscosity, v , is equal to viscosity over density, μ/ρ

$$\lambda = \left(\frac{v^3}{P_m} \right)^{\frac{1}{4}} = \left(\frac{\left(\frac{1.1 \text{ to } 1.4 \times 10^{-3}}{2700} \right)^3}{0.0021} \right)^{\frac{1}{4}} = 13.4 \text{ to } 16.0 \mu\text{m} \quad \text{Equation 4-5}$$

These calculations shows that by using the mechanical stirrer the aggregates approximately larger than 20-30 μm can be deagglomerated by the turbulent shear damage of clusters.

Table 5 Stir mixing experimental parameters

| Parameter | Value | Units |
|---------------------|---------|----------------|
| Volume | 0.001 | m ³ |
| Vessel Diameter | 90 | mm |
| Liquid Level | 80 | mm |
| Agitator Diameter | 36 | mm |
| Equivalent Diameter | 86.5 | mm |
| Shaft Speed | 500 | rpm |
| Power | 2.64e-4 | kW |

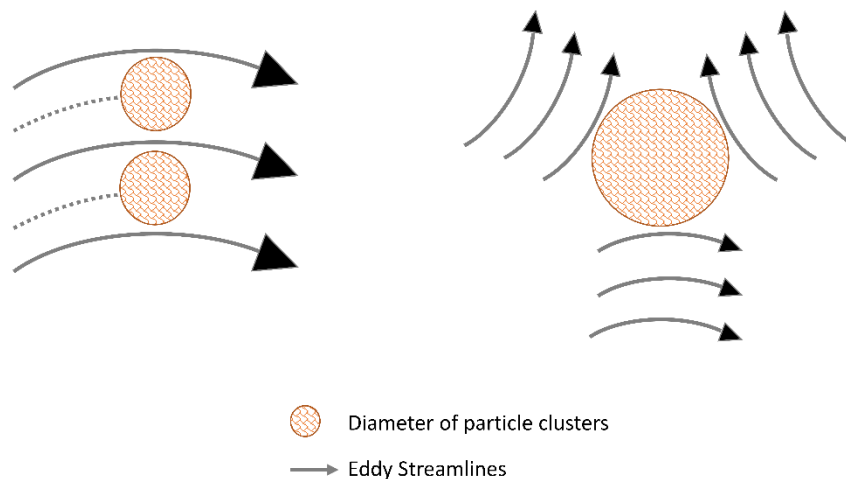


Figure 38 Particle- Eddy streamline interaction

During ultrasonic mixing, an ultrasonic horn creates cavitation in the melt by a gas streaming effect related to the formation and collapse of bubbles generated in the melt. Cavitation bubble collapse is a remarkable phenomenon induced throughout the liquid by the power of sound. In aqueous systems at an ultrasonic frequency of 20kHz each cavitation bubble collapse acts as a localized hotspot generating temperatures of about 4,000 K and pressures in excess of 1000 atmospheres. During the rarefaction phase,

the surface of the cavities expands to many times that of stable bubbles, and the pressure inside the cavities decrease to almost zero. During the compression phase, cavities collapse, and there is a sudden dramatic increase in pressure. Therefore, acoustic cavitation can produce dramatic effects on powders suspended in a liquid. Surface imperfections or trapped gas can act as the nuclei for cavitation bubble formation on the surface of a particle and subsequent surface collapse can then lead to shock waves which break the particle apart. Cavitation bubble collapse in the liquid phase near to a particle can force it into rapid motion. The gas streaming in the melt then disperses the reinforcement agents throughout the liquid metal. Figure 39b shows the TEM micrograph of the microstructure exhibited by a cast nanocomposite synthesized using a combined stir mixing and ultrasonic mixing, with a wetting agent added to the molten metal. Both methods of stirring were needed to disperse nanoparticles in the metal matrix. This process resulted in the incorporation of nanoparticles within microscale grains of aluminum and formed a tri-modal microstructure. As it can be observed, particles (marked by blue arrows) has a size variation between 8-15 nm, and particles (marked by red arrows) has a size variation between 50-150 nm within the microscale grains of alpha-aluminum. Ceramic nanoparticles may be uniformly dispersed in metal matrices to increase the tensile strength and wear resistance using ultrasonic cavitation of the melt to further disperse the particles. The TEM micrograph is also showing that the reinforcement phases are not too agglomerated and are not only restricted to the grain boundaries.

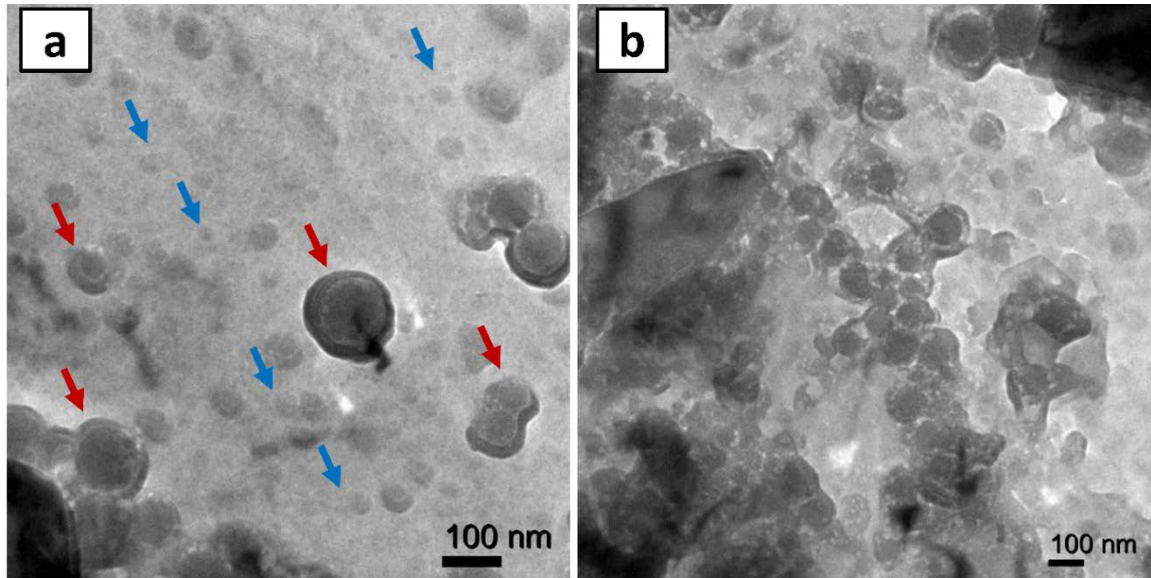


Figure 39 TEM of aluminum/ ($TiB_2-Al_2O_3$) nanocomposites produced by liquid stir casting a) In-situ stir mixing b) In-situ stir/ultrasonic mixing

4.3.3 Comparison of mechanical properties of micro and nanocomposites

In order to compare the properties of hybrid composites prepared starting with micron or nano TiO_2 precursors, microstructures, mechanical properties, and fracture surfaces of the test specimens were investigated. Table 6 summarizes the grain size, mechanical properties, and tribological properties of the micro and nanocomposites reinforced with 4wt% hybrid particles under varying processing conditions.

The optical macrographs of the unreinforced, and composites processed at similar conditions containing 4 weight percent of micron and nano sized particles is shown in Figure 40. In polycrystalline materials, grains tend to grow to maintain the lowest level of energy in the system. However, a dispersion of second-phase particles helps preventing the grain growth by pinning and impedes the migration of the grain boundaries. By decreasing the particle size the pinning effect will be intensified due to

the larger number of particles for a constant volume fraction. Figure 40b and c, show the microstructure of composite specimens made with b) micronized TiO₂, c) nanosized TiO₂ particles. Grain size analysis shows that the grain size is smaller in composites made by nano-sized precursor.

Table 6 Summary of average properties of the micro and nanocomposites reinforced with 4wt% hybrid particles at various processing condition.

| | Temp. (°C) | Time (min) | Grain size (um) | Hardness (HV) | Yield Stress (MPa) | Elongation (%) | UTS (MPa) |
|-----------------------|------------|------------|-----------------|---------------|--------------------|----------------|-----------|
| Unreinforced Aluminum | 700 | - | 330 | 41.9±1.5 | 39.1±0.1 | 60±4 | 56±3 |
| Unreinforced Aluminum | 850 | - | 580 | 39.3±1.6 | 29.9±0.2 | 52±5 | 55±2 |
| Unreinforced Aluminum | 1000 | - | 780 | 37.5±1.6 | 25.2±0.7 | 58±0.5 | 56±3 |
| Hybrid Microcomposite | 700 | 5 | - | 45.1±2.6 | 33.3±6.2 | 38±14 | 62±3 |
| Hybrid Microcomposite | 700 | 15 | - | 48.7±2.3 | 36.5±3.1 | 28±5 | 70±1 |
| Hybrid Microcomposite | 1000 | 5 | - | 59.2±5.0 | 41.1±0.9 | 28±8 | 75±7 |
| Hybrid Microcomposite | 1000 | 15 | - | 59.0±2.6 | 40.3±1.5 | 18±2 | 77±4 |
| Hybrid Nanocomposite | 700 | 5 | 330 | 49.1±1.3 | 40.0±4.3 | 58±8 | 131±1 |
| Hybrid Nanocomposite | 700 | 10 | 310 | 64.4±0.7 | 66.7±4.3 | 61±5 | 152±2 |
| Hybrid Nanocomposite | 700 | 15 | 280 | 37.9±0.6 | 65.6±1.9 | 44±3 | 150±2 |
| Hybrid Nanocomposite | 850 | 5 | 300 | 59.2±4.3 | 62.3±1.4 | 47±2 | 162±3 |
| Hybrid Nanocomposite | 850 | 10 | 200 | 77.4±3.9 | 90.1±0.8 | 53±4 | 232±2 |
| Hybrid Nanocomposite | 850 | 15 | 140 | 562.1 ±2.1 | 84.8±1.1 | 58±2 | 223±1 |
| Hybrid Nanocomposite | 1000 | 5 | 330 | 63.2±1.5 | 66.5±2.1 | 52±1 | 191±1 |
| Hybrid Nanocomposite | 1000 | 10 | 140 | 81.1±1.9 | 71.8±1.2 | 53±2 | 134±2 |
| Hybrid Nanocomposite | 1000 | 15 | 80 | 56.4±0.9 | 76.2±4.1 | 43±5 | 208±2 |

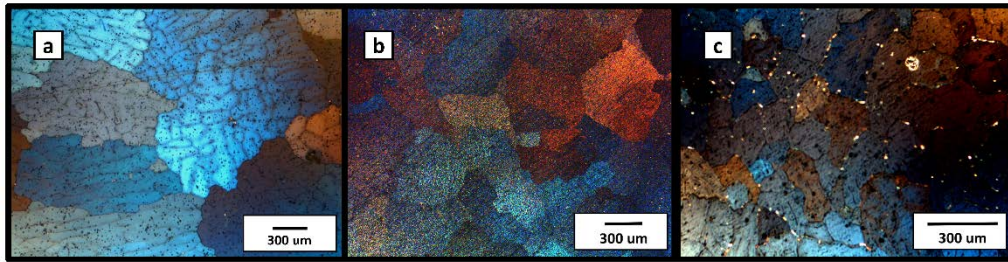


Figure 40 The cross polarized optical macrograph of (a) the unreinforced aluminum, (b) the microcomposite, and (c) The nanocomposite processed at similar conditions containing 4 weight percent reinforcement

Figure 41 shows the tensile stress-strain curves of the microcomposites (composites synthesized with micron sized TiO_2 as precursor) and nanocomposites (composites synthesized with nano sized TiO_2 as precursor) reinforced with hybrid particles. Based on the results, nanocomposites show a different tensile behavior compared with that of the microcomposites. It is apparent that although by addition of hard ceramic particles (TiB_2 and Al_2O_3) in microcomposites, the tensile strength is higher, but the ductility of the composite decreases significantly compared to the base alloy. Furthermore, there is a significant increase in tensile properties when a nanosize TiO_2 is used as a starting material.

In general metal matrix composites exhibit high hardness and tensile properties as well as good wear resistance. Assuming a uniform distribution of particles within the matrix, at a constant particle volume fraction, the particles' spacing will decrease as the average particle size decreases. The strength and hardness of samples increase with decreasing the particle size. This is a result of hindering of dislocations movement due to increase in the particle concentration and decrease in the grain size of the aluminum matrix. Additionally, it can be obviously seen that nanocomposites show improved tensile ductility in comparison with microcomposites. Crack propagation in

the nanocomposites region is retarded by blunting mechanism of nanoparticles.

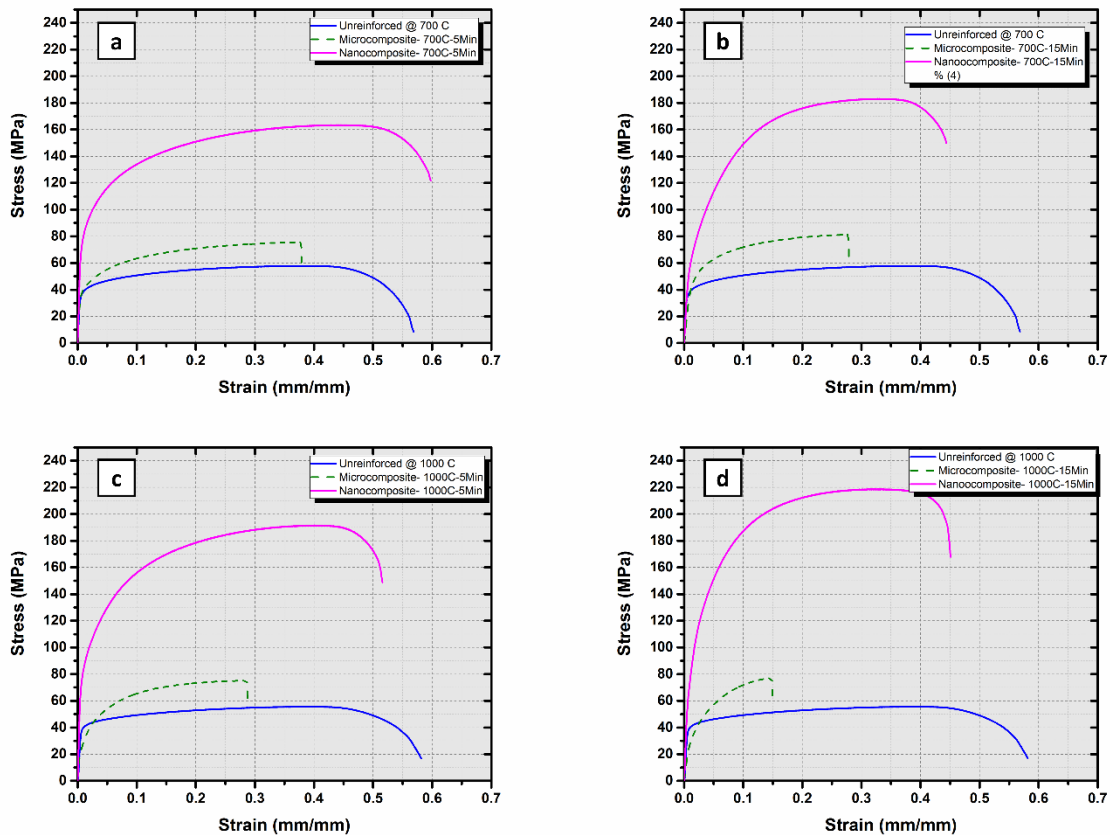


Figure 41 The engineering stress-strain curves of (a) microcomposites reinforced with 4wt% hybrid particles at 700°C, (b) microcomposites reinforced with 4wt% hybrid particles at 1000°C, (c) nanocomposites reinforced with 4wt% hybrid particles at 700 °C, (d) nanocomposites reinforced with 4wt% hybrid particles at 850 °C, and (e) nanocomposites reinforced with 4wt% hybrid particles at 1000 °C.

The macroscopic crack path can provide useful information about the failure of the samples. The fracture surfaces of tensile tested samples can also provide valuable information pertaining to microstructural effects on tensile ductility and fracture properties of the aluminum hybrid nano and microcomposites. Failure in particulate reinforced metal composites can be explained by various mechanisms including the matrix reinforcement interfacial decohesion, reinforcement fracture, and failure in the matrix [140-142]

Figure 42 shows macro fractographs of unreinforced, micro, and nano particle reinforced composite tensile specimens. During tensile testing, the unreinforced specimen underwent necking and finally fractured, whereas the microcomposite specimens failed across the shear planes. The mixed type fracture has been observed in the nanocomposite tensile specimens (Figure 43).

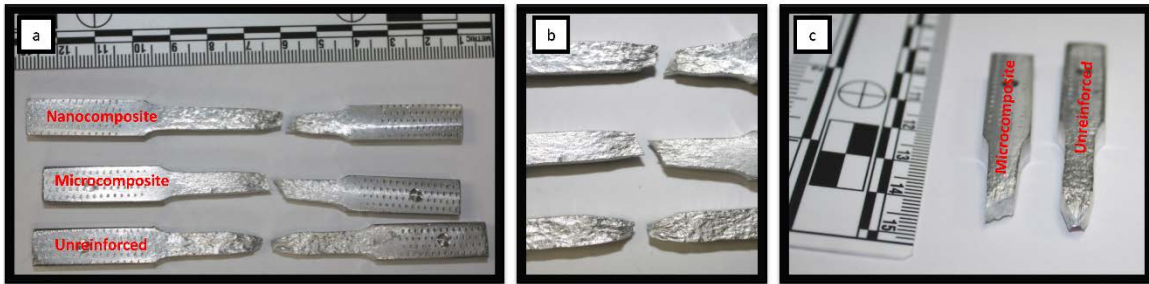


Figure 42 Macro fractographs of unreinforced, micron, and nano particle reinforced composite tensile specimens

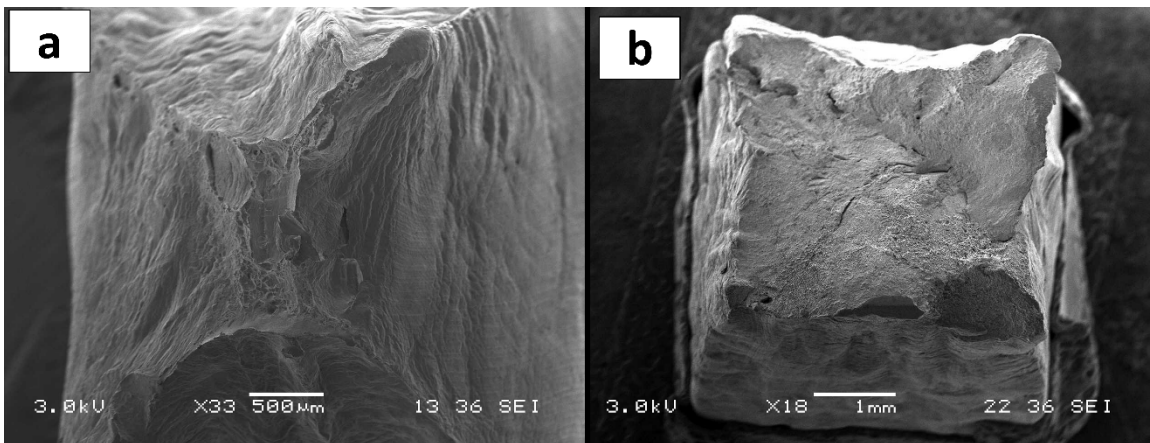


Figure 43 micro fractographs of unreinforced and nano particle reinforced composite tensile specimens

Metal matrix composites behave differently from pure metals. There are many mechanisms which can be associated with the failure in MMCs. The damage or failure can be associated with the breaking and decohering of the reinforcement with the metal matrix. Additionally, the fracture and decohesion of the reinforcing particles have a

detrimental effect on the overall load-bearing capacity of the composite. The reinforcements may also distribute at the grain boundaries of the base matrix metal during the synthesis. Additionally the ductility of popular reinforcements are quite low compared to the metallic matrices. Thus they obstruct ductile deformation and movement of dislocations along the grains of the matrix, and abrupt brittle fracture is obtained during the tensile test. The coarser the reinforcement, the more brittle the MMC becomes.

The SEM fractography of Al/(Al₂O₃- TiB₂) hybrid microcomposites and Al/(Al₂O₃- TiB₂) hybrid nanocomposites are shown in Figure 44 and Figure 45. The difference in the appearance of fracture surfaces between nanocomposite and microcomposite at the same magnification (Figure 44b and Figure 45b) was significant. The SEM micrographs of the fracture surface of the unreinforced aluminum matrix, which includes dimples and voids, demonstrates a ductile fracture. For the nanocomposites synthesized by in-situ reaction, many dispersed shallow and small dimples with varying sizes were found in the matrix as shown in Figure 45., while in the microcomposite a cleavage and matrix rupture was also observed. In the Al/(Al₂O₃- TiB₂) nanocomposite, dimples with some pull-out were observed, indicating that fracture still exhibited the ductility of the aluminum matrix despite the incorporation of the reinforcement.

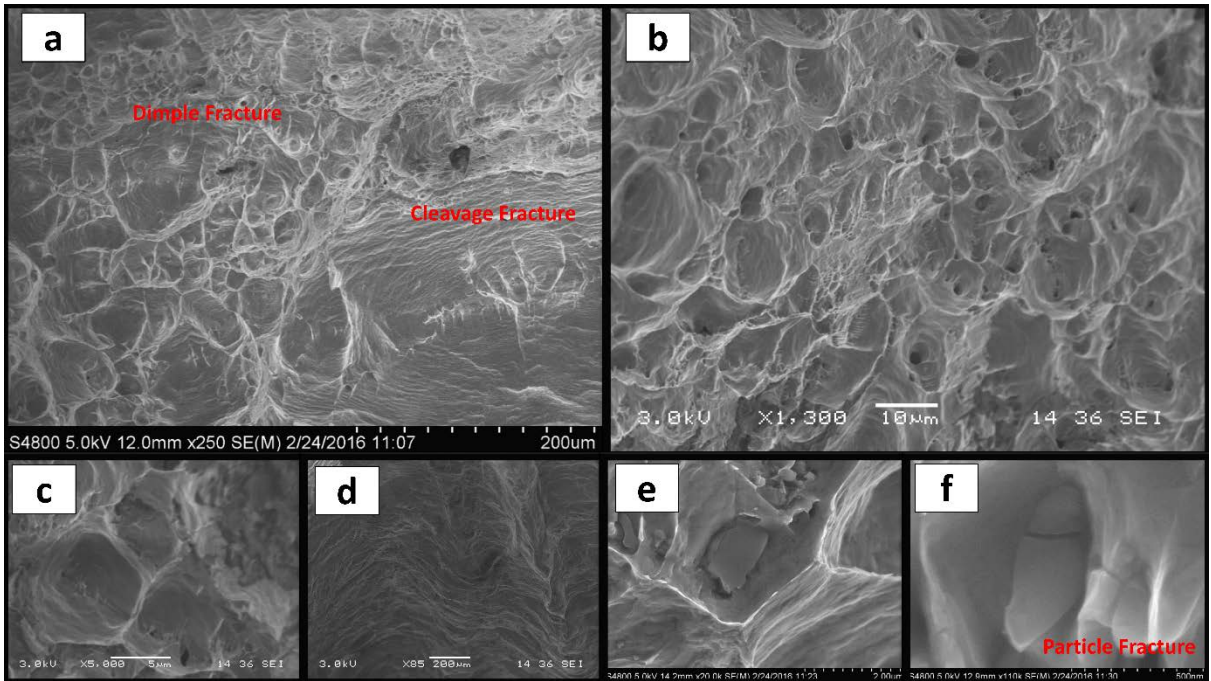


Figure 44 Tensile specimen fracture surface of the microcomposites reinforced with hybrid particles

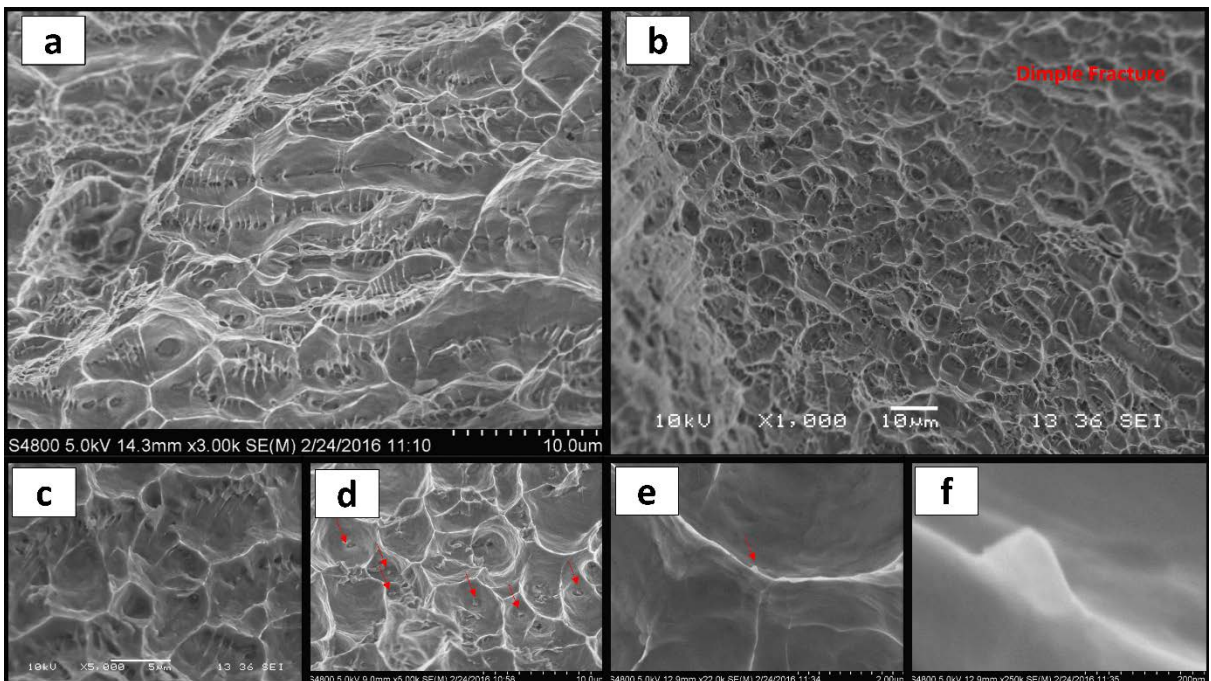


Figure 45 Tensile specimen fracture surface of the nanocomposites reinforced with hybrid particles

The microcomposites possess both dimple-like characteristics and cleavage-like features where can be seen in various areas on the fracture surfaces. The presence of hard, brittle, and essentially elastically deforming reinforcing particles constrains the mechanical deformation of the soft, ductile, and plastically deforming alloy matrix; and as a result, a triaxial stress state is developed in the matrix, which limit the flow stress of the composite. For the microcomposite synthesized by an in-situ reaction, there are a number of large voids on the tensile fracture surface shown in Figure 44 b. Some larger dimples are linked together along the boundaries, showing increased degree of clustering along the grain boundaries. Furthermore, the agglomeration of particles was found in the dimples which provided sites for crack initiation (Figure 44e). The fractograph of the composite shows a mixture of brittle and dimple fracture.

In general, the total energy of the fracture is related to the size of the dimples. The presence of small and deep dimples in Figure 45 suggests a ductile fracture mode and confirms the improved ductility of nanocomposites. All of the SEM fractographs were correlated very well to the corresponding elongation values for the mentioned nanocomposites. In the nanocomposites, SEM images show that the local deformation of the matrix near the reinforcement led to increase in the strain to failure. Furthermore, presence of nano-sized particles (indicated with an arrow) in the dimples shows that the interfacial bond strength between in-situ nano-sized particles and the matrix aluminum is high. Nanoparticles which are embedded in the dimples of the aluminum matrix and partially projected shows that the crack has propagated around the nanoparticles. In order to study the failure mechanism by comparing the path of fracture with the metallographic grain structure (Figure 46), it is obvious that the failure is having a transgranular nature which can be as a result of microvoid nucleation and coalescence. However, at some specific regions, the occurrence of intergranular

fracture was observed, where the second phase particles were located along the grain boundaries (Figure 46c). The accumulation of agglomerated nanoparticles are occasionally observed in the grain boundaries which can affect the aluminum matrix cohesion and act as preferential fracture point.

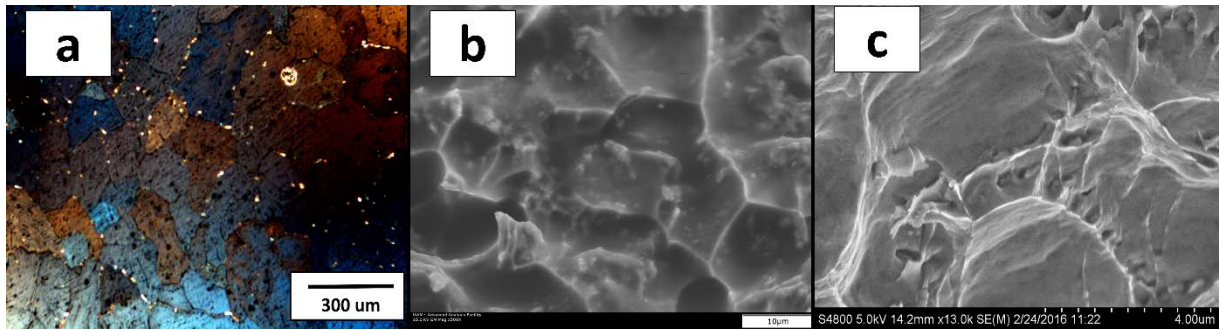


Figure 46 (a) The cross polarized optical micrograph, and (b,c) the SEM fracture surface micrograph of Al/ (TiB₂- Al₂O₃) hybrid nanocomposites

4.3.4 Variation of mechanical properties with reinforcement content

One of the main factors that may influence the mechanical properties of composites is volume fraction of nanoparticles. It should be mentioned that the weight fraction of reinforcements in the matrix were calculated based on the assumption that all of the TiO₂ and Boron added to the melt have converted to Al₂O₃ and TiB₂, which were confirmed by XRD. The composites with 0, 0.1, 2, 4, and 8 wt% nanosize reinforcements were synthesized to examine the effect of nanoparticle loading on mechanical properties of the nanocomposites including hardness and elastic modulus. Table 7 is listing the estimated volume fraction and weight percent of each Al₂O₃ and TiB₂ separately. The instrumented nano indentation method was used to measure the hardness and elastic modulus of a material from indentation load– displacement data obtained during cycles of loading and unloading.

Table 7 Estimated reinforcement loading in the composites

| Calculated Reinforcement loading (wt.%) | Calculated Reinforcement loading (Vf) | Estimated Al ₂ O ₃ content (wt.%) | Estimated TiB ₂ content (wt.%) |
|-----------------------------------------|---------------------------------------|---------------------------------------------------------|-------------------------------------------|
| 0 | 0 | 0 | 0 |
| 0.1 | 0.13 | 0.049 | 0.051 |
| 2 | 1.29 | 0.99 | 1.01 |
| 4 | 2.6 | 1.97 | 2.03 |
| 8 | 5.27 | 3.95 | 4.05 |

In the instrumented nano indentation method, the penetration depth and the applied load were monitored both during the insertion and withdrawal of the indenter, resulting in a loading and unloading curve of the applied load as a function of the penetration depth.

A typical load versus displacement curve resulting from such an indentation test may be seen in Figure 47. At point A the indenter touches the metal, and the load increases along curve AB as the indenter penetrates into the metal. During unloading the curve is along the BC line. For a perfectly elastic material, there will be no hysteresis. Therefore, information on the plastic and elastic properties of the nanocomposites can be obtained from the penetration depth of inventor into the material as a function of the applied load.

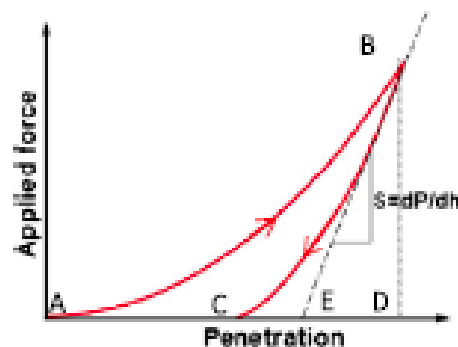


Figure 47 Typical curve of load versus penetration depth in an indentation test.

The hardness and elastic modulus of the reinforced aluminum composite can be estimated from the measured curves in Figure 48. Hardness is defined as the resistance of permanent (plastic) deformation caused by nanoindentation. Thus, what is being measured with this technique is the plastic deformation of the surface. The modulus and hardness values were averaged in the indentation depth range of 150–3000 nm into the surface.

Figure 48, which shows the load– displacement curves during cycles of loading and unloading for unreinforced aluminum and its nanocomposites as a function of particle concentration, shows that upon loading, the curves move upward with increasing particle content. This indicates that the resistance to indentation of nanocomposites is enhanced by increasing nanoparticles concentration. The penetration depth represents the contributions from both the elastic and plastic displacements.

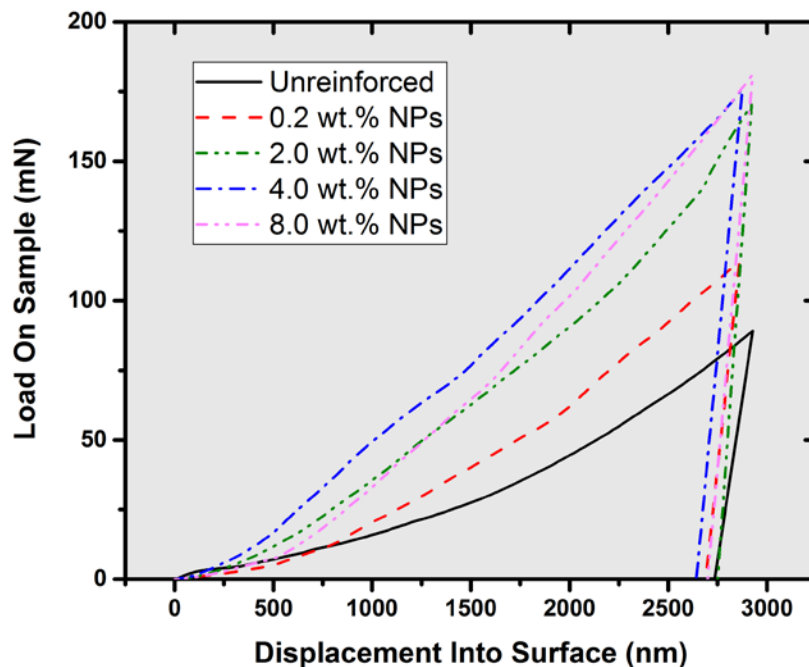


Figure 48 The force displacement diagram of Nano indentation test.

Table 8 Measured values for elastic modulus and hardness of particle reinforced aluminum nanocomposites

| Specimen | Avg Elastic Modulus (GPa) | Avg Hardness (GPa) | Predicted Modulus (GPa) |
|--------------------|---------------------------|--------------------|-------------------------|
| Unreinforced alloy | 63.1±5.0 | 0.94±0.05 | 62 |
| Al- 0.2wt.% NPs | 64.3±4.6 | 1.12±0.05 | 62.1 |
| Al- 2wt.% NPs | 66.7±3.1 | 1.85±0.03 | 63.2 |
| Al- 4wt.% NPs | 69.1±8.4 | 2.82±0.18 | 64.4 |
| Al- 8wt.% NPs | 72.0±12.4 | 1.41±0.18 | 67.1 |

The hardness and modulus of all the samples were plotted as a function of nano particle loading, as shown in

Figure 49 and listed in Table 8. Both the elastic modulus and hardness increase with increasing particle loading. With addition of 2 wt% of nanoparticles, the hardness was improved by about 50%, as compared with its unreinforced counterpart. This increase in hardness is due to the increase in the volume fraction of nanoparticles which contributes to the strengthening of the matrix. It is also found that no hardness improvement by further increasing the nano particle content above 4 wt%. One possible theory is related to the nanoparticles distribution within the matrix. Upon solidification it is expected that the amount of rejected NPs to the last freezing zone is enhanced by increasing the loading in the molten alloy. The particles pushed to the interface will be trapped and clustered at the boundaries, and this will lead to the embrittlement of the composite.

Several theoretical models exist today, which predict the modulus of MMC's reinforced by particulates. Among them, the rule of mixture which is the weighted

average of the components, is almost inaccurate in predicting the modulus. However, it has been shown experimentally that the average modulus predicted by the Hashin-Shtrikman model can be a good fit to experimental data points [143]. In this regard, the modulus of composites with various reinforcement content have been calculated using:

$$E_c = E_m \frac{E_m V_m + E_p (V_p + 1)}{E_p V_m + E_m (V_p + 1)}$$

Where E_c , E_m , and E_p is the Young's modulus of composite, the matrix, and the particles, respectively, and V_m and V_p are the volume fractions of the matrix and particles. Figure 50 shows the predicted and experimental value of Young's modulus. The experimental data is in correspondence with the analytical model with the increase of reinforcement content.

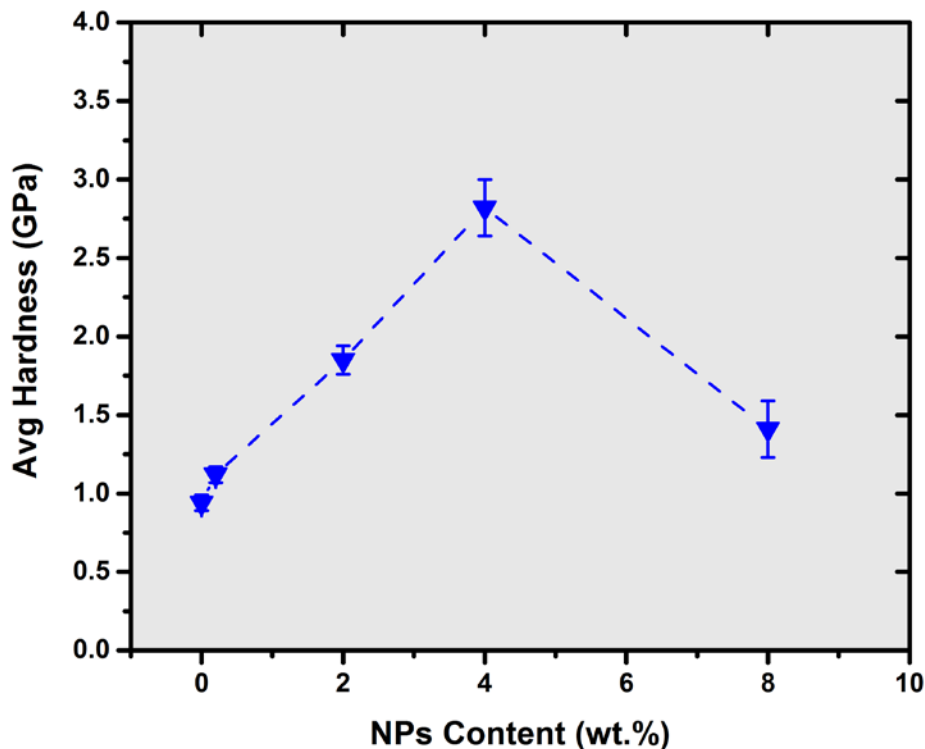


Figure 49 Average Elastic Modulus values for aluminum and its nanocomposites as a function of particle loading.

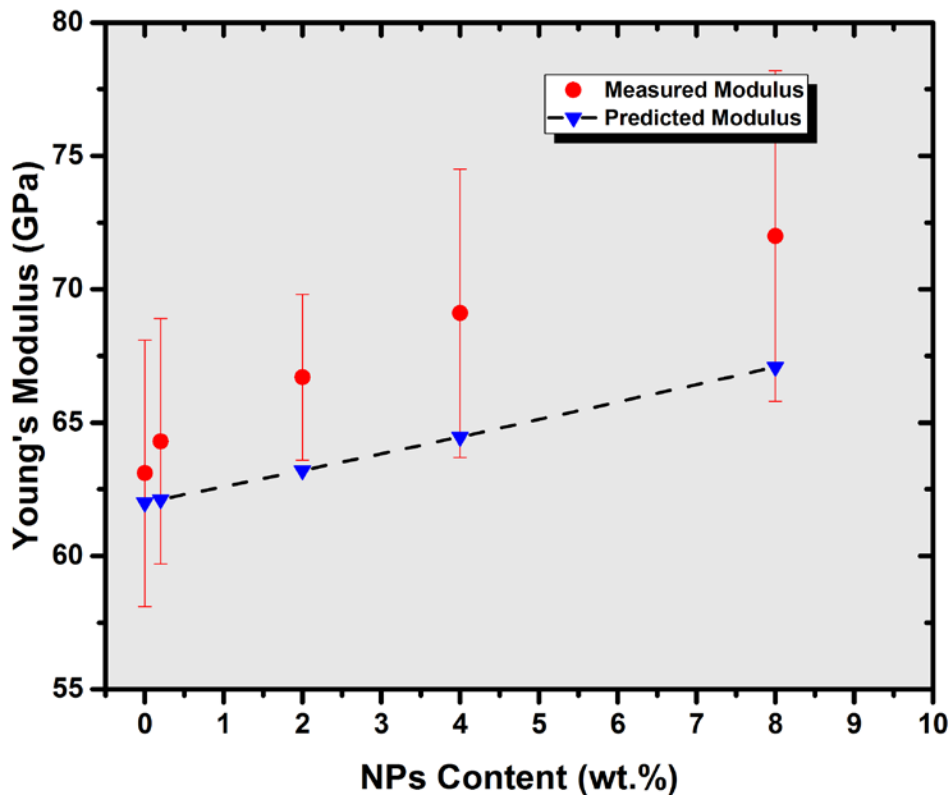


Figure 50 Comparison between theoretical prediction and experimental data using the Hashin- Shtrikman analytical model.

4.3.5 Variation of properties with processing parameters

Processing, structure and property relationships provide important information for the development of microstructures for improved performance. The following section provide insight in the processing conditions in relation to their structure and the effect of the addition of nanoparticles on the mechanical properties.

There is evidence that the introduction of NPs into a metal matrix results in some grain refinement effect, addition of particles reduces the size of the grains in the MMNCs compared to the un-reinforced metal processed under the same conditions. The improvement of yield strength due to grain refinement, is dependent on the extent of effectiveness of NPs in reducing grain size using following equation:

$$\Delta\sigma_{Grain\ refinement} = K \left(\frac{1}{\sqrt{D_{m,T}}} - \frac{1}{\sqrt{D_{0,T}}} \right)$$

where $D_{M,T}$ and $D_{0,T}$ are the average grain diameters of polycrystalline matrix materials in presence of NPs and when particles are absent processed at temperature T , respectively.

In Figure 51, the measured grain size for various superheats of the castings is presented. It can be seen that the grain size increases linearly with increasing pouring temperature. The data collected and the slope of the linear fit, can represent the average pouring temperature dependent crystallite growth rate of the matrix.

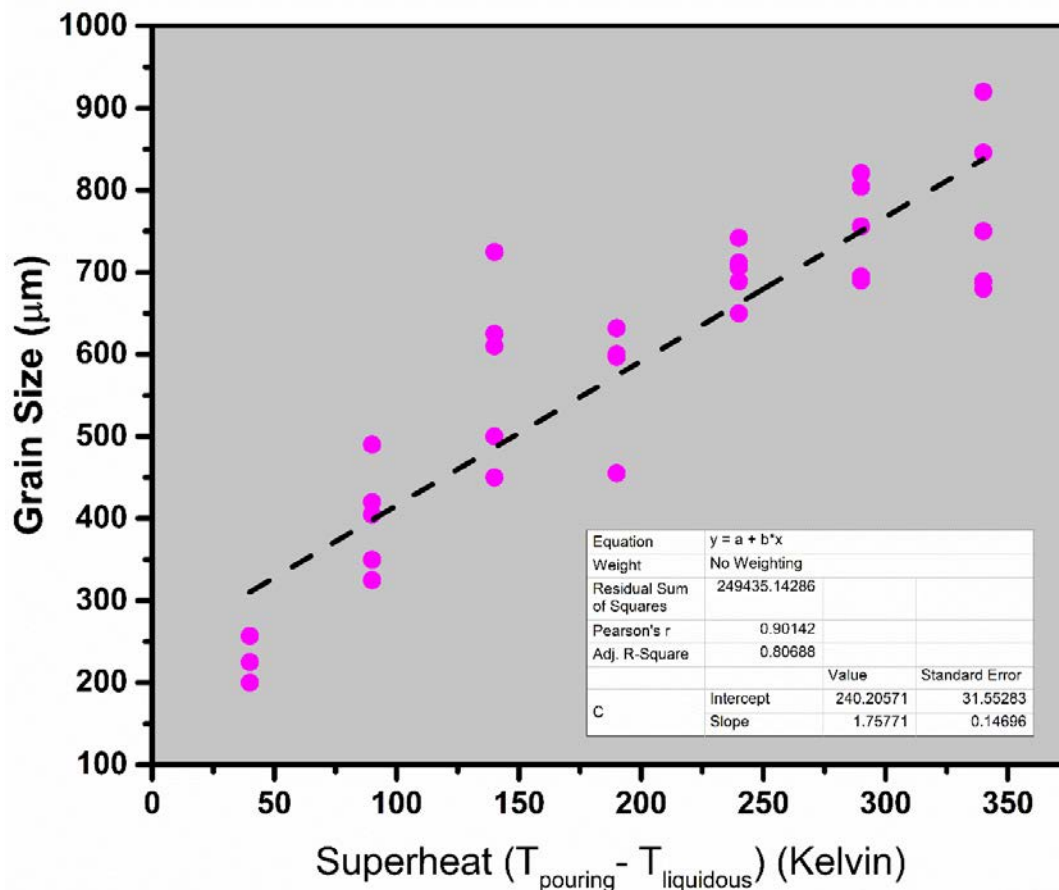


Figure 51 The grain size variation by pouring temperature of aluminum melt

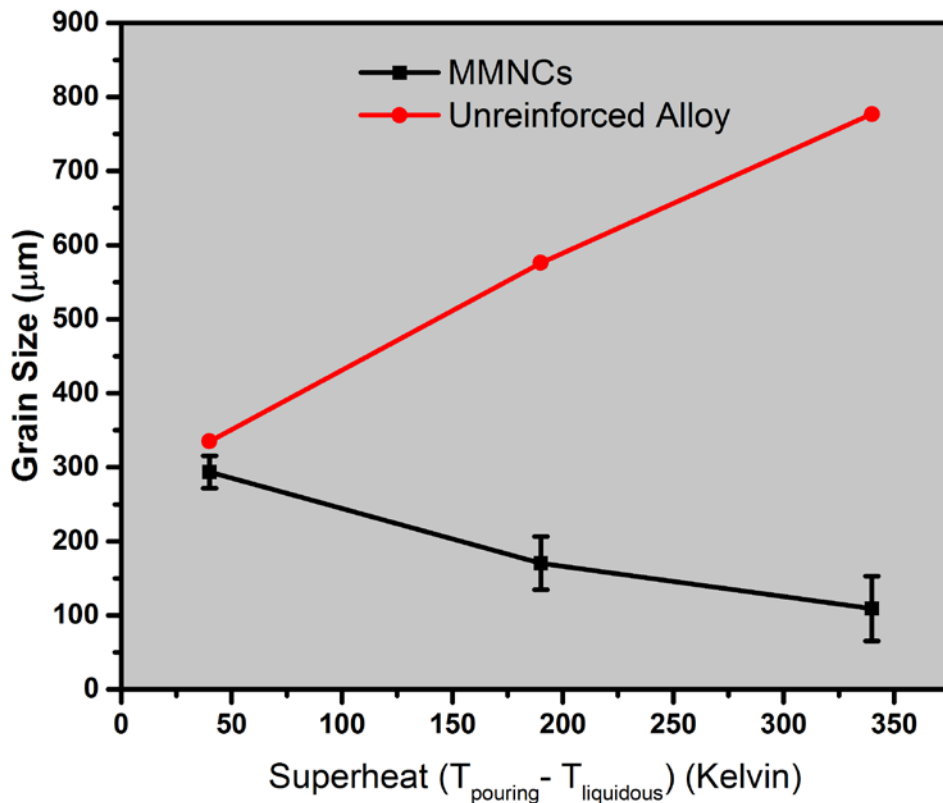


Figure 52 The grain size variation by mixing temperature for unreinforced and particle reinforced composites

The addition of NPs to a metal matrix acts to refine the grain size by restricting the size of the grains in the MMNC rather than nucleating new grains. As shown in Figure 52, the addition of NPs at various temperatures decreased the grain size of the matrix. For such indirect impacts of NP addition, the grain boundary pinning of added particles during processing is dependent on the size of the particles at a constant volume fraction [31]. Therefore, at a constant volume fraction, by varying the particle size it is expected that the nanocomposite hardness and yield stress will change as a result of grain refinement. In summary, for smaller particles, the NPs can restrict the size of the grains in the MMNC more effectively.

In order to compensate the effect of pouring temperature on the unreinforced matrix, and to only consider the effect of nanoparticles in grain refinement, a normalized factor,

refinement ratio, R , is proposed. R for each nanocomposite can be calculated by the ratio of the grain size of the nanocomposite to the grain size of the matrix without any reinforcing particles at a specific mixing and pouring temperature.

$$R = \frac{D_{m,T}}{D_{0,T}}$$

In the following text, we will study the effect of processing parameter on the refinement ratio ($D_{M,T}/D_{0,T}$) of the nanocomposites.

Based on the results discussed earlier in chapter 4, during the reduction of TiO_2 in the melt, TiB_2 forms on the surface of TiO_2 particles in the form of nodules. Interfacial stress will be present at the TiO_2/TiB_2 interface which causes the detachment of nodules from the TiO_2 surface. During stir casting the turbulent flow removes the concentration gradient. According to Prandtl, a thin region adjacent to the particle boundary, the flow is retarded because of the effect of viscosity. In the regions beyond the thin boundary layer, the velocity is uniform and the effect of viscosity is no longer significant. The thickness of the thin boundary layer, δ , is an important factor which determines the detachment of TiB_2 nodules of the TiO_2 surface. The drag forces acting on the nodules by the molten metal is a function of viscosity of the melt. Therefore, it is reasonable to assume that during stir mixing, viscosity is the factor which determines the size of nodules where the detachment take place. Figure 53 shows schematically how the thickness of the boundary layer can be correlated to the detachment of TiB_2 nanoparticles during mixing.

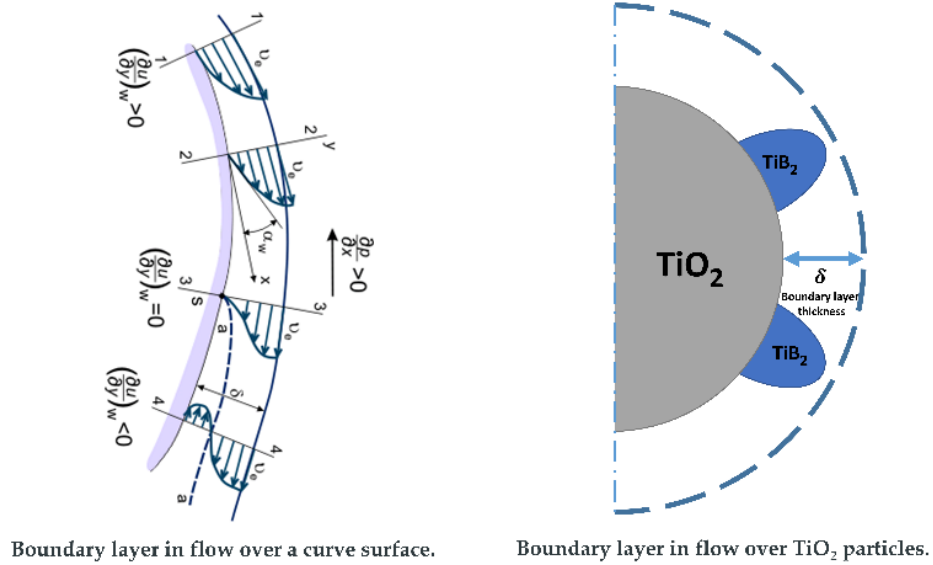


Figure 53 Schematic representation of the boundary layer on TiO_2 particles during stir mixing and turbulent flow effect on the detachment of TiB_2 nanoparticles during mixing.

According to Newton's law of viscosity, liquid metal viscosity must obey the Arrhenius behavior as a function of temperature. In general the viscosity-temperature relation for liquid aluminum can be expressed in the form of:

$$\eta = \eta_0 \exp\left(\frac{E}{RT}\right)$$

where E is the activation energy for viscous flow, η_0 is the pre-exponential viscosity, which are both constants for the particular element, T is the temperature in K and R is the gas constant. Empirical results show that for liquid aluminum $\eta_0 = 0.257$ mPa.s and $E = 13.08$ kJ/mol [144]. Figure 54 shows the variation of experimental data obtained for aluminum melt viscosity by temperature in the range where our experimental results are obtained.

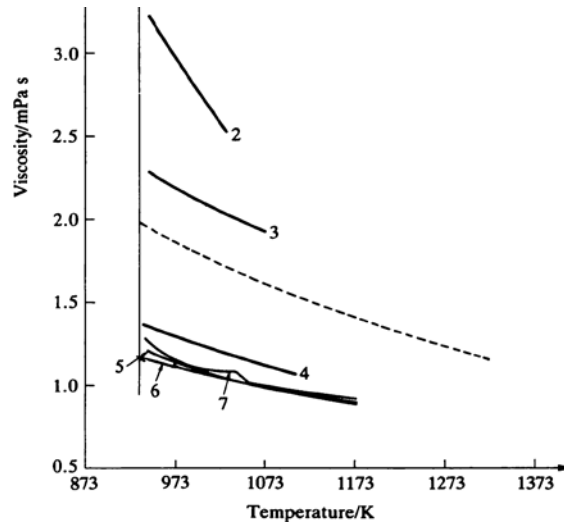


Figure 54 The variation of experimental data obtained for the aluminum melt viscosity with temperature [144]

Figure 55 shows the experimental data collected for the variation in refinement ratio by temperature at various mixing times. Figure 56 shows the fitted curves of the experimental data collected and shows that the change in grain size can be well described as the square root of viscosity at any specific temperature. Figure 57 shows the variation of refinement ratio with time. At higher temperatures, not only is the melt viscosity is decreasing, but also the size of nodules gets larger in smaller amount of time, and it will reach the detachment stress sooner. However, it can be clearly seen that the grain size ratio does not change significantly with mixing time. Figure 58 shows the 3D plot of variation in grain ratio by temperature and time. The isotherms can clearly illustrate the variation in grain size of MMNCs processed at similar temperatures.

$$\frac{D_{m,T}}{D_{0,T}} \propto \delta \propto \mu^{\frac{1}{2}} \propto \sqrt{\mu_0 e^{\frac{E}{RT}}}$$

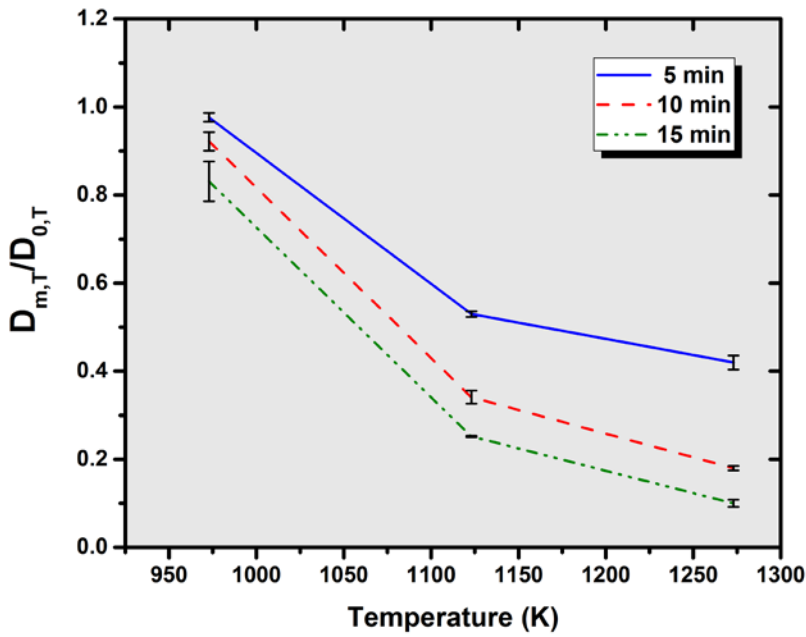


Figure 55 The experimental data collected for the variation in refinement ratio with pouring temperature at various mixing times for the nanocomposite reinforced with 4wt% hybrid particles

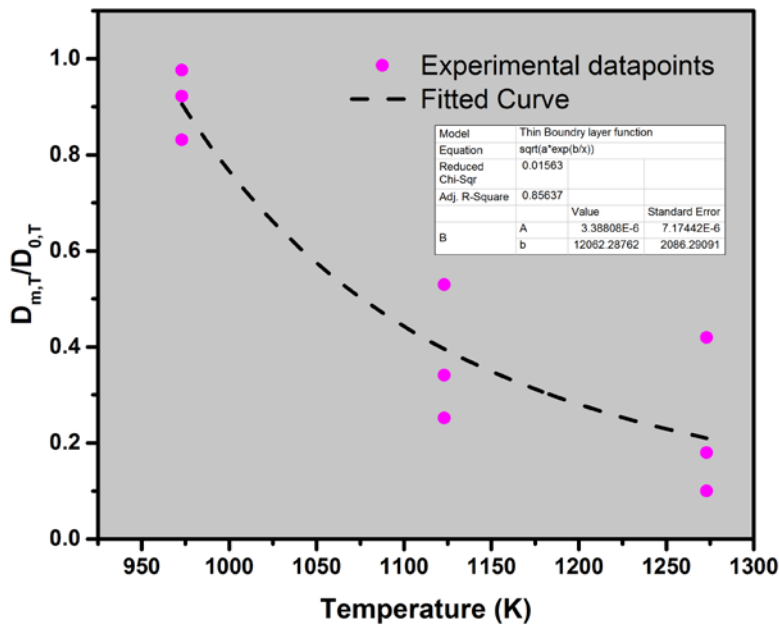


Figure 56 Variation in refinement ratio by temperature for the nanocomposites reinforced with 4wt% hybrid particles; the fitted curves of the experimental data is in accordance with the viscosity control prediction model

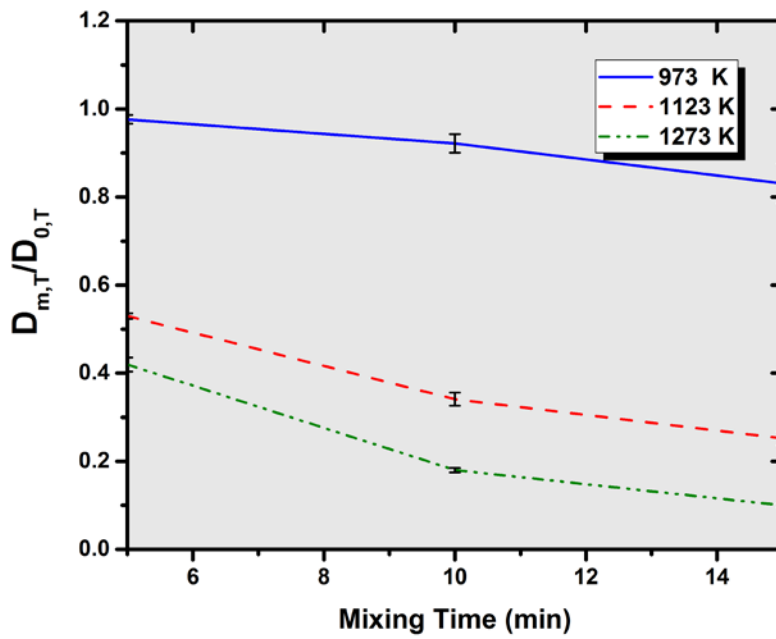


Figure 57 The experimental data collected for the variation in refinement ratio by mixing times at various temperatures for the nanocomposites reinforced with 4wt% hybrid particles

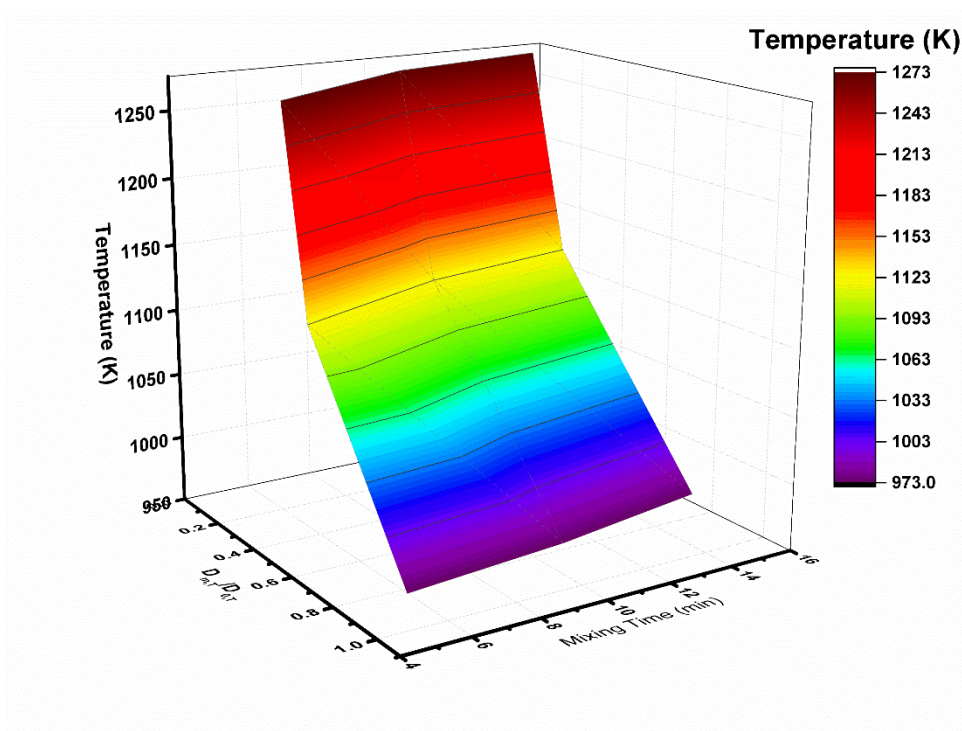


Figure 58 The 3D plot of variation in grain ratio by temperature and time for the nanocomposites reinforced with 4wt% hybrid particles.

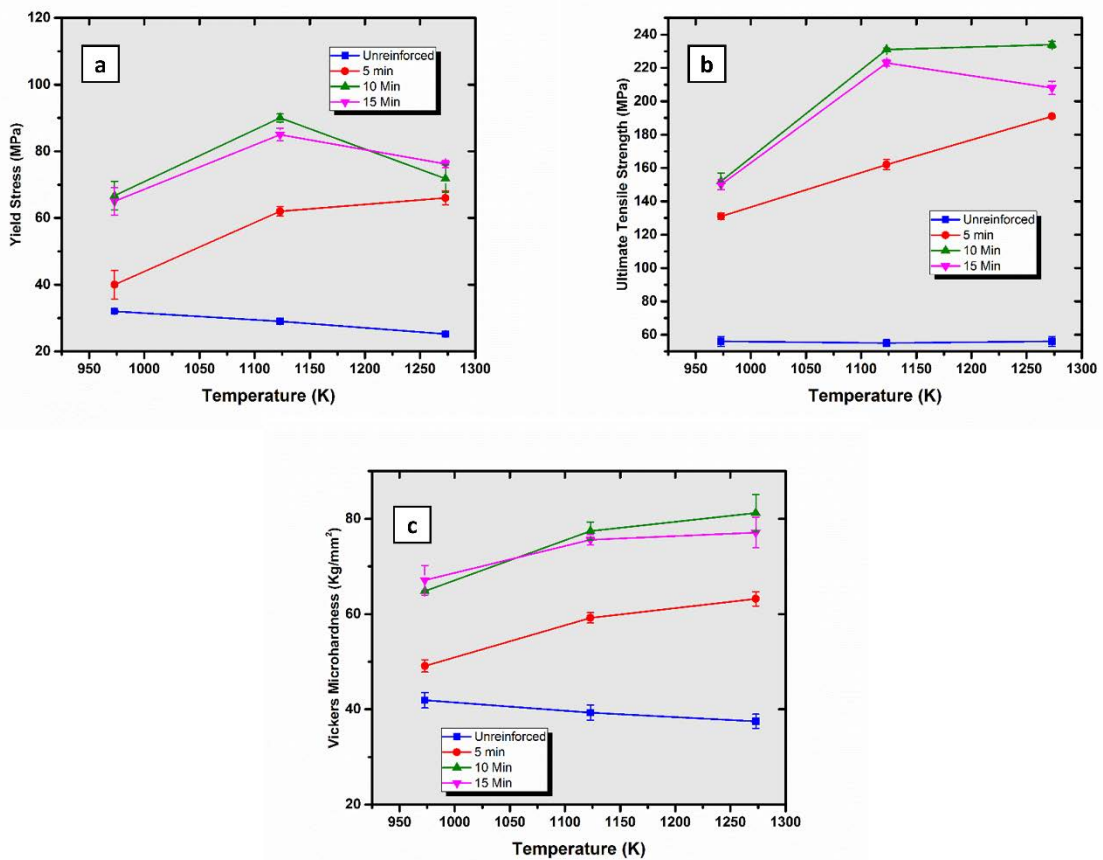


Figure 59 Variation in a) Hardness and, b) Yield Stress of the nanocomposites by processing temperature for 4wt% particle loading

Figure 59 displays the variation in hardness, yield stress, and ultimate tensile strength of the nanocomposites with 4wt% particle loading synthesized at different processing temperatures. The results show that by increasing processing temperature and time, the tensile properties can be affected. Based on the results, increasing the temperatures higher than 850 °C, no significant improvements can be obtained. In addition, at extended mixing times at 1000 °C where the melt viscosity is low, the re-agglomeration is likely to happen which deteriorates the mechanical properties. These mechanical properties of the in-situ nanocomposites synthesized at various processing conditions, Mechanical properties including hardness, yield strength, and ultimate

tensile strength is mainly controlled by matrix grain size, reinforcing particle size and type, and the reinforcing particle distribution. Variation in processing condition of the in-situ nanocomposites will change these factors which can be attributed to the multiple effects of factors which can increase or decrease the mechanical strength and ductility.

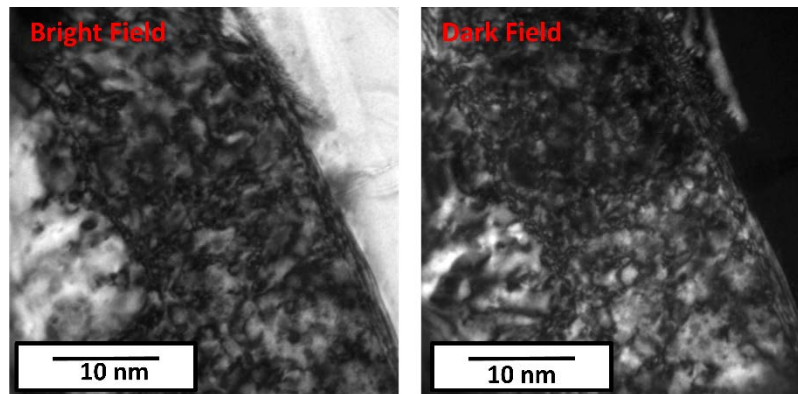


Figure 60 TEM image of dislocations around particles

As it has been discussed earlier in this section, the time and the temperature varies the MMNCs grain size. The addition of NPs to a metal matrix acts to refine the grain size by restricting the size of the grains which will lead to increased strength and hardness. It has been theoretically discussed and experimentally shown (Figure 58) that the change in grain refining ability of particles is changing with temperature similar to variation of viscosity with temperature as per Arrhenius law.

The thermal mismatch stress between reinforcements and aluminum matrix will increase the dislocation density within the matrix, which might lead to local stress and also increase the strength of the matrix, and thus that of the composite. This stress depends on the temperature from which the composite is cooled and the cooling rate. The higher the casting temperature, the more local stress will be present, increasing the strength of the composite (Figure 60).

Higher casting temperatures increase the fluidity of molten aluminum which will affect particle distribution in the samples. The improvement in the distribution the reinforcement can be a result of the high shear rate and the high intensity of turbulence which leads to the uniform dispersion of the reinforcement by breaking up the clusters. The apparent viscosity increases as temperature decreases, which in turn increases the shear stress. The force due to shear on the clusters, is linearly proportional to the melt viscosity and the shear rate. An increased shear stress breaks up the agglomerates and disperses particles more uniformly.

4.3.6 Variation of tribological properties with processing parameters [145]

In the present investigation, an aluminum/(Al₂O₃- TiB₂) metal matrix composite was fabricated by using the liquid metallurgy technique. The Transmission Electron Microscopy (TEM) study was conducted in order to investigate the microstructure of the in-situ processed composites. X-ray diffraction (XRD) analysis of the composite was performed to investigate the various phases present in the composite. Dry sliding tests were conducted using pin-on-disk tribometer in order to understand the self-lubricating behavior of developed composite. The microstructural characteristics revealed formation of in-situ phases and uniform dispersion of the reinforcement phases throughout the composite. The developed hybrid self-lubricating nanocomposites showed superior mechanical and tribological properties. The superior tribological properties of the hybrid composite are attributed to the formation and synergetic effect of TiB₂ and Al₂O₃ particles in the composites. The Al₂O₃ hard ceramic particles act as the obstacles to the movement of dislocation and thus enhance the mechanical properties. The oxidation of TiB₂ on the surface forms H₃BO₃ and TiO₂ tribo-layer resulting in superior tribological properties.

Results show that the composite hardness, strength, and ductility are changed by processing temperature and time since they influence the completion of the reaction, as well as the temperature required to affect desired reaction products. When the mixing time is not sufficient at a specific temperature, the reaction stops well before completion. On the other hand, while the mixing time is beyond optimal values, particle coarsening and particle growth can occur.

Figure 61 presents the variation of coefficient of friction (COF) of pure aluminum and aluminum composite at different reaction temperatures and times. It is interesting to note that the nanocomposites have a lower COF compared to pure aluminum which can be resulted from the self-lubrication nature of TiB_2 . Moreover, the COF values remain almost constant at different processing conditions which implies that the COF is not significantly dependent on processing conditions. The oxidation of TiB_2 during sliding process could be the most possible mechanism for reduced COF in nanocomposites compared to pure alloy. The existence of a soft film with nanometer thickness of the TiB_2 on the surface will lead to formation of H_3BO_3 film (Figure 62) [146]. During the sliding process of Al/ (Al_2O_3 - TiB_2) nanocomposite, the hard alumina phase can support the aluminum matrix and ultimately wears away from the surface of the composites. Some detached TiB_2 nanoparticles, left on the nanocomposites surface, are oxidized to TiO_2 and B_2O_3 followed by the formation of H_3BO_3 through reaction with H_2O from the air. Therefore, aluminum nanocomposite reinforced by nano TiB_2 shows a self-lubricating behavior. The fairly independent COF values as regards to the processing conditions indicate that the hardness does not play a significant effect on the COF of nanocomposites. This implies that the formation of lubricious tribo-layer is found to be more effective than the microstructural and hardness variation on frictional behavior.

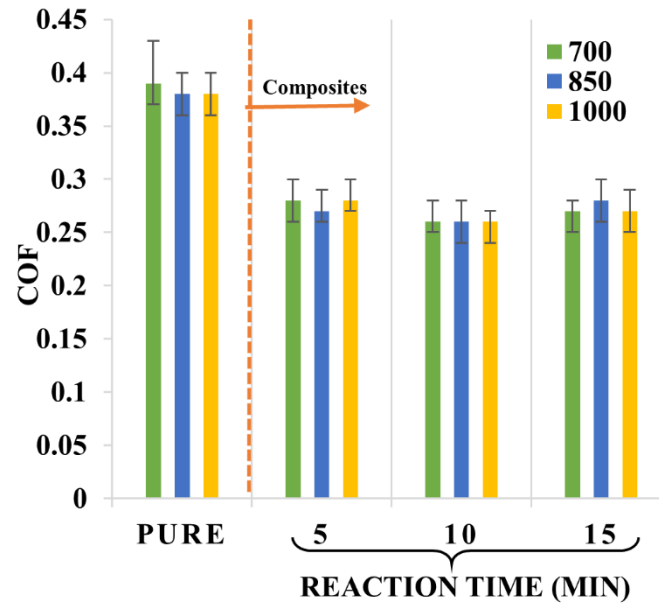


Figure 61 Variation of coefficient of friction of pure aluminum and nanocomposites reinforced with 4wt% hybrid particles synthesized at various processing conditions

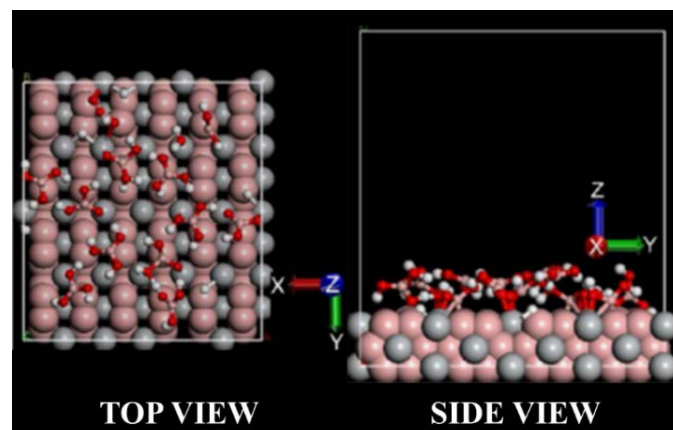


Figure 62 Lubricant tribofilm formation on worn surface of composites [146]

The wear results are shown in Figure 63, where the self-lubricating aluminum nanocomposites reinforced by TiB_2 and Al_2O_3 display lower wear rate values as compared to pure aluminum. Three important mechanisms are attributed to lower the values of wear rates in the composites: 1) higher hardness of the composites compared to pure aluminum, 2) TiB_2 reaction with moisture in the air and formation of lubricious tribofilm on the worn surfaces, and 3) the load bearing effect of ceramic hard nanoparticles which protects the matrix from direct application of load. Generally, the synergetic effect of Al_2O_3 and TiB_2 , where the hardness imparted by the Al_2O_3

reinforcement particles, and the lubricious effect provided by the self-lubricating nature of TiB₂ reduce the severity of the wear on the surface, resulting in low volume loss during sliding.

Figure 63 shows the correlation between hardness and wear rate at different reaction temperatures and times. According to Archard equation, the wear rate is inversely proportional to hardness[147]. The sliding wear due to abrasion was given as:

$$V = \frac{kPL}{H}$$

where V is the volume loss, P is the applied load, L is the sliding distance, H is the hardness of the specimen, and k is the wear coefficient.

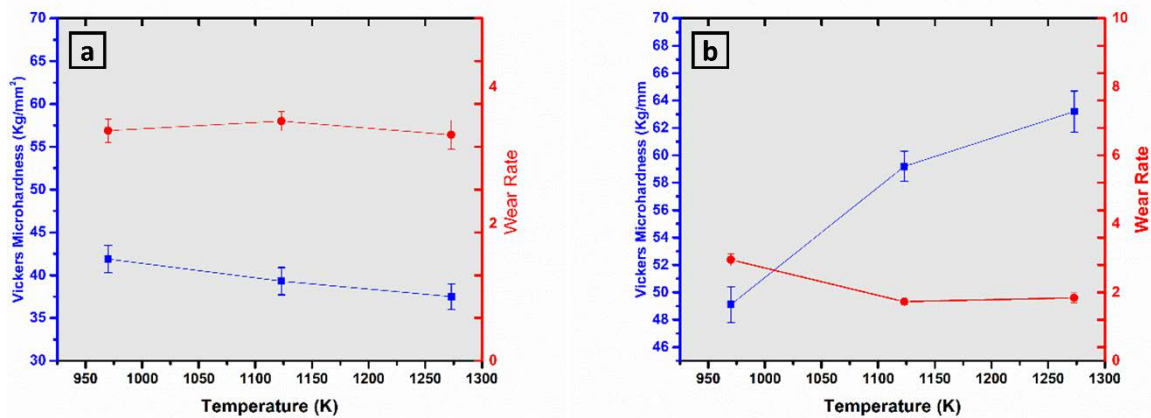


Figure 63 Variation of wear rate and hardness with reaction temperature for a) Unreinforced aluminum, b) nanocomposites reinforced with 4wt% hybrid particles

Microstructure characterization of worn surface of metal matrix nanocomposites is more complex than that of metals or alloys and an understanding of the wear mechanisms is far from complete. The SEM analysis of worn surface was carried out to illustrate the wear mechanisms in the nanocomposites in the presence of TiB₂ and Al₂O₃. The low magnification SEM micrographs of the aluminum and nanocomposites

are shown in Figure 64. The depth and number of grooves on the worn surface of the composites are decreased with the introduction of nanoparticles into the matrix in comparison with pure aluminum as shown in Figure 64. Smoother surface on the composites is due to the fact that the major part of applied load is carried by alumina nanoparticles which minimized the amount of plastic deformation and aid to the formation of lubricant film on the surface of composites. In addition, there are interactions between dislocations and Al_2O_3 nanoparticles that ultimately resist the propagation of cracks during sliding wear. Furthermore, during the solidification stage, strain fields are created around Al_2O_3 nanoparticles due to the thermal mismatch between the aluminum and Al_2O_3 nano-particle. The strain fields resist the propagation of the cracks and subsequent material removal during sliding condition. Moreover, the lubricant H_3BO_3 tribo-layer can reduce the actual area of metal to metal contact. These can be some of the reasons which lead to decrease in the wear rate of the composites containing TiB_2 and Al_2O_3 phases. The in-situ processing used in this study helps the particle's surface to remain clean, as a result, a good bonding between particles and aluminum matrix arise. Consequently, the impurity free interface and the good bonding delay the detachment of particles from the aluminum matrix. In general, the worn surface of the pure aluminum reveals patches of severely damaged regions and deep abrasion grooves caused by severe plastic deformation. The morphological examinations of the worn surfaces indicate the existence of both abrasion and delamination wear mechanisms.

Figure 65 illustrates the 2-D and 3-D profiles of the worn surfaces of pure aluminum and composites at 850 °C reaction temperature for different reaction times. It can be seen that the aluminum worn surface possess large peaks and deep valleys while small peaks and shallow valleys are observed in the composite worn surfaces indicating that

the composite possesses smoother worn surfaces than the pure aluminum. The measured 2D arithmetic average surface roughness (R_a) of pure aluminum is $1.243 \pm 0.04 \mu\text{m}$ while the surface roughness of composites for 5, 10 and 15 minutes reaction times are $0.832 \pm 0.027 \mu\text{m}$, $0.831 \pm 0.109 \mu\text{m}$, and $0.879 \pm 0.060 \mu\text{m}$, respectively.

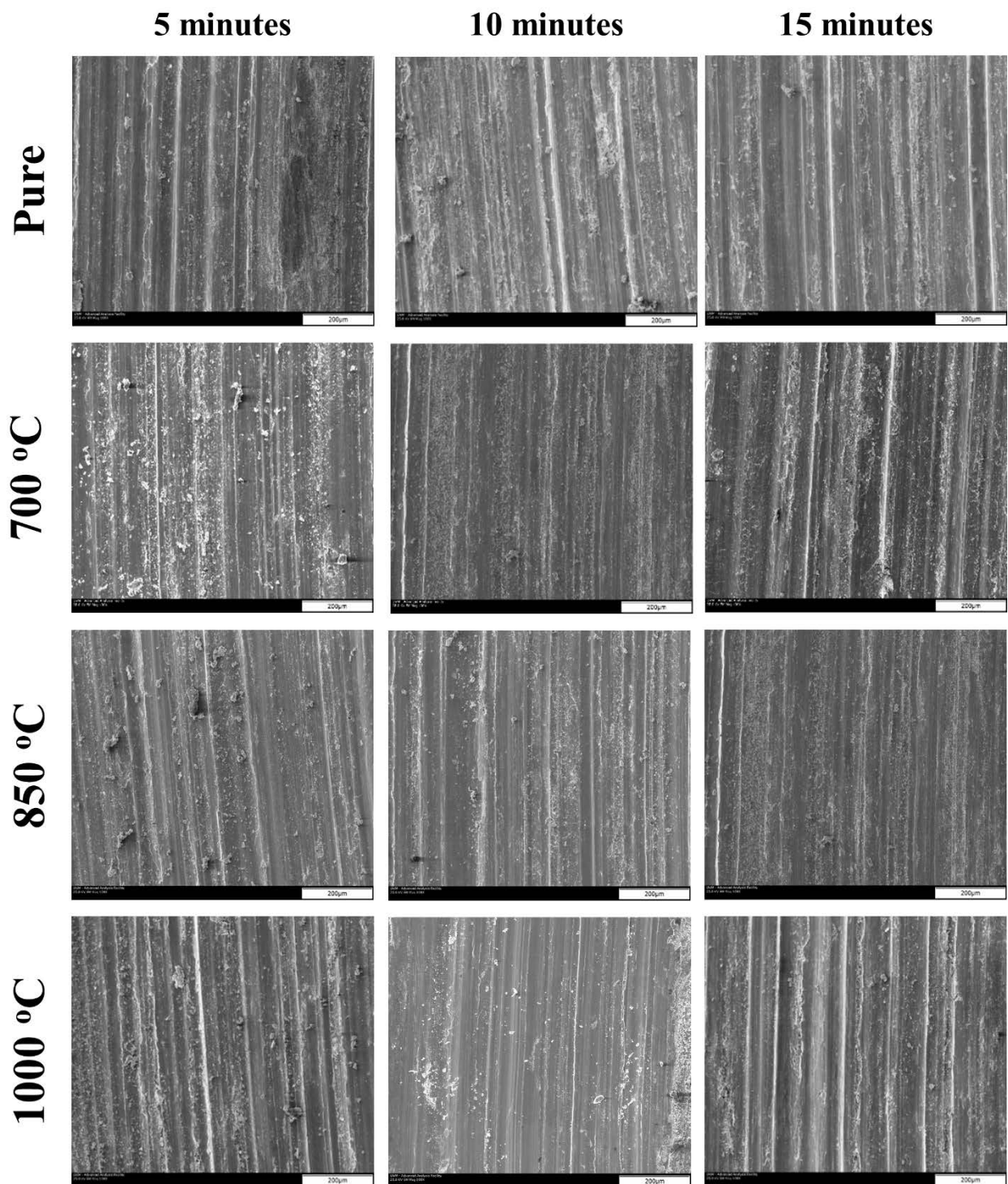


Figure 64 SEM micrographs of the worn surfaces at various processing times and temperatures

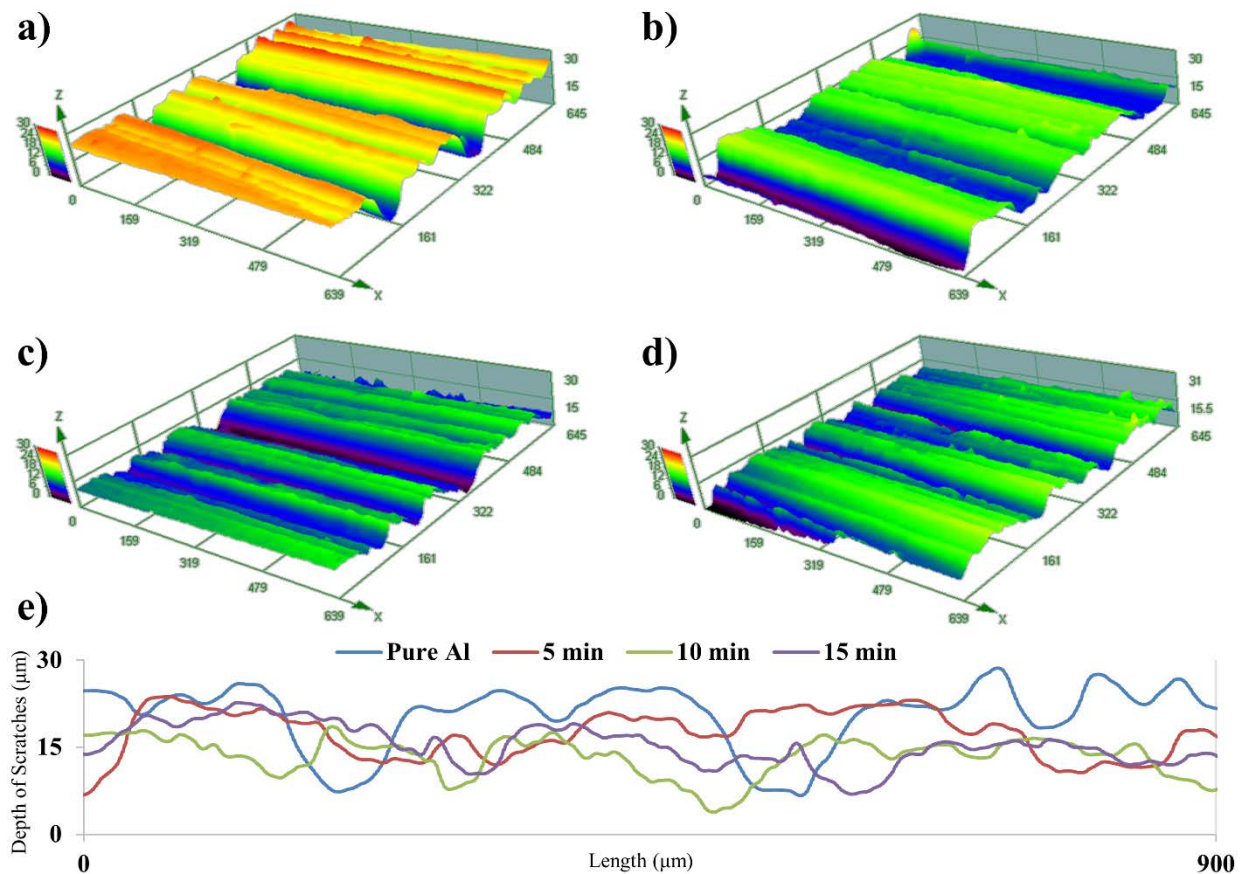


Figure 65 Topography image of worn surface for 850 °C reaction temperature for a) pure aluminum, b) 5 min, c) 10 min and d) 15 min reaction time and e) linear profile of worn surfaces

Figure 66 shows the EDS analysis of the worn surface after the sliding test. The main observation is that iron is transferred from the counterface to the composite by mechanical action. Simultaneous interactions between the hard particles that are present in the debris and the counterface material resulted in the micro plowing of fine iron rich regions. In addition, the composite surface showed presence of boron element which confirms that the worn surface is covered with boron layer, such as H_3BO_3 as it is indicated in Zhou's study [146]. In literature, boric acid is found as a good solid lubricants and showed superior tribological performance [148, 149]. However, they are forced out of the contact zone during sliding. To retain these solid lubricants at the interface, a carrier lubricant was used. Again, these additives when added in the carrier lubricant, a multiphase hybrid lubricant is developed and demonstrated a superior

tribological performance over the carrier lubricant without any solid lubricant additives. In the current research, when self-lubricating composites are used, such external lubricant is not required as the lubricant is forming in-situ during sliding and continuously replenished to the interface which ultimately results in superior tribological performance.

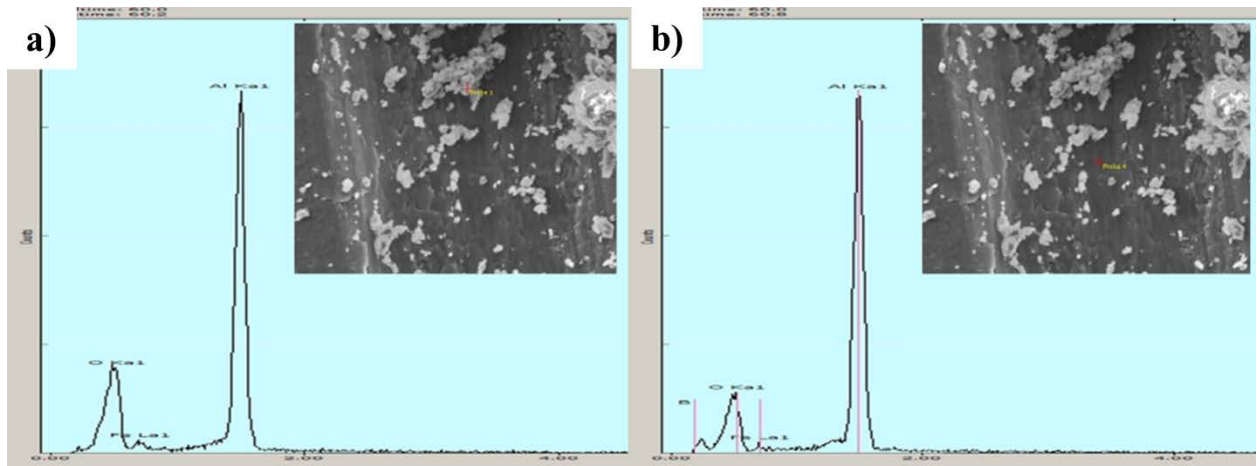


Figure 66 Energy dispersive spectrum (EDS) of the worn surface

4.3.7 Summary

Microstructures and mechanical properties of aluminum matrix composites reinforced by in-situ TiB_2 and Al_2O_3 particulates have been investigated. Result of XRD analysis indicates that the $(\text{Al}_2\text{O}_3 + \text{TiB}_2)$ /aluminum composites can be fabricated with the direct melt reaction method. According to reaction sequence TiB_2 and Al_2O_3 reinforcement particles forms in Al-B melts through the reaction on the surface of TiO_2 particles, where the size of the in-situ formed particles is controlled by the size of the TiO_2 particles. In this chapter it was experimentally demonstrated that TiB_2 and Al_2O_3 particles with sizes ranging from 5-55 μm can be formed in-situ from micronized TiO_2 particles while a nanocomposite can be prepared using nanosized TiO_2 particles. SAED by TEM is used to characterize crystal symmetry and lattice parameters.

An ultrasonic assisted processing were used to disperse nanoparticles within the matrix. The micro-structural analysis indicated the uniform distribution of nanoparticles in the aluminum matrix with few clusters of reinforcing particles. From the investigations on mechanical properties of composites, we deduce that the yield stress, UTS and hardness of composites are obviously higher than those of unreinforced with the same percentage reinforcements of TiB_2 or Al_2O_3 particles. Elimination of Al_3Ti brittle phase by using this processing route greatly improved the mechanical properties of the composites prepared compared to previous literatures. Additionally, nanocomposites shows improved tensile ductility in comparison with microcomposite. Crack propagation in the nanocomposites region is retarded by blunting mechanism of nanoparticles. Processing, structure and property relationships has been studied and it was found that the refining power of NPs which depends on their size is very dependent on processing temperature but not time. The size of NPs is controlled by viscosity of the melt rather than precipitation and growth. There was an improvement in tensile and yield strength accompanied by a factor of three but no significant loss in ductility in the nanocomposites. It has been shown while the higher mixing temperature can improve the tensile properties, but long mixing times will cause reagglomeration of particles which led to embrittlement and less interfacial bonding and so decrease in mechanical properties. The wear resistance of the composite has been compared with and found to be better than that of unreinforced alloy. The decreased wear rate of hybrid composite can be attributed to the simultaneous interaction of TiB_2 and Al_2O_3 particles for the formation of a more resistant tribolayer at the contact surface.

CHAPTER 5. CONCLUSION

The following conclusions have been drawn from the current work:

1. Thermodynamic calculations shows that, in Al-TiO₂-B system, the Gibbs free energy change for formation of TiB₂ is much more negative than those for other reactions in temperature range between 200- 1400 °C. Therefore, in presence of sufficient boron, TiB₂ phase is more thermodynamically stable compared to other intermetallics such as Al₃Ti and AlB₂.
2. The heat flow analysis of the Al-TiO₂-B mixture shows that when the mixture is heated up, an endothermic peak at 676 °C, which corresponds to the melting of the 99% pure aluminum, followed an endothermic tempered valley at 759 °C, and an exothermic peak which onsets at 940 °C are observed.
3. XRD results suggest that the reduction of TiO₂ by boron and aluminum is more complicated than depicted by direct reduction which only shows the formation of the thermodynamically stable phases.
4. The X-ray diffraction patterns obtained on products heat treated below the exothermic peak on DSC trace (676 °C) for up to 30 minutes suggests that no significant reaction between Al, B, and TiO₂ have occurred.
5. The X-ray diffraction patterns after thermal processing at 760°C held isothermally for longer 30 minutes show that the anatase TiO₂ begins to transform to rutile- TiO₂. Microstructural analysis shows that the Rutile surface is highly hierarchical with clusters of fine nano-sized TiO₂ crystals aggregated in a spheroidal morphology (Stage I).

6. The X-ray diffraction pattern after thermal processing at 900 °C with no holding time, suggests that intermediate phases including TiBO_3 , Ti_2O_3 , and minor quantities of Al_2O_3 , and Al_3Ti have begun to appear (Stage II).
7. SEM and TEM observations and elemental analysis show the formation of a shell on TiO_2 particles consisting of Al_2O_3 spheroidal and Al_3Ti rod-like structure of several tens of nanometers at stage II.
8. Once the Al_2O_3 layer that forms is continuous, it prevents the liquid aluminum from coming into contact with the TiO_2 underneath in the core. The higher diffusivity of boron in Al_2O_3 rather than aluminum diffusivity, let the TiO_2 in the core reacts with B to form TiBO_3 and Ti_2O_3 as intermediates through a partial reduction.
9. X-ray diffraction pattern of the mixture isothermally treated for 5 minutes at 900 °C, suggests that the borothermic reduction proceeds and the two phases formed at stage I (TiBO_3 and Ti_2O_3) are reacting with boron to form TiB_2 and B_2O_3 (Stage III).
10. Although partial reduction of TiO_2 by aluminum was started at Stage II, the XRD analysis shows that the formation of the TiB_2 is associated with a decrease in the intensity of the main TiBO_3 and Ti_2O_3 peaks but little change to the Al_2O_3 and Al_3Ti peaks at stage III.
11. Theoretical calculation shows that Formation of TiB_2 is accompanied by 156% volume change which will result in formation of cracks on Al_2O_3 / Al_3Ti shell and direct contact between molten aluminum and TiO_2 (Stage IV). Aluminothermic reduction of the remaining TiO_2 proceeds by formation of Magne ´li phases.

12. At the final stage of transformation (Stage V), the complete reduction of TiO_2 and dissolution of Al_3Ti allows only Al_2O_3 and TiB_2 to phases exist as a reaction product.
13. Experimental observations suggest that using nanosized TiO_2 powder as precursor is a viable process capable of resulting in the synthesis of nano Al_2O_3 and TiB_2 as reinforcement particles inside an aluminum matrix by aluminoborthermic reduction.
14. HRTEM studies shows that when TiO_2 particles with 25 nm average size is used as a precursor in the Al- TiO_2 - B mixture, the particle size of final products is in range of 5-55 nm, while, TiB_2 and Al_2O_3 particles with sizes ranging from 20-45 μm can be formed in-situ from micronized TiO_2 particles (>44 μm).
15. In-situ formation of hybrid Al/(Al_2O_3 - TiB_2) during melt processing of aluminum alloys can be considered as a practical method for producing metal matrix nanocomposites, which may be scaled-up to make larger parts and or ingots.
16. A hybrid Al/(Al_2O_3 - TiB_2) composite has been synthesized using micronized TiO_2 particles (25 μm average particle size, >44 μm). TiB_2 and Al_2O_3 particles with sizes ranging from 5-55 μm can be formed by in-situ reaction during melt processing. Few particulates having a size less than 100 nm have been observed. TiB_2 is a block-like particulate and has straight sides while Al_2O_3 was an approximately spherical particulate.
17. XRD analysis of the powders skimmed from bottom and top of the melt before pouring suggests that unreacted TiO_2 is present when micronized TiO_2 particles have been used as a precursor. Theoretical calculations shows that the

reaction sites can be increased three times in magnitude by introducing nano size particles in the melt.

18. A hybrid Al/(Al₂O₃-TiB₂) composite has been synthesized using nanosized TiO₂ particles (25 nm average particle size). TiB₂ and Al₂O₃ particles with sizes ranging from 5-100 nm can be formed by using an in-situ melt processing. No particulates having a size larger than 150 nm have been observed. However agglomeration and particle capture by solidification front is an issue that has not completely been resolved.
19. Theoretical calculations and experimental analysis showed that mechanical stir mixing is not sufficient to deagglomerate the nanoparticle clusters. However, collapse of cavitation bubbles forms on the surface of a particle during ultrasonic mixing lead to shock waves which can potentially break the particle apart. TEM observation confirms the uniform distribution of particles in the matrix with few clusters of reinforcing particles.
20. The mechanical properties of the composites synthesized by in-situ reactive stir mixing were improved relative to the base alloy. The ultimate tensile strength of microcomposites has been improved at optimum processing condition approximately by 40% with significant decrease in ductility, while in the nanocomposite, 250% improvement in UTS has been measured with no significant loss in ductility.
21. Fractography studies shows that fine dimples are present in fracture surface of nanocomposites, while in the composites synthesized by micron sized TiO₂ mixed type fracture including failing across the shear planes and fracture ridges were observed.

22. Nano indentation and hardness analysis showed that by increasing the volume percentage of nanoparticles in the in-situ composite, the modulus increases from 63 GPa in unreinforced aluminum to 72 GPa for 8 wt% particle reinforced nanocomposites. Increasing the nano particle content above 4 wt% is not lead to improved hardness which may be attributed to the nanoparticles distribution within the matrix. By adding 4 Wt% of reinforcement to the matrix the hardness has increased from 0.94 GPa to 1.14 GPa.
23. The grain size is increasing linearly with increasing temperature in unreinforced aluminum. However, after addition of NPs the grain size of the matrix is decreasing by pouring temperature. It was found that the refining power of NPs which depends on their size is very dependent on processing temperature but not significantly on time.
24. Increasing temperature and time improves the tensile properties. At 1000 °C where the melt viscosity in very high, extended mixing times is likely to result in the re-agglomeration which deteriorate the mechanical properties. The maximum ultimate tensile strength obtained at the optimum processing condition of composites relative to the base aluminum has been increased from 56 MPa to 232 MPa.
25. Tribological studies shows that the fabricated hybrid self-lubricating nanocomposites have shown better wear properties compared to the base metal. The decreased wear rate of hybrid composite is likely to be attributed to the simultaneous interaction of TiB₂ and Al₂O₃ particles in the formation of a more resistant tribolayer on the contact surface.

CHAPTER 6. FUTURE WORK

The objective of this dissertation was to explore the feasibility and the processing pathway for the bulk synthesis of metal matrix composites using in-situ ultrasonic assisted stir mixing through a careful investigation of the particle formation mechanism. Although preliminary information was obtained regarding the microstructure, properties, and the processing conditions for in-situ processed nanocomposites, future work will focus on TEM and SEM investigation to show how the nanoparticles are distributed along and within the grain boundaries at different processing condition. Also, more characterization is required to identify the Al_2O_3 / TiB_2 particles by EBSD and lattice imaging.

In addition, to have a uniform distribution of reinforcement particles in metal-matrix composites synthesized from solidification processing, the particle pushing and engulfment by the moving solidification front is important to be studied. Theoretical studies shows that TiB_2 particles have a high tendency to be captured by solidification front. Experimental studies is required to investigation the variation in cooling rate and the particle size and content on their engulfment. The use of this technique to synthesize master alloys for subsequent re-melting and dispersion in a larger melt can be explored.

In addition a theoretical and experimental investigation is required to model the mechanical properties' improvement in the synthesized MMNCs. Future work will also focus on the effect of stirring parameter and ultrasonic intensity on microstructure and mechanical properties of the nanocomposites. Moreover, the reaction pattern can be extended for other lightweight materials such as magnesium and fabrication magnesium nanocomposites.

Future work will also focus on alloy selection so that higher mechanical properties can be obtained. Synthesize the nanocomposites with aluminum alloys with higher initial mechanical properties such A365 and A206 may lead to utilization of full potential of these materials. However, a careful study is required to investigate the possible reaction models of the reactant and the alloying elements.

Computational fluid dynamics analysis of the effect of flow of liquid metal during reactive mixing at different condition and the quantitative modeling of reaction and solidification will lead to a more systematic processing parameter selection which provides a benchmark for the development of metal matrix nanocomposites with improved microstructures and properties via stir mixing.

CHAPTER 7. REFERENCES

1. Moghadam, A.D., et al., *Functional metal matrix composites: self-lubricating, self-healing, and nanocomposites-an outlook*. JOM, 2014. **66**(6): p. 872-881.
2. Rohatgi, P.K., et al., *Synthesis and properties of metal matrix nanocomposites (MMNCS), syntactic foams, self lubricating and self-healing metals*. PRICM, 2013. **8**: p. 1515-1524.
3. Moghadam, A.D., et al., *Mechanical and tribological properties of self-lubricating metal matrix nanocomposites reinforced by carbon nanotubes (CNTs) and graphene—a review*. Composites Part B: Engineering, 2015. **77**: p. 402-420.
4. Doel, T. and P. Bowen, *Tensile properties of particulate-reinforced metal matrix composites*. Composites Part A: Applied Science and Manufacturing, 1996. **27**(8): p. 655-665.
5. Degischer, H.P., *Innovative light metals: metal matrix composites and foamed aluminium*. Materials & design, 1997. **18**(4): p. 221-226.
6. Tjong, S.C., *Novel Nanoparticle-Reinforced Metal Matrix Composites with Enhanced Mechanical Properties*. Advanced Engineering Materials, 2007. **9**(8).
7. Kumar, G.V., et al., *Studies on Al6061-SiC and Al7075-Al₂O₃ metal matrix composites*. Journal of Minerals and Materials Characterization and Engineering, 2010. **9**(01): p. 43.
8. Shen, Y.-L. and N. Chawla, *On the correlation between hardness and tensile strength in particle reinforced metal matrix composites*. Materials Science and Engineering: A, 2001. **297**(1): p. 44-47.
9. Davis, L. and B. Artz, *Thermal conductivity of metal-matrix composites*. Journal of applied physics, 1995. **77**(10): p. 4954-4960.
10. Vaidya, R.U. and K. Chawla, *Thermal expansion of metal-matrix composites*. Composites Science and Technology, 1994. **50**(1): p. 13-22.
11. Farley, G.L., *Energy absorption of composite materials*. Journal of composite Materials, 1983. **17**(3): p. 267-279.
12. Schaller, R., *Metal matrix composites, a smart choice for high damping materials*. Journal of Alloys and Compounds, 2003. **355**(1): p. 131-135.
13. Deve, H.E. and C. McCullough, *Continuous-fiber reinforced composites: A new generation*. Jom, 1995. **47**(7): p. 33-37.
14. Kevorkijan, V.M., *Aluminum Composites for Automotive Applications: A Global Perspective-II*. JOM, 1999: p. 54.
15. Ibrahim, I., F. Mohamed, and E. Lavernia, *Particulates reinforced metal matrix composites – a review*. Journal of Materials Science, 1991. **26**: p. 1137.
16. Jamaati, R., et al., *Effect of particle size on microstructure and mechanical properties of composites produced by ARB process*. Materials Science and Engineering: A, 2011. **528**(4): p. 2143-2148.
17. Barmouz, M., et al., *Investigation of mechanical properties of Cu/SiC composite fabricated by FSP: effect of SiC particles' size and volume fraction*. Materials Science and Engineering: A, 2011. **528**(3): p. 1740-1749.
18. Christy, T., N. Murugan, and S. Kumar, *A comparative study on the microstructures and mechanical properties of Al 6061 alloy and the MMC Al 6061/TiB₂/12p*. Journal of Minerals and Materials Characterization and Engineering, 2010. **9**(01): p. 57.
19. Karnezis, P., G. Durrant, and B. Cantor, *Characterization of reinforcement distribution in cast Al-alloy/SiC p composites*. Materials Characterization, 1998. **40**(2): p. 97-109.

20. Prabu, S.B., et al., *Influence of stirring speed and stirring time on distribution of particles in cast metal matrix composite*. Journal of Materials Processing Technology, 2006. **171**(2): p. 268-273.
21. Suresh, S., et al., *Production and characterization of micro and nano Al₂O₃ particle-reinforced LM25 aluminium alloy composites*. ARPN Journal of Engineering and Applied Sciences, 2011. **6**(6).
22. Ezatpour, H.R., et al., *Investigation of microstructure and mechanical properties of Al6061-nanocomposite fabricated by stir casting*. Materials & Design, 2014. **55**: p. 921-928.
23. Goh, C., et al., *Ductility improvement and fatigue studies in Mg-CNT nanocomposites*. Composites Science and Technology, 2008. **68**(6): p. 1432-1439.
24. Hassan, S. and M. Gupta, *Development of high performance magnesium nanocomposites using nano-Al₂O₃ as reinforcement*. Materials Science and Engineering: A, 2005. **392**(1): p. 163-168.
25. Hassan, S. and M. Gupta, *Development of nano-Y₂O₃ containing magnesium nanocomposites using solidification processing*. Journal of Alloys and Compounds, 2007. **429**(1): p. 176-183.
26. Nouri, N., *Water withdrawal and consumption reduction analysis for electrical energy generation system*. 2015.
27. Li, X., Y. Yang, and X. Cheng, *Ultrasonic-assisted fabrication of metal matrix nanocomposites*. Journal of Materials Science, 2004. **39**(9): p. 3211-3212.
28. Yang, Y., J. Lan, and X. Li, *Study on bulk aluminum matrix nano-composite fabricated by ultrasonic dispersion of nano-sized SiC particles in molten aluminum alloy*. Materials Science and Engineering: A, 2004. **380**(1): p. 378-383.
29. Ferguson, J., et al., *On the strength and strain to failure in particle-reinforced magnesium metal-matrix nanocomposites (Mg MMNCs)*. Materials Science and Engineering: A, 2012. **558**: p. 193-204.
30. Kim, C.-S., et al., *Prediction models for the yield strength of particle-reinforced unimodal pure magnesium (Mg) metal matrix nanocomposites*. Journal of Materials Science, 2013. **48**(12): p. 4191.
31. Ferguson, J., et al., *Revised Orowan Strengthening: Effective Interparticle Spacing and Strain Field Considerations*. Metallurgical and Materials Transactions A, 2012. **43**(6): p. 2110-2115.
32. Xu, J., et al., *Theoretical study and pathways for nanoparticle capture during solidification of metal melt*. Journal of Physics: Condensed Matter, 2012. **24**(25): p. 255304.
33. Miracle, D., *Metal matrix composites—from science to technological significance*. Composites science and technology, 2005. **65**(15): p. 2526-2540.
34. Rawal, S.P., *Metal-matrix composites for space applications*. JOM, 2001. **53**(4): p. 14-17.
35. Rohatgi, P., *Cast aluminum-matrix composites for automotive applications*. Jom, 1991. **43**(4): p. 10-15.
36. Chen, L.-Y., et al., *Achieving uniform distribution and dispersion of a high percentage of nanoparticles in metal matrix nanocomposites by solidification processing*. Scripta Materialia, 2013. **69**(8): p. 634-637.
37. He, F., Q. Han, and M.J. Jackson, *Nanoparticulate reinforced metal matrix nanocomposites—a review*. International Journal of Nanoparticles, 2008. **1**(4): p. 301.
38. Casati, R. and M. Vedani, *Metal matrix composites reinforced by nano-particles—a review*. Metals, 2014. **4**(1): p. 65-83.

39. Zhang, Z. and D.L. Chen, *strength, Consideration of Orowan strengthening effect in particulate-reinforced metal matrix nanocomposites: A model for predicting their yield*. Scripta Materialia, 2006. **54**: p. 1321.
40. Ajayan, P.M., L.S. Schadler, and P.V. Braun, *Nanocomposite science and technology*. 2006: John Wiley & Sons.
41. Ghosh, S.K., P. Saha, and S. Kishore, *Influence of size and volume fraction of SiC particulates on properties of ex situ reinforced Al–4.5 Cu–3Mg metal matrix composite prepared by direct metal laser sintering process*. Materials Science and Engineering: A, 2010. **527**(18): p. 4694-4701.
42. Ni, D., et al., *Effect of B 4 C particle size on microstructure of in situ titanium matrix composites prepared by reactive processing of Ti–B 4 C system*. Scripta materialia, 2006. **55**(5): p. 429-432.
43. Dolatkhah, A., et al., *Investigating effects of process parameters on microstructural and mechanical properties of Al5052/SiC metal matrix composite fabricated via friction stir processing*. Materials & Design, 2012. **37**: p. 458-464.
44. Ma, Z., et al., *In-situ formed Al₂O₃ and TiB₂ particulates mixture-reinforced aluminum composite*. Scripta Metallurgica et Materialia, 1994. **31**(5): p. 635.
45. Yue, N.L., L. Lu, and M.O. Lai, *Application of thermodynamic calculation in the in-situ process of Al/TiB₂*. Composite Structures, 1999. **47**: p. 691.
46. Zhu, H.X. and R. Abbaschian, *In-situ processing of NiAl–alumina composites by thermite reaction*. Materials Science and Engineering: A, 2000. **282**(1-2): p. 1.
47. Fan, T., G. Yang, and D. Zhang, *Thermodynamic Effect of Alloying Addition on In-Situ Reinforced TiB₂/Al Composites*. METALLURGICAL AND MATERIALS TRANSACTIONS A, 2005. **36A**: p. 225.
48. Dong, S. and T. Yang, *Thermodynamic analysis of the formation of In-situ reinforced phases in cast Al-4.5 Cu alloy*. Journal of Wuhan University of Technology-Mater. Sci. Ed., 2008. **23**(3): p. 342-345.
49. MALEKI, A., et al., *Synthesis of In-situ Aluminum Matrix Composite Using a New Activated Powder Injection Method*. Metallurgical and Materials Transactions A, 2008. **39A**: p. 3034.
50. Sudarshan, M.K., D.A. Surappa, and R. Raj, *Nanoceramic–Metal Matrix Composites by In-Situ Pyrolysis of Organic Precursors in a Liquid Melt*. Metallurgical and Materials Transactions A, 2008. **39A**: p. 3291.
51. Jing, Z., et al., *Al-Si/Al₂O₃ in situ composite prepared by displacement reaction of CuO/Al system*. Research & Development, 2010. **7**(1): p. 19.
52. Liu, Z., et al., *Effect of ultrasonic vibration on microstructural evolution of the reinforcements and degassing of in situ TiB₂p/Al–12Si–4Cu composites*. Journal of Materials Processing Technology, 2012. **212**(2): p. 365-371.
53. Niranjana, K. and P. Lakshminarayanan, *Dry sliding wear behaviour of in situ Al–TiB₂ composites*. Materials & Design, 2013. **47**: p. 167-173.
54. Senthil, P., T. Selvaraj, and K. Sivaprasad, *Influence of turning parameters on the machinability of homogenized Al–Cu/TiB₂ in situ metal matrix composites*. The International Journal of Advanced Manufacturing Technology, 2013. **67**(5-8): p. 1589-1596.
55. Eskandari, H. and R. Taheri, *A Novel Technique for Development of Aluminum Alloy Matrix/TiB₂/Al₂O₃ Hybrid Surface Nanocomposite by Friction Stir Processing*. Procedia Materials Science, 2015. **11**: p. 503-508.
56. Balali, M.H., *An Economical Model Development for a Hybrid System of Grid Connected Solar PV and Electrical Storage System*. 2015.

57. Yoshikawa, N., et al., *Growth Rate and Microstructure of Al/Al₂O₃ Composite Body Obtained by Reaction between SiO₂ and Molten Al*. Journal of the Japan Institute of Metals, 1999. **63**(3): p. 312.
58. Munro, R.G., *Material properties of titanium diboride*. Journal of Research of the National Institute of Standards and Technology, 2000. **105**(5): p. 709-720.
59. Lü, L., et al., *In situ TiB₂ reinforced Al alloy composites*. Scripta Materialia, 2001. **45**(9): p. 1017-1023.
60. Kumar, N., et al., *Titanium diboride thin films by low-temperature chemical vapor deposition from the single source precursor Ti (BH₄)₃ (1, 2-dimethoxyethane)*. Chemistry of materials, 2007. **19**(15): p. 3802-3807.
61. Li, P., R. Zhou, and X.C. Zeng, *Computational Analysis of Stable Hard Structures in the Ti–B System*. ACS Applied Materials & Interfaces, 2015. **7**(28): p. 15607-15617.
62. Weirauch, D.A., *Technologically significant capillary phenomena in high-temperature materials processing: Examples drawn from the aluminum industry*. Current Opinion in Solid State and Materials Science, 2005. **9**(4): p. 230-240.
63. Mutale, C.T., W.J. Krafick, and D.A. Weirauch Jr, *Direct Observation of Wetting and Spreading of Molten Aluminum on TiB₂ in the Presence of a Molten Flux from the Aluminum Melting Point up to 1033 K (760 C)*. Metallurgical and Materials Transactions B, 2010. **41**(6): p. 1368-1374.
64. Asthana, R. and S. Tewari, *The engulfment of foreign particles by a freezing interface*. Journal of materials science, 1993. **28**(20): p. 5414-5425.
65. Han, Y., et al., *First-principles calculations on the stability of Al/TiB₂ interface*. Applied physics letters, 2006. **89**(14): p. 4107.
66. Weirauch Jr, D., et al., *The wettability of titanium diboride by molten aluminum drops*. Journal of materials science, 2005. **40**(9-10): p. 2301-2306.
67. Jiang, Z. and W.E. Rhine, *Preparation of titanium diboride from titanium alkoxides and boron powder*. Chemistry of materials, 1992. **4**(3): p. 497-500.
68. Vinod Kumar, G., B. Murty, and M. Chakraborty, *Settling behaviour of TiAl₃, TiB₂, TiC and AlB₂ particles in liquid Al during grain refinement*. International Journal of Cast Metals Research, 2010. **23**(4): p. 193-204.
69. Delannay, F., L. Froyen, and A. Deruyttere, *The wetting of solids by molten metals and its relation to the preparation of metal-matrix composites*. Journal of materials science, 1987. **22**(1): p. 1-16.
70. Neuhaus, S., N.D. Spencer, and C. Padeste, *Anisotropic wetting of microstructured surfaces as a function of surface chemistry*. ACS applied materials & interfaces, 2011. **4**(1): p. 123-130.
71. Estruga, M., et al., *Ultrasonic-Assisted Synthesis of Surface-Clean TiB₂ Nanoparticles and Their Improved Dispersion and Capture in Al-Matrix Nanocomposites*. ACS Applied Materials & Interfaces, 2013. **5**: p. 8813.
72. Hwang, Y. and J.K. Lee, *Preparation of TiB₂ powders by mechanical alloying*. Materials Letters, 2002. **54**(1): p. 1-7.
73. Li, P., et al., *Distribution of TiB₂ particles and its effect on the mechanical properties of A390 alloy*. Materials Science and Engineering: A, 2012. **546**: p. 146-152.
74. Abdellahi, M., M. Zakeri, and H. Bahmanpour, *Events and reaction mechanisms during the synthesis of an Al₂O₃-TiB₂ nanocomposite via high energy ball milling*. Frontiers of Chemical Science and Engineering, 2013. **7**(2): p. 123-129.
75. Takacs, L., *Self-sustaining reactions induced by ball milling*. Progress in Materials Science, 2002. **47**(4): p. 355-414.
76. Chen, Z.Y., et al., *Microstructure and properties of In situ Al/TiB₂ composite fabricated by in-melt reaction method*. 2000. **31**(8): p. 1959.

77. Emamy, M., M. Mahta, and J. Rasizadeh, *Formation of TiB₂ particles during dissolution of TiAl₃ in Al–TiB₂ metal matrix composite using an in situ technique*. Composites Science and Technology, 2006. **66**: p. 1063.
78. Thostenson, E.T. and T.W.C. C. Li, *Review: Nanocomposites in context*. Composites Science and Technology, 2005. **65**: p. 491.
79. Jackson, M.J., *Nanoparticulate reinforced metal matrix nanocomposites a review*. International journal of nanoparticles, 2009. **1**(4): p. 301.
80. Akbari, M.K., H. Baharvandi, and K. Shirvanimoghaddam, *Tensile and fracture behavior of nano/micro TiB₂ particle reinforced casting A356 aluminum alloy composites*. Materials & Design, 2015. **66**: p. 150-161.
81. Balali, M.H., et al. *Development of an economical model for a hybrid system of grid, PV and Energy Storage Systems*. in *2015 International Conference on Renewable Energy Research and Applications (ICRERA)*. 2015. IEEE.
82. Ferguson, J.B., et al., *On the superposition of strengthening mechanisms in dispersion strengthened alloys and metal matrix nano composites: Consideration of Stress and Energy*. Metals and Materials International, 2013: p. Accepted.
83. Flemings, M.C., *Metallurgical and Materials Transactions A*, (1991). **22A**: p. 957.
84. Maxwell, I. and A. Hellawell, *The constitution of the system Al-Ti-B with reference to aluminum-base alloys*. Metallurgical Transactions, 1972. **3**(6): p. 1487.
85. Easton, M. and D. StJohn, *Grain Refinement of Aluminum Alloys: Part I. The Nucleant and Solute Paradigms—A Review of the Literature*. Metallurgical and Materials Transactions A, 1999. **30A**: p. 1613.
86. Mohanthy, *mechanisms of grain refinement in aluminium alloys*. Acta Metallurgica et materialia, 1995. **43**: p. 2001.
87. StJohn and Easton, *Grain Refinement of Aluminum Alloys: Part II. Confirmation of, and a Mechanism for, the Solute Paradigm*. Metallurgical and Materials Transactions A, 1999. **30A**.
88. Cibula, A., *The mechanism of grain refinement of sand castings in aluminum alloys*. Journal of Inst Metals 1949. **1950.76**: p. 321.
89. Sigworth, G.K. and T.A. Kuhn, *Grain Refinement of Aluminum Casting Alloys*, in *ASM Handbook, Volume 15*. ASM Handbook, Volume 15: Casting. p. 255-262.
90. Wang, C., et al., *The grain refinement behavior of TiB₂ particles*. Materials Science and Engineering A, 2007. **459**: p. 238.
91. Kuruvilla, *Microstructure-property correlation in (XD) composite*. Scripta metallurgica et materialia, 1990: p. 873.
92. Lu, L., M.O. Lai, and H.Y. Wang, *Synthesis of titanium diboride TiB₂ and Ti-Al-B metal matrix composites*. Journal of Materials Science, 2000. **35**: p. 241.
93. Ma, Z.Y. and Tjong, *In Situ Ceramic Particle-Reinforced Aluminum Matrix Composites Fabricated by Reaction Pressing in the TiO₂ (Ti)-Al-B (B₂O₃) Systems*. METALLURGICAL AND MATERIALS TRANSACTIONS A, 1997. **28A**: p. 1931.
94. Chen, Y. and D.D.L. Chung, *In situ Al-TiB composite obtained by stir casting*. Journal of materials science, 1996. **31**: p. 311.
95. Feng, C.F. and L. Froyen, *Incorporation of All into TiB₂ in Al matrix composites and Al-Ti-B master alloys*. Materials Letters, 1997. **32**: p. 175.
96. Bartels, C., et al., *Investigation of the precipitation kinetics in an Al6061/TiB₂ metal matrix composite*. Materials Science and Engineering: A, 1997. **237**: p. 12.
97. Fjellstedt, J. and A.E.W. Jarfors, *On the precipitation of TiB₂ in aluminum melts from the reaction with KBF₄ and K₂TiF₆*. Materials Science and Engineering A, 2005. **413–414**: p. 527.

98. Lawrance, C. and P.S. Prabhu, *Al 6061-TiB₂ Metal Matrix Composite Synthesized with Different Reaction Holding Times by In-Situ Method*. International Journal of Composite Materials, 2015. **5**(5): p. 97-101.
99. Sureshkumar, T. and P.S. Kumar, *Fabrication and Characterization of Aa2024-Tib₂ Stir Casting Method*.
100. Chen, C.-G., et al., *Microstructural evolution and mechanical properties of in situ TiB₂/Al composites under high-intensity ultrasound*. Rare Metals, 2015. **34**(3): p. 168-172.
101. Gan, G.-S. and B. Yang, *Microstructure evolution of TiB₂ particle-reinforced 7075 Al alloy slurry in semisolid state with different holding time*. Rare Metals: p. 1-5.
102. Wood, J., P. Davies, and J.L.F. Kellie, *Properties of reactively cast aluminium-TiB₂ alloys*. Materials science and technology, 1993. **40**: p. 833.
103. Lakshmi, S., L. Lu, and M. Gupta, *In situ preparation of TiB₂ reinforced Al based composites*. Jopurnal of materials procesesing technology, 1998. **73**: p. 160.
104. Dhokey, N.B., et al., *Effect of KBF₄ and K₂TiF₆ on precipitation kinetics of TiB₂ in aluminium matrix composite*.
105. Chen, Z.Y., et al., *Microstructure and properties of In situ Al/TiB₂ composite fabricated by in-melt reaction method*. Metallurgical and Materials Transactions A, 2000. **31**(8): p. 1959-1964.
106. Chen, Z.Y., et al., *Solidification and interfacial structure of in situ Al-4.5Cu/TiB₂ composite*. Journal of Materials Science, 2000. **35**(22): p. 5605.
107. Donaldson, J.D., C.P. Squire, and F.E. Stokes, Journal of materials science, 1978: p. 13.
108. WANG, X., et al., *Microstructural analysis of Al alloys dispersed with TiB₂ particulate for MMC applications*. Journal of Microscopy, 1999. **196**: p. 137.
109. Wang, X., A. Jha, and R. Brydson, *In situ fabrication of Al₃Ti particle reinforced aluminium alloy metal matrix composites*. Materials science and engineering A, 2004. **364**: p. 339.
110. Usurelu, E.-M., et al., *On the Mechanism and Thermodynamics of the Precipitation of Tib₂ Particles in 6063 Matrix Aluminum Alloy*. U.P.B. Sci. Bull., Series B, 2011. **73**(3): p. 205.
111. Tee, K., L. Lu, and M. Lai, *In situ stir cast Al-TiB₂ composite: processing and mechanical properties*. Materials science and technology, 2001. **17**(2): p. 201-206.
112. Han, Y., X. Liu, and X. Bian, *In situ TiB₂ particulate reinforced near eutectic Al-Si alloy composites*. Composites Part A: Applied Science and Manufacturing, 2002. **33**(3): p. 439-444.
113. Tee, K.L., L. Lu, and M.O. Lai, *Synthesis of in situ Al-TiB₂ composites using stir cast route*. Composite Structures., 1999. **47**: p. 589.
114. Rajan, H.M., et al., *Synthesis and characterization of in situ formed titanium diboride particulate reinforced AA7075 aluminum alloy cast composites*. Materials & Design, 2013. **44**: p. 438-445.
115. Yuan, L., et al., *Mechanical properties and tribological behavior of aluminum matrix composites reinforced with in-situ AlB₂ particles*. Tribology International, 2016. **98**: p. 41-47.
116. Zhang, Y.-j., et al., *Microstructure and mechanical properties of in-situ TiB₂/A356 composites and a prediction model of yield strength*. China Foundry, 2015. **12**(4).
117. Tee, K.L., L. Lu, and M.O. Lai, *In situ processing of Al-TiB₂ composite by the stir-casting technique*. Journal of Materials Processing Technology, 1999. **89-90**: p. 513.

118. Yang, B., Y.Q. Wang, and B.L. Zhou, *The Mechanism of Formation of TiB₂ Particulates Prepared by In Situ Reaction in Molten Aluminum*. Metallurgical and Materials Transactions B, 1998. **29**: p. 635.
119. Emamy, M., M. Mahta, and J. Rasizadeh, *Formation of TiB₂ particles during dissolution of TiAl₃ in Al–TiB₂ metal matrix composite using an in situ technique*. Composites science and Technology, 2006. **66**(7): p. 1063-1066.
120. Gotman, I. and M.J. Koczak, *Fabrication of Al matrix in situ composites via self-propagating synthesis*. Materials science and engineering, 1994. **A187**: p. 189.
121. Ma, Z.Y., et al., *Property-microstructure correlation in in situ formed Al₂O₃, TiB₂ and Al₃Ti mixture-reinforced aluminium composites*. Journal of Materials Science, 1996. **31**: p. 741.
122. Garvin, J., Y. Yang, and H. Udaykumar, *Multiscale modeling of particle–solidification front dynamics. Part II: Pushing–engulfment transition*. International journal of heat and mass transfer, 2007. **50**(15): p. 2969-2980.
123. Estruga, M., et al., *Ultrasonic-assisted synthesis of surface-clean TiB₂ nanoparticles and their improved dispersion and capture in Al-matrix nanocomposites*. ACS applied materials & interfaces, 2013. **5**(17): p. 8813-8819.
124. Li, T., et al., *Particle Coagulation in Molten Metal Based on Three-Dimensional Analysis of Cluster by X-Ray Micro-Computer Tomography (CT)*. ISIJ international, 2013. **53**(11): p. 1958-1967.
125. KWON, Y.-S., *Microstructure changes in TiB₂-Cu nanocomposite under sintering*. JOURNAL OF MATERIALS SCIENCE, 2004. **39**: p. 5325.
126. Tu, J.P., et al., *Preparation and properties of TiB nanoparticle reinforced copper matrix composites by in situ processing*. Materials Letters, 2002. **52**: p. 448.
127. Guo, M.X., M.P. Wang, and K. Shen, *Synthesis of nano TiB₂ particles in copper matrix by in situ reaction of double-beam melts*. Journal of Alloys and Compounds, 2008. **460**: p. 585.
128. Bahmanpour, M. abdellahi, and M. Zakeri, *Events and reaction mechanisms during the synthesis of an Al₂O₃-TiB₂ nanocomposite via high energy ball milling*. Frontiers of Chemical Science and Engineering, 2013. **7**: p. 123.
129. Ramezani, M. and T. Neitzert, *Mechanical milling of aluminum powder using planetary ball milling process*. JAMME, 2012. **55**(2): p. 790-798.
130. Khaghani-Dehaghani, Ebrahimi-Kahrizangi, and Setoudeh, *Mechanochemical synthesis of Al₂O₃-TiB₂ nanocomposite powder from Al, H₃BO₃ and TiO₂ mixture*. International Journal of Refractory Metals and Hard Materials, 2011. **29**(2): p. 244.
131. Sharifi, Karimzadeh, and E. M, *Synthesis of titanium diboride reinforced alumina matrix nanocomposite by mechanochemical reaction of Al, B₂O₃ and TiO₂*. Journal of Alloys and Compounds, 2010. **502**(2): p. 508.
132. Welham, N.J., *Formation of Nanometric TiB₂ from TiO₂*. Journal of the American Ceramic Society, 2000. **83**(5): p. 1290.
133. Watson, I., et al., *Investigation of the clustering behaviour of titanium diboride particles in aluminium*. Composites Part A: Applied Science and Manufacturing, 2005. **36**(9): p. 1177-1187.
134. LI, X., Y. YANG, and X. CHENG, *Ultrasonic-assisted fabrication of metal matrix nanocomposites*. JOURNAL OF MATERIALS SCIENCE, 2004. **39**: p. 3211 – 3212.
135. Jiana, X., et al., *Effect of power ultrasound on solidification of aluminum A356 alloy*. Materials Letters, 2005. **59**(190– 193): p. 2005.
136. Li, X., Y. Yang, and D. Weiss, *Theoretical and experimental study on ultrasonic dispersion of nanoparticles for strengthening cast Aluminum Alloy A356*. Metallurgical Science and Technology 2008. **26**(2).

137. Moghadam, A.D., et al., *On the Reaction Pathway of the Formation of In-Situ Nanometric TiB₂ in Aluminum Matrix Composite*. ACS Industrial & Engineering Chemistry Research, 2016. **Accepted**.
138. Kubaschewski, O., C.B. Alcock, and R.I. Spencer, *Materials Thermo-chemistry*. 1993: Pergamon Press.
139. Ricci, P.C., et al., *Anatase-to-rutile phase transition in TiO₂ nanoparticles irradiated by visible light*. The Journal of Physical Chemistry C, 2013. **117**(15): p. 7850-7857.
140. Mazahery, A. and M.O. Shabani, *Plasticity and microstructure of A356 matrix nano composites*. Journal of King Saud University-Engineering Sciences, 2013. **25**(1): p. 41-48.
141. Suresh, S., *Fundamentals of metal-matrix composites*. 2013: Elsevier.
142. Ibrahim, I., F. Mohamed, and E. Lavernia, *Particulate reinforced metal matrix composites—a review*. Journal of materials science, 1991. **26**(5): p. 1137-1156.
143. Hashin, Z. and S. Shtrikman, *A variational approach to the theory of the elastic behaviour of multiphase materials*. Journal of the Mechanics and Physics of Solids, 1963. **11**(2): p. 127-140.
144. Dinsdale, A. and P. Quedstedt, *The viscosity of aluminium and its alloys--A review of data and models*. Journal of materials science, 2004. **39**(24): p. 7221-7228.
145. Moghadam, A.D., et al., *Effect of In-situ Processing Parameters on the Mechanical and Tribological Properties of Self-Lubricating Hybrid Aluminum Nanocomposites*. Tribology Letters, 2016. **62**(2): p. 1-10.
146. Zhou, X., et al., *Micro-mechanism in Self-lubrication of TiB₂/Al Composite*. ACS applied materials & interfaces, 2015.
147. Menezes, P.L., et al., *Friction and wear*, in *Tribology for Scientists and Engineers*. 2013, Springer. p. 43-91.
148. Erdemir, A., G. Fenske, and R. Erck, *A study of the formation and self-lubrication mechanisms of boric acid films on boric oxide coatings*. Surface and coatings technology, 1990. **43**: p. 588-596.
149. Ma, X., W. Unertl, and A. Erdemir, *The boron oxide–boric acid system: Nanoscale mechanical and wear properties*. Journal of materials research, 1999. **14**(08): p. 3455-3466.

Appendix I (Corrosion and Wetting of Al/ (TiB₂-Al₂O₃) Micro- and Nanocomposites)

The metallic materials used in water treatment, water storage and water transportation often get wetted by water and oils, resulting in corrosion and surface fouling, and limited service life. In an attempt to mitigate this problem, surface properties of metallic substrates have been modified through coating techniques that include sol-gel methods, silanation, and nano- and micro-patterning via lithography. Some of these approaches lead to patterns or coatings that are expensive, are not durable, or are not viable for large-scale shaped components. Several recent studies indicate that increasing the contact angle leads to reduced corrosion. Wetting behavior is influenced by the surface tensions and interfacial tension between the liquid and the solid metal, surface roughness, heterogeneity, particle shape and size, and also by various physical and chemical processes occurring at the solid-liquid interface. A limited amount of work has been done to probe the correlation between the surface chemistry, surface roughness, and surface wettability. Until now, very little attention has been paid to the effect of grain size, grain orientation, texture, microstructural phases, state of strain, and oxidation of metals and their alloys on their surface wettability.

The size and dispersion of the grains and the second phase in a metallic composite with different chemical properties and therefore different interfacial energies directly impact the amount of the London dispersion force. The grain boundaries and interfaces between phases present in the microstructure have a different surface energy that is not well known and that affects wettability. Our aim is to investigate the effect of surface microstructure, including grain size and second phase size on water/air contact angle. In principle, the objective is to enhance the scientific understanding

of the effect of second-order parameters on intermolecular and surface forces, surface tensions, interfacial energies, and wetting properties of a surface to influence corrosion, fouling, wear, and energy loss due to friction during flow.

Under the sponsorship of the I/UCRC NSF, the contact angle and water wettability of the synthesized aluminum alloys and composites using micron and nanosized TiB_2 and Al_2O_3 been studied. Additionally, the variation in contact angle as a factor of grain microstructure have been investigated. To decouple the effect of reinforcement and matrix grain size we investigated experimentally wetting of composite materials with initially smooth surface and with the matrix roughness by etching, as described in the next section.

The samples were ground and polished to create a smooth surface. The grinding involved successive steps with 400, 600 and 1200 grit SiC paper. Polishing was done with a soft cloth impregnated with 1 micron alumina.

The contact angles for all samples were measured at least five times per sample using the model 250 Ramé-Hart Goniometer (Figure 67). To keep the environment constant the experiments were performed using approximately 5 ml of cold tap water (Figure 68). Surfaces were air dried between measurements.

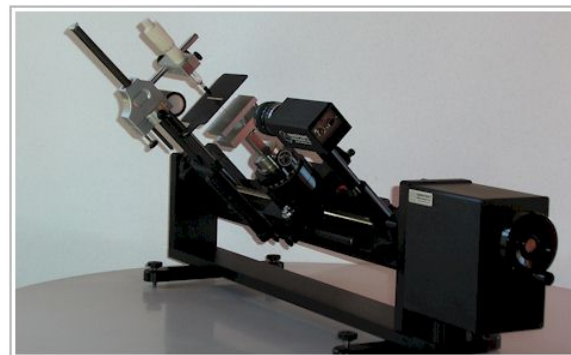
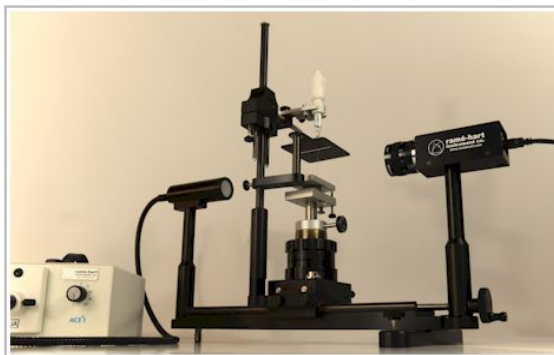


Figure 67 Rame Hart Model 500 Goniometer (Measures Contact Angle of Water in Air & Oil in Water)

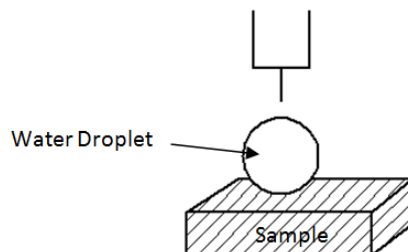


Figure 68 Schematic of water/air contact angle measurement.

In the following report, all the polarization plots were generated by applying a potential of 250 mV (-250 mV to +250 mV) in both positive and negative directions from the open circuit potential. The electrolyte used was a 3.5% NaCl solution using a standard calomel electrode as the reference electrode and platinum electrode as the counter electrode. The data obtained from Tafel diagrams (E_{corr} , i_{corr}) were used to estimate the corrosion resistance of the metals.

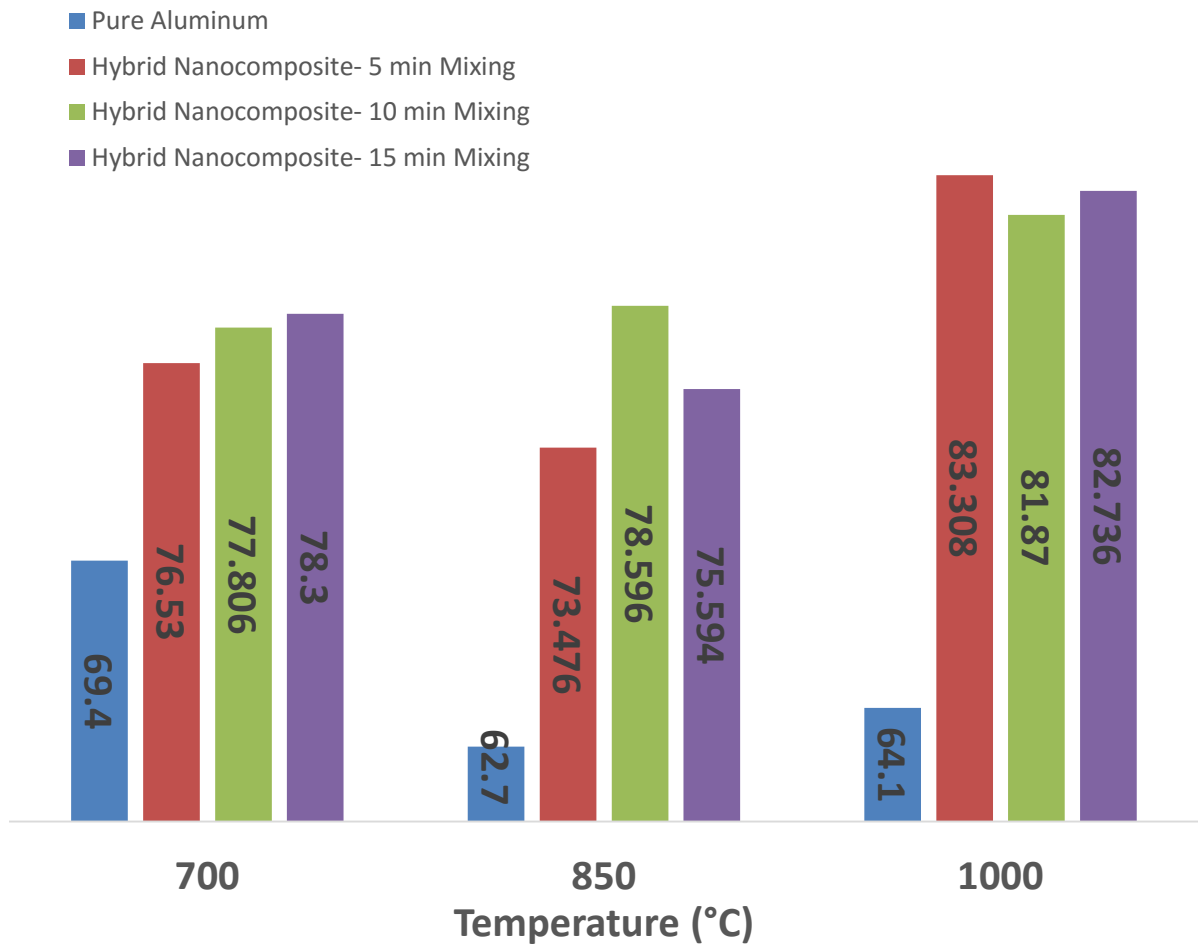


Figure 69 Comparison of contact angles between aluminum and its composites at different pouring temperature

The wetting of pure aluminum, composites reinforced by TiB_2 and Al_2O_3 at different weight percentage of reinforcement particles were investigated. Figure 69 illustrates the variation in contact angles by addition of nanosize TiO_2 and boron to the melt. As it can be seen, there is a significant increase in contact angle when nanoparticles are present.

Figure 70 shows the variation in the contact angle with grain size. The microstructures of these composites have been discussed and shown in chapter 4. As it can be observed, by increasing the grain size the water contact angle is decreasing. The data points marked by a blue circle are for unreinforced alloy. The variation in

contact angle by grain size can be explained by the grain boundaries energy. In a polycrystalline materials, the energy of the grain boundaries are higher than the grains. As a result, higher contact angles will be achieved at higher grain boundary densities.

Figure 71 shows the Potentiodynamic polarization plot of unreinforced pure aluminum and Aluminum/ (TiB₂-Al₂O₃) nanocomposite and the results are summarized in Table 9. Results show that the addition of nanoparticles has no adverse effect on corrosion resistance of aluminum.

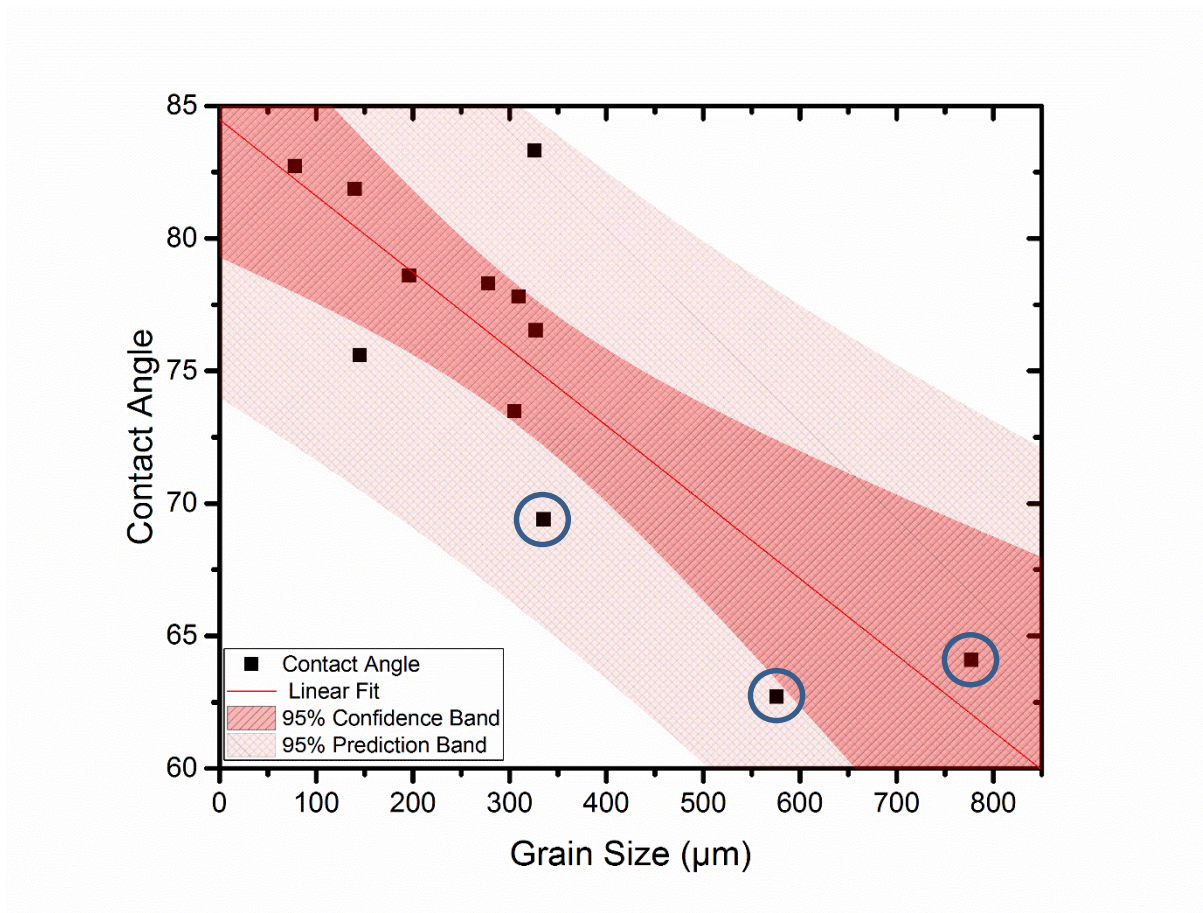


Figure 70 Variation in contact angle by the matrix grain size

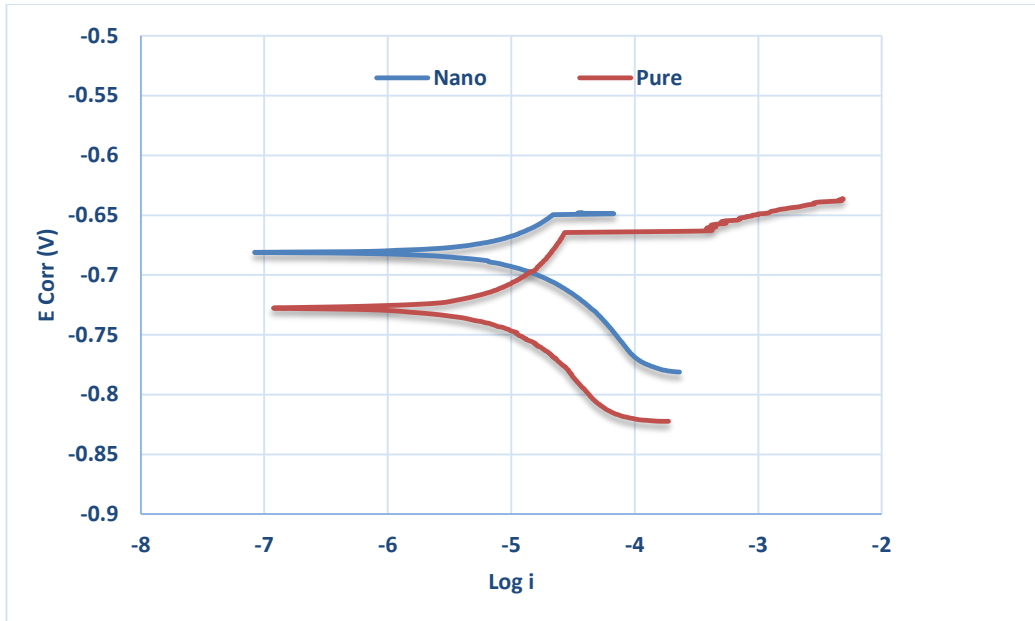

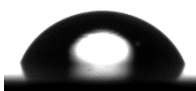
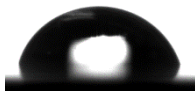
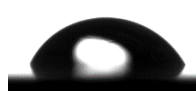
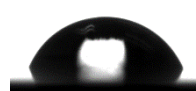


Figure 71 Potentiodynamic polarization plot of unreinforced pure aluminum and Aluminum/ (TiB₂-Al₂O₃) nanocomposite






Table 9 Corrosion current and corrosion potential of unreinforced pure aluminum and Aluminum/ (TiB₂-Al₂O₃) nanocomposite

| Materials | E _{Corr} (mV) | I _{Corr} (μA) |
|-----------|------------------------|------------------------|
| Pure | -726.962 | 0.003 |
| Nano | -680.392 | 0.003 |

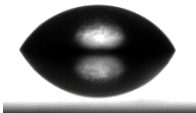
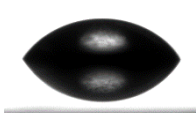
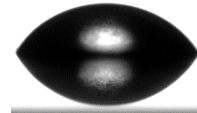
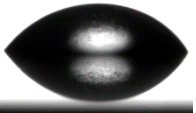
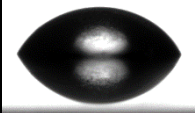
Hybrid nanocomposite; Pouring Temperature: 700 °C; Mixing Time: 10 min
 Droplet size: 4 μ l average value: 77.806

| Test 1 | Test 2 | Test 3 | Test 4 | Test 5 |
|-----------------------------------------------------------------------------------|-----------------------------------------------------------------------------------|-----------------------------------------------------------------------------------|------------------------------------------------------------------------------------|-------------------------------------------------------------------------------------|
|  |  |  |  |  |
| 77.61 | 78.10 | 79.90 | 75.98 | 77.44 |

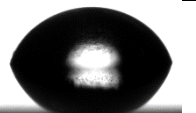
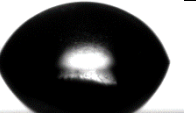
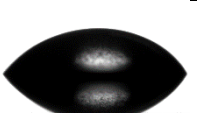
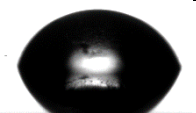
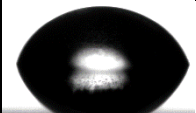
Hybrid nanocomposite; Pouring Temperature: 700 °C; Mixing Time: 10 min
 Droplet size: 10 μ l average value: 83.59

| Test 1 | Test 2 | Test 3 | Test 4 | Test 5 |
|-----------------------------------------------------------------------------------|-----------------------------------------------------------------------------------|-----------------------------------------------------------------------------------|------------------------------------------------------------------------------------|-------------------------------------------------------------------------------------|
|  |  |  |  |  |
| 83.48 | 83.26 | 84.61 | 85.58 | 81.02 |

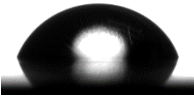
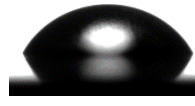
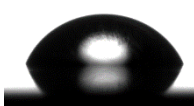
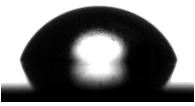
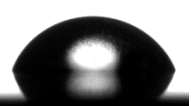
Hybrid nanocomposite; Pouring Temperature: 800 °C; Mixing Time: 5 min
 Droplet size: 4 μ l average value: 73.476

| Test 1 | Test 2 | Test 3 | Test 4 | Test 5 |
|-------------------------------------------------------------------------------------|-------------------------------------------------------------------------------------|-------------------------------------------------------------------------------------|--------------------------------------------------------------------------------------|---------------------------------------------------------------------------------------|
|  |  |  |  |  |
| 74.12 | 73.38 | 73.69 | 70.30 | 75.89 |

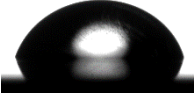
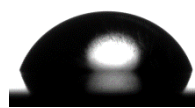
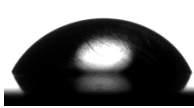
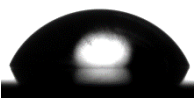
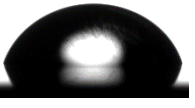
Hybrid nanocomposite; Pouring Temperature: 800 °C; Mixing Time: 5 min
 Droplet size: 10 μ l average value: 79.722

| Test 1 | Test 2 | Test 3 | Test 4 | Test 5 |
|-------------------------------------------------------------------------------------|-------------------------------------------------------------------------------------|-------------------------------------------------------------------------------------|--------------------------------------------------------------------------------------|---------------------------------------------------------------------------------------|
|  |  |  |  |  |
| 81.59 | 82.25 | 70.55 | 82.06 | 82.16 |

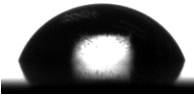
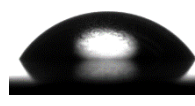
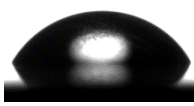
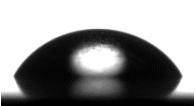
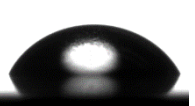
Hybrid nanocomposite; Pouring Temperature: 800 °C; Mixing Time: 10 min
 Droplet size: 4 μ l average value: 78.596

| Test 1 | Test 2 | Test 3 | Test 4 | Test 5 |
|-----------------------------------------------------------------------------------|-----------------------------------------------------------------------------------|-----------------------------------------------------------------------------------|------------------------------------------------------------------------------------|-------------------------------------------------------------------------------------|
|  |  |  |  |  |
| 80.36 | 74.98 | 77.97 | 80.36 | 79.31 |

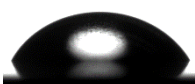
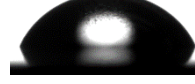
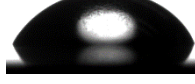
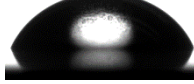
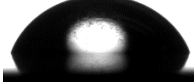
Hybrid nanocomposite; Pouring Temperature: 800 °C; Mixing Time: 10 min
 Droplet size: 10 μ l average value: 79.306

| Test 1 | Test 2 | Test 3 | Test 4 | Test 5 |
|-----------------------------------------------------------------------------------|-----------------------------------------------------------------------------------|-----------------------------------------------------------------------------------|------------------------------------------------------------------------------------|-------------------------------------------------------------------------------------|
|  |  |  |  |  |
| 80.50 | 80.44 | 76.76 | 77.96 | 80.87 |

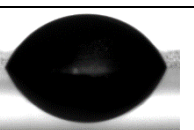
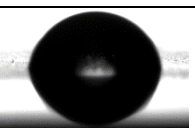
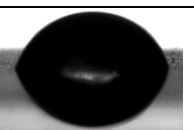
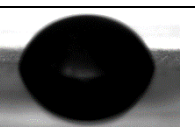
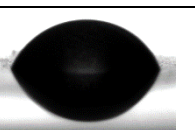
Hybrid nanocomposite; Pouring Temperature: 800 °C; Mixing Time: 15 min
 Droplet size: 4 μ l average value: 75.594

| Test 1 | Test 2 | Test 3 | Test 4 | Test 5 |
|-------------------------------------------------------------------------------------|-------------------------------------------------------------------------------------|-------------------------------------------------------------------------------------|--------------------------------------------------------------------------------------|---------------------------------------------------------------------------------------|
|  |  |  |  |  |
| 80.79 | 72.77 | 74.58 | 74.48 | 75.35 |

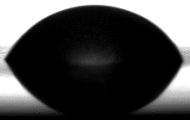
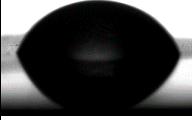
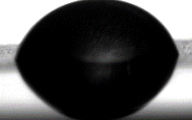
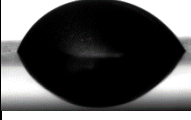
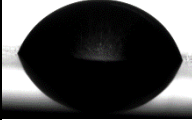
Hybrid nanocomposite; Pouring Temperature: 800 °C; Mixing Time: 15 min
 Droplet size: 10 μ l average value: 76.774

| Test 1 | Test 2 | Test 3 | Test 4 | Test 5 |
|-------------------------------------------------------------------------------------|-------------------------------------------------------------------------------------|-------------------------------------------------------------------------------------|--------------------------------------------------------------------------------------|---------------------------------------------------------------------------------------|
|  |  |  |  |  |
| 73.60 | 77.01 | 76.69 | 77.64 | 78.93 |


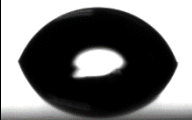

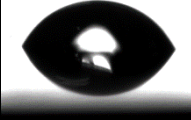
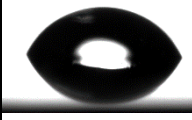
Hybrid nanocomposite; Pouring Temperature: 1000 °C; Mixing Time: 5 min
 Droplet size: 4 μ l average value: 83.308

| Test 1 | Test 2 | Test 3 | Test 4 | Test 5 |
|-------------------------------------------------------------------------------------|-------------------------------------------------------------------------------------|-------------------------------------------------------------------------------------|--------------------------------------------------------------------------------------|---------------------------------------------------------------------------------------|
|  |  |  |  |  |
| 78.43 | 88.94 | 83.78 | 86.15 | 79.24 |

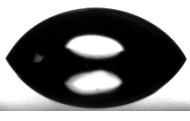
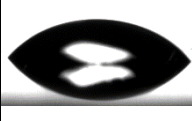



Hybrid nanocomposite; Pouring Temperature: 1000 °C; Mixing Time: 5 min
 Droplet size: 10 μ l average value: 80.236

| Test 1 | Test 2 | Test 3 | Test 4 | Test 5 |
|-----------------------------------------------------------------------------------|-----------------------------------------------------------------------------------|-----------------------------------------------------------------------------------|------------------------------------------------------------------------------------|-------------------------------------------------------------------------------------|
|  |  |  |  |  |
| 78.07 | 81.84 | 83.43 | 76.80 | 81.04 |

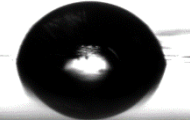
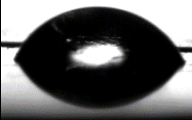
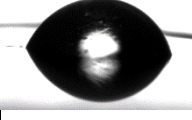
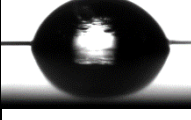
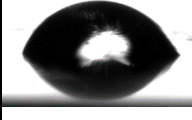
Hybrid nanocomposite; Pouring Temperature: 1000 °C; Mixing Time: 10 min
 Droplet size: 4 μ l average value: 81.87

| Test 1 | Test 2 | Test 3 | Test 4 | Test 5 |
|-----------------------------------------------------------------------------------|-----------------------------------------------------------------------------------|-----------------------------------------------------------------------------------|------------------------------------------------------------------------------------|-------------------------------------------------------------------------------------|
|  |  |  |  |  |
| 84.67 | 79.66 | 87.98 | 79.95 | 77.09 |

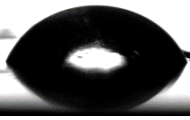
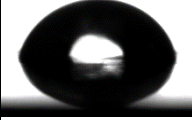
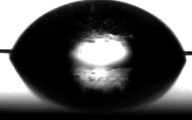
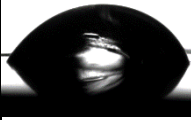
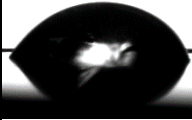
Hybrid nanocomposite; Pouring Temperature: 1000 °C; Mixing Time: 10 min
 Droplet size: 10 μ l average value: 76.636

| Test 1 | Test 2 | Test 3 | Test 4 | Test 5 |
|------------------------------------------------------------------------------------|------------------------------------------------------------------------------------|------------------------------------------------------------------------------------|-------------------------------------------------------------------------------------|--------------------------------------------------------------------------------------|
|  |  |  |  |  |
| 74.38 | 71.10 | 81.32 | 72.71 | 83.67 |

Hybrid nanocomposite; Pouring Temperature: 1000 °C; Mixing Time: 15 min
 Droplet size: 4 μ l average value: 82.736

| Test 1 | Test 2 | Test 3 | Test 4 | Test 5 |
|-------------------------------------------------------------------------------------|-------------------------------------------------------------------------------------|-------------------------------------------------------------------------------------|--------------------------------------------------------------------------------------|---------------------------------------------------------------------------------------|
|  |  |  |  |  |
| 88.74 | 78.69 | 83.40 | 84.12 | 78.73 |

Hybrid nanocomposite; Pouring Temperature: 1000 °C; Mixing Time: 15 min
 Droplet size: 10 μ l average value: 82.222

| Test 1 | Test 2 | Test 3 | Test 4 | Test 5 |
|-------------------------------------------------------------------------------------|-------------------------------------------------------------------------------------|-------------------------------------------------------------------------------------|--------------------------------------------------------------------------------------|---------------------------------------------------------------------------------------|
|  |  |  |  |  |
| 82.62 | 82.13 | 83.28 | 81.35 | 81.73 |

CURRICULUM VITAE

AFSANEH DORRI MOGHADAM

EDUCATION

B.S., Ferdowsi University of Mashhad – August 2007; Major: Metallurgical Engineering

M.S., Sharif University of Technology- Iran, January 2010; *Major: Materials Science and Engineering*

PUBLICATIONS- PEER REVIEWED PAPERS

1. Afsaneh Dorri Moghadam, J.B. Ferguson, Hugo Lopez, Pradeep Rohatgi, "On the Reaction Pathway of the Formation of In-Situ Nanometric TiB₂ in Aluminum Matrix Composite", ACS Industrial & Engineering Chemistry Research, Accepted, April 2016.
2. Afsaneh Dorri Moghadam, Emad Omrani, Pradeep L. Menezes, Pradeep K. Rohatgi, "Effect of In-situ Processing Parameters on the Mechanical and Tribological Properties of Self-Lubricating Hybrid Aluminum Nanocomposites", Tribology Letters 62, no. 2 (2016): 1-10.
3. Emad Omrani, Afsaneh Dorri Moghadam, Pradeep L. Menezes, Pradeep K. Rohatgi, "Effect of Graphite Particles on Improving Tribological Properties Al-16Si-5Graphite Composite under Fully Flooded and Starved Lubrication Conditions for Transportation Applications", Journal of Advance Manufacturing Technology (2016), 1-11.
4. Afsaneh Dorri Moghadam, Emad Omrani, Pradeep L. Menezes, Pradeep K. Rohatgi "Mechanical and tribological properties of self-lubricating metal matrix nanocomposites reinforced by carbon nanotubes (CNTs) and graphene – A review", Composite Part B: Engineering 77 (2015): 402-420.
5. Afsaneh Dorri Moghadam, Emad Omrani, Pradeep L. Menezes, Pradeep K. Rohatgi "Influence of graphite reinforcement on the tribological behavior of self-lubricating aluminum matrix composites – A Review", Journal of Advance Manufacturing Technology (2015): 1-22.
6. Afsaneh Dorri Moghadam, Simin Nickelsen, J.B. Ferguson, Pradeep Rohatgi, "Modeling and Experimental Study of Oil/Water Contact Angle on Biomimetic Micro- Parallel-Patterned Self-Cleaning Surfaces of Selected Alloys Used in Water Industry", Applied Surface Science, 353 (2015): 781-787.
7. Vahid Hejazi, Afsaneh Dorri Moghadam, Pradeep Rohatgi, Michael Nosonovsky. "Beyond Wenzel and Cassie–Baxter: Second-Order Effects on the Wetting of Rough Surfaces." Langmuir 30, no. 31 (2014): 9423-9429.
8. J.B. Ferguson, B F. Schultz, Afsaneh Dorri Moghadam, P K. Rohatgi, "Influence of Laser Velocity and Powder Flow Rate on Porosity in 420 Stainless Steel and 4140 Steel Using Laser Engineered Net Shaping", Journal of Manufacturing processes 19C (2015): 163-170.
9. Emad Omrani, Bamdad Barari, Afsaneh Dorri Moghadam, Pradeep Rohatgi, Krishna M Pillai, "Mechanical and Tribological Properties of Bio-based Epoxy Composites Reinforced by 2D Woven Carbon Fiber Made Using Resin Transfer Molding Process", Tribology international 92 (2015): 222–232.
10. Afsaneh Dorri Moghadam, J.B. Ferguson, Benjamin F. Schultz, Pradeep K. Rohatgi, "In-situ Reactions in Cast Aluminum Alloy/Silica Composites and Their Effect on Physical and Mechanical Properties", Journal of Manufacturing and Performance, Under review.
11. Mechanical, Physical and Tribological Characterization of Nano-Cellulose Fibers Reinforced Bio-Epoxy Composites: An Attempt to Fabricate and Scale the 'Green' Composite, Carbohydrate Polymers, under review.
12. Afsaneh Dorri Moghadam, Benjamin F. Schultz, J. B. Ferguson, Emad Omrani, Pradeep K. Rohatgi, and Nikhil Gupta, "Functional Metal Matrix Composites: Self-lubricating, Self-healing, and Nanocomposites-An Outlook" JOM 66.6 (2014): 872-881.
13. Pradeep K. Rohatgi, Afsaneh Dorri M., Benjamin F. Schultz, J.B. Ferguson "Synthesis and Properties of Metal Matrix Nanocomposites (MMNCs), Syntactic Foams, Self-Lubricating

- and Self-Healing Metals”, PRICM: 8 Pacific Rim International Congress on Advanced Materials and Processing (pp. 1515-1524). John Wiley & Sons, Inc.
14. Emad Omrani, Ali Shokuhfar, Afsaneh Dorri Moghadam, “The Effects of homogenization Time and Cooling Environment on Microstructure and Transformation Temperatures of Ni-42.5wt%Ti-7.5wt%Cu Alloy”, Defect and Diffusion Forum 297-301 (2010) : 344-353.

PUBLICATIONS- BOOKS AND CHAPTERS

1. Moghadam, A. D., Omrani, E., Menezes, P. L., & Rohatgi, P. K. (2015). New Emerging Self-lubricating Metal Matrix Composites for Tribological Applications. Ecotribology: Research Developments, 63 (Book Chapter).

INTERNATIONAL CONFERENCE PRESENTATIONS

1. Morphology development of Thermoplastic Starch/ Polypropylene immiscible polymer blends, Antec 2016.
2. Tribological Properties of Micro- and Nano-sized Solid Lubricant (Graphite and Graphene) as Lubricant Oil Additives, 2015 STLE Tribology Frontiers Conference, October 25 - 27, 2015, Denver, Colorado.
3. Effect of In-situ Processing Parameters on the Mechanical and Tribological Properties of Hybrid Aluminum Nanocomposites, 2015 STLE Tribology Frontiers Conference, October 2015, Denver, Colorado.
4. In-situ TiB₂ Reinforced Aluminum Matrix Nanocomposites, TMS Annual Meeting and Exhibition, Nanocomposites Symposium, March 2015, Orlando, Florida.
5. Synthesis and Properties of Metal Matrix Nanocomposites (MMNCS), Syntactic Foams, Self-Lubricating and Self-Healing Metals. In PRICM: 8 Pacific Rim International Congress on Advanced Materials and Processing, 2013.
6. Modification of starch based packaging in Iran plastic industry”, First conference on advanced packaging industry, 15-17 November 2010, Tehran, Iran.
7. The Effects of Annealing Time and Cooling Environment on Microstructure and Transformation Temperatures of Ni-42.5wt%Ti-7.5wt%Cu Alloy”, Proceeding of 5th international conference of DSL, 2009, Rome, Italy.

AWARDS AND HONORS

1. UW- Milwaukee Distinguished Dissertation Fellowship, (Total \$ 16,500), University of Wisconsin Milwaukee, Fall 2014.
2. American Foundry Society Award- Northeastern Wisconsin Chapter Scholarship, Student section, 2012.
3. Foundry Education Foundation scholarship
4. Runner Up in the 3rd annual B.C. Church Microscopy Contest, University of Wisconsin Milwaukee, May 2013.

TEACHING EXPERIENCES

1. Engineering Materials (U-MATENG201); Instructor; Department of Materials Engineering, University of Wisconsin- Milwaukee, Spring 2016.
2. Engineering Composites (U/G- MECHENG457); Instructor; Department of Mechanical Engineering, University of Wisconsin- Milwaukee, Fall 2015.
3. Engineering Materials (U- MATENG201), Teaching Assistant; Department of Materials Science and Engineering, University of Wisconsin- Milwaukee, Fall 2011- Spring 2013
4. Materials and Processes in Manufacturing (U- MATENG330), Teaching Assistant; Department of Materials Science and Engineering, University of Wisconsin- Milwaukee, Fall 2011- Spring 2013
5. Advanced Materials Characterization (U/G- MATENG570), Lab Instructor; Department of Materials Science and Engineering, University of Wisconsin- Milwaukee, Fall 2014

AFFILIATIONS AND MEMBERSHIPS

1. American foundry society (AFS)
2. foundry educational foundation (FEF)
3. Society of plastic engineers (SPE)
4. Water Equipment and and Policy Research Center (WEP IUCRC)
5. Society of Tribologists and Lubrication Engineers (STLE)
6. UWM Women in Science & Engineering